Characterization of Novel Thin-Films and Structures for Integrated Circuit and Photovoltaic Applications

by

Zhao Zhao

A Dissertation Presented in Partial Fulfillment
of the Requirements for the Degree
Doctor of Philosophy

Approved February 2017 by the
Graduate Supervisory Committee:

Terry Alford, Chair
Shahriar Anwar
David Theodore

ARIZONA STATE UNIVERSITY

May 2017

ABSTRACT

Thin films have been widely used in various applications. This research focuses on the characterization of novel thin films in the integrated circuits and photovoltaic techniques. The ion implanted layer in silicon can be treated as ion implanted thin film, which plays an essential role in the integrated circuits fabrication. Novel rapid annealing methods, *i.e.* microwave annealing and laser annealing, are conducted to activate ion dopants and repair the damages, and then are compared with the conventional rapid thermal annealing (RTA). In terms of As^+ and P^+ implanted Si, the electrical and structural characterization confirms that the microwave and laser annealing can achieve more efficient dopant activation and recrystallization than conventional RTA. The efficient dopant activation in microwave annealing is attributed to ion hopping under microwave field, while the liquid phase growth in laser annealing provides its efficient dopant activation. The characterization of dopants diffusion shows no visible diffusion after microwave annealing, some extent of end range of diffusion after RTA, and significant dopant diffusion after laser annealing.

For photovoltaic applications, an indium-free novel three-layer thin-film structure (transparent composited electrode (TCE)) is demonstrated as a promising transparent conductive electrode for solar cells. The characterization of TCE mainly focuses on its optical and electrical properties. Transfer matrix method for optical transmittance calculation is validated and proved to be a desirable method for predicting transmittance of TCE containing continuous metal layer, and can estimate the trend of transmittance as the layer thickness changes. TiO_2/Ag/TiO_2 (TAgT) electrode for organic solar cells (OSCs) is then designed using numerical simulation and shows much higher Haacke

figure of merit than indium tin oxide (ITO). In addition, TAgT based OSC shows better performance than ITO based OSC when compatible hole transfer layer is employed. The electrical and structural characterization of hole transfer layers (HTLs) in OSCs reveals MoO_3 is the compatible HTL for TAgT anode. In the end, the reactive ink printed Ag film for solar cell contact application is studied by characterizing its electromigration lifetime. A percolative model is proposed and validated for predicting the resistivity and lifetime of printed Ag thin films containing porous structure.

ACKNOWLEDGMENTS

I would like to gratefully thank my advisor Dr. Terry Alford for supporting me and giving me instructions and inspiration. I gain not only knowledge but also motivation from him. He is always being down to the earth, and takes care of me like his family member. I am grateful for the help from Dr. Lea Lanz. She patiently helped me to overcome English barrier and to pass the English test, which means a lot to me.

I would also thank Dr. Rajitha Vemuri for her support and generous help on experiments and measurements in the first year. She led me to get into this group and help me to initialize my first project. I really appreciate the help from Dr. Sayantan Das, Dr. Aritra Dhar. Barry O'Brien. Dr. Sayantan Das gave a great help on starting my organic solar cell project and also gave lots of inspirations. Dr. Aritra Dhar.offered great guidance on starting my thin film deposition project. I would greatly thank for Barry O'Brien's generous help on deposition tool maintenance. He offered a very valuable instructions, guidance and help on using, fixing and maintaining the tool. Without his help, I cannot proceed on my organic solar cell project and cannot gain so much experience on tool maintaining. I would like to thank visiting scholar and students in Dr. Alford group: Dr. Yuanqing Chen, Taliya Gunawansa, Aditya Yerramilli.

I would also express my gratitude to my committee, Dr. David Theodore. He offered great help on electron microscopy measurement and his kindness to provide suggestion to data analysis.and manuscript edition. I would like to thank my committee Dr. Shahriar Anwar for his generous help and previous committee member Dr. Candace Chan for her time and suggestions on comprehensive exam.

I would like to thank Dr. Benjamin French in Intel for SIMS measurement and analysis. His extremely helpful suggestions on SIMS analysis help me to get the reasonable data. I would like to thank Barry Wilkens, Jason Ng, Wei Lu and Dr. S.S. Lau for their help in material characterization, sample preparation and data measurement;

Finally, I would owe my work to my parents and my friends, and thank for their support and love. Without them, I would not be able to come to U.S. and accomplish my Ph.D degree.

TABLE OF CONTENTS

Page

CHAPTER Page

CHAPTER Page

LIST OF TABLES

Table Page

Table Page

LIST OF FIGURES

Figure Page

Figure Page

Figure Page

Figure Page

1. INTRODUCTION

1.1. Ion Implanted Thin-Film

1.1.1. Ion Implantation

In semiconductor industry, introducing dopants into the intrinsic semiconductor is the most common way to obtain a thin-film layer in low resistivity for semiconductor applications[1]. Methods of introducing dopant atoms include: diffusion and ion implantation. The most commonly used method is ion implantation in which the dopant atoms are ionized and accelerated to 10 - 150 keV energy or higher and bombarded into the wafer. During this process, a large amount of vacancies and disordered array of atoms (*i.e.*, damages) are created in the wafer surface, leading to amorphizationof the implanted layer[2].

The advantage of ion implantation is that the specific dose or amount of ions (dopant atoms) are precisely introduced into silicon. The amount of ions (dose) can be easily controlled by increase the implantation time or current, which allows the subtle tailoring of dose in metal-oxide-semiconductor (MOS) devices. Moreover, the depth of ion can also be easily controlled by the implantation energy[3]. The ideal distribution of implanted ion is a Gaussian distribution[3]. The depth of the peak concentration is call projected range (R_p), which depends on the energy, mass of incident ions and the atomic number of matrix material[4]. Heave ions typically has shorter R_p, but light ions has longer R_p. The straggle (ΔR_p) is defined to represent the standard deviation of ion distribution[4]. In reality, ion profile is not a perfect Gaussian distribution. For light ions will high energy, the distribution is possible shifted towards the surface due to backscattering and

this is called negative skewness. For heavy ions at low energy, positive skewness might happen, in which the profile might be shifted toward the end due to ion channeling[3].

1.1.1.1 Nuclear stopping and electronic stopping

When dopants are implanted into the Si wafers, they travel through the material, collide with atoms and finally come to rest due to the loss of energy[1]. The loss of energy has two mechanisms: nuclear stopping and electronic stopping[5]. Depending on the implantation energy, the nuclear stopping or electronic stopping dominates and the extent of the damage varies. The higher implantation energy does not necessarily mean more damage. In nuclear energy loss, ions with low incident energy are able to interact with atomic cores of materials and lose energy in their elastic collision[5]. Ions transfer energy to atoms, resulting in eventual displacement of these atoms[5]. Hence, damage is created in this process. In electronic energy loss event, the energetic particles with high velocity lose energy primarily through inelastic collisions with electron cloud, transferring energy to electrons, resulting in little damage[5]. Based on the energy loss mechanism, if two kinds of dopants species implanted with the same energy, they may experience different energy loss because their different masses lead to different energy loss mechanism. Therefore, different dopants with same implantation energy can cause different levels of damage. It is reported that for boron, electronic energy loss dominates in the range of 10 to 1000 keV, while for arsenic and phosphorus, the electronic energy loss dominates after energies of 130 and 700 keV, respectively[5, 6]. In our study, boron and phosphorus ions are implanted with energy of 15 keV. According to the energy range of the two energy-loss mechanisms in Si for different implants[6], boron implants mainly experience electronic loss; while, nuclear energy loss dominates in phosphorus implanted samples, suggesting

that phosphorus dopants cause more damage than boron dopants do. The damage can be characterized by ion channeling in Rutherford backscattering Spectrometry (RBS).

1.1.1.2 Defects and Amorphization in Ion Implanted Silicon

The ion implantation not only creates vacancies and disordered array of atoms, but also introduces excess ions into the silicon. A damage model called "+1" is introduced to describe the defects due to excess ions. This model assumes that the net effect of an implant is to introduce one extra interstitials when the ion is implanted into silicon[3]. This model has been widely accepted and used to explain many effects during damage removal and dopants diffusion[3].

Ion implantation is not necessary to create amorphous layer because the amorphization threshold has to be met. The implant dose for amorphous layer first appears is called threshold dose. It depends on both ion mass and implant temperature[7]. The light ions require a higher threshold dose than heavy ions do; at the same time the room temperature implantation needs a higher dose than the liquid temperature implantation does to create amorphous layer[7]. For example, the threshold dose for amorphization at 30 ℃ is 8×10^{16} and 6×10^{14} cm^{-2} for boron and phosphorous dopants, respectively, while the threshold dose at –170 ℃ is 1×10^{15} and 2×10^{14} cm^{-2} for B and P dopants, respectively[7].

1.1.2. Post-Implantation Annealing

The damage are typically removed by post implantation annealing. During the annealing, the silicon lattice is restored and the dopants are moved to substitutional position.

1.1.2.1 Damage Removal and Evolution During Annealing

1.1.2.1.1 Solid Phase Epitaxial Regrowth

In the amorphous region of the ion implanted sample, the amorphous layer experiences a solid phase epitaxial (SPE) regrowth, in which the layer-by-layer epitaxial re-arrangement starts from the amorphous/crystalline (a/c) interface[3]. Most of the primary damage in the amorphous region are removed and most of the dopant atoms in the amorphous region are incorporated into the substitutional sites during SPE[3]. In addition, due to the low temperature requirement of SPE, no dopant diffusion occurs[3]. In fact, SPE simultaneously enables all the damage removal and high extent of dopant activation without noticeable dopant diffusion[3].

1.1.2.1.2 Removal of primary defects and secondary defects

In the damage region not having completely amorphization, most of the Frenkel defect pairs can undergo bulk recombination at low temperature of 400 ℃ in the initial stage of annealing[3]. During this process, nearly all the vacancy and interstitials are removed and only the interstitials defects due to extra implanted ions remains[3]. Considering atom lost due to implant sputtering near the surface and vacancies captured in the native oxide layer, the amount of interstitials is not the same but approximately approaches the implant dose according to the "+1" damage model as we mentioned in previous section[3], It should be noted that the remaining interstitials are either dopant ions or Si self-interstitials.

Then the Si interstitials are quickly condense into rod-shaped defect clusters and lies on ^{8} plane of silicon when annealing temperature increase above 400 ℃[3]. These ^{8} defects starts to dissolve by the evaporation of Si interstitials when it is further annealed

at above 900 ℃ [3]. If the total damage is below a critical value, all the [8] defects will be dissolved. However, if the damage amount is above the critical value, some of the [9] defects grow while others dissolve and shrink[3]. As [8] defects grow to larger size, they turns into stable dislocation loops[3]. The dislocation loops will ripen to larger loops if the sample is further annealed at 1000 ℃[3]. These dislocation loops are called secondary defects and require higher temperature to remove. It was reported that 1100 ℃ for 60 sec can completely remove the secondary defects[3]. These dislocation loops are mainly located at the original a/c interface and are also called End-Of-Range (EOR) defects[3]. In the narrow region just beyond the a/c interface on the crystalline side, the damage level is just blow the amorphization threshold[3]. As a result, large amount of high level damages are generated but without amorphization, and the damage level is high enough to cause the formation of {311} defect and dislocation loops[3].

1.1.2.2 Dopant Activation

Resistivity of the wafer is still high after implantation due to the absence of long range order of the substrate lattice and the presence of dopants in off-lattice sites. Dopant activation is achieved by relocation of dopant atoms from interstitial sites, or off-lattice sites, into substitutional sites, where they can act as donors or acceptors and contribute electrons or holes. At the same time, the mobility will be improved by repairing the damages. Annealing implanted Si samples is performed to promote dopant activation and to obtain conductive materials. As discussed in last section, SPE that happens in amorphous layer enables high extent of dopant activation at low temperature. A sufficient dopant activation can be achieved at 600 ℃. However, for damage level just below amorphization, the annealing will generate stable secondary defects which hinders the

dopant activation, and the useful level of activation can only be achieved by annealing at higher temperature between 950-1050 ℃.

1.1.3 Annealing Techniques

Annealing methods to achieve damage removal and dopant activation are divided into solid phase epitaxial (SPE) regrowth and liquid phase epitaxial (LPE) regrowth based on their regrowth mechanism. Laser annealing is based on LPE regrowth, while metal induced crystallization (MIC), rapid thermal anneal (RTA)[10] and microwave anneal are based on SPE regrowth. In MIC, the metal layer, such as Ag and Au, is deposited on amorphous silicon[11, 12]. The metal atoms begin to intermix with the amorphous Si layer. Then the nuclearization of c-Si occurs at the interface[11, 12] and the Si crystallite is surround by metal-Si compounds. The Si atoms from the amorphous layer diffuse through the metal-Si compounds, precipitate on the crystalline phase nuclei , and cause the radial growth of crystalline Si[11, 12]. Finally, the metal is segregated to the top and bottom surface of the silicon[11, 12]. Compared to the direct reordering of the amorphous lattice which require a high temperature, MIC provides a reduced free energy for the system, so that the crystallization could be done in relative low temperature at ~250 ℃[12] . However, the contamination of ultra-thin metal film will lead to the failure of the devices[10]. The RTA achieves the rapid heating rate using quartz halogen lamps or tungsten halogen lamps, which provides radiation energy to recrystallize the amorphous layer in a short time. However, even RTA minimizes the diffusion length by short annealing at high temperature; it still causes the end of range diffusion[13].

1.1.3.1 Microwave Annealing

1.1.3.1.1 Microwave heating mechanism

The interaction of microwave and materials includes absorption, transmission and reflection. However, only the absorption procedure which is caused by the energy loss in the interaction leads to the heating of materials[14]. The energy loss includes the ion conduction loss and dipole polarization loss[15].

In ion conduction loss, the free electrons move back and forth, or ions move within the lattice network under the changing electromagnetic field[13]. The moving electrons or ions collide with other species and dissipate energy, leading to generation of heat in materials[15].

The dipole polarization loss is based on polarization mechanisms. The process of dipole formation (or alignment of already existing dipoles) under an external electric field E, is called polarization[15]. In term of electronic polarization, under the influence of an external electric field, the negatively charged electron cloud of an atom becomes displaced with respect to its positively charged core[15]. In ionic material, such as the alkali halides, cations and anions are displaced from their equilibrium positions under an external field. Moreover, many materials already possess permanent dipoles that can be aligned in an external electric field. This is called molecular polarization[16]. In dielectric materials, electric dipoles are created and align themselves with electromagnetic field. They rotate as the field alternates. As the field frequency increases, the rotation of dipole lags behind the field. Hence, dipoles collide with either surrounding electron clouds or other dipoles, resulting energy loss and heat generating.

The absolute value of absorption and the proportion of the ion conduction loss and dipole polarization loss are dependent on MW frequency and material parameters[16]. The ionic conduction loss dominates at low frequencies, because the time letting electrons transport in one direction reduces as the frequency increases, resulting in few collision events and less heat generation at high frequency[15]. On the other hand, dipole polarization loss is dominant at high frequencies. The lag between the rotation of dipole and changing of electromagnetic field becomes severe at high frequency so that most of the energy loss results from the friction of dipoles[15].

1.1.3.1.2 Dielectric Properties of Materials

The ionic loss and dipole loss mentioned above can be determined by the loss factor (ε''). For dielectric materials which is not conductive, the loss factor (ε'') is relating the out phase component of electric displacement (*D*) to the applied electric field[17, 18], which describes the how badly the dipoles lag behind the applied electric field. The electric displacement (*D*) is the electric field strength within the dielectric material. For conductive materials, the loss factor is related to the density of free carries in the materials. When the materials is both conductive and has dipoles, both process contributes to the loss, the loss factor is called effective loss factor[14]. The dielectric constant (ε') which is also called relative permittivity, is related to the in-phase component of the electric displacement (*D*) to the applied electric field[17, 18]. This means ε' describe how much a material allows itself to be polarized.

The materials with large loss factor can experience higher extent of dipole dielectric loss and generate more heat. When the dipoles are able to follow the changing

of the applied field, the dielectric constant maintains its maximum value. As the frequency increases, the dipolar polarization falls behind the field. When the frequency reaches a point where the dipole is no longer rotates significantly with respect to changing field, the effective polarization decreases[19]. The reduced effective polarization means a decrease in the dielectric constant and an increase of the loss factor as the frequency increases[19].

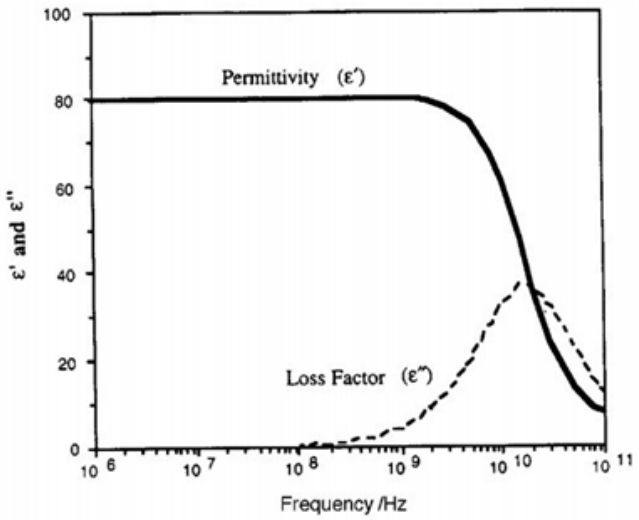

Figure 1.1 The variation of ε' and ε" with frequency for water at 20 ℃ [19]

1.1.3.1.3 Susceptor Assistance in Microwave Annealing

Temperature has a significant impact on loss factor and microwave absorption[14, 20]. As temperature increase, the dielectric relaxation time decrease, which means the dipoles are easier to response to the oscillating field due to the increased kinetic energy. This means the loss factor peak will shift to higher frequency as temperature increase. As a result, the loss factor and microwave absorption efficiency of a material at a certain frequency can be increased by tailoring the temperature.

Amorphous Si cannot efficiently absorb microwave at low temperature[21, 22]. When the ion implanted Si is annealed at the microwave cavity, it cannot obtain a high temperature without any external heat supply[22]. To achieve a temperature that is high enough to repair the damages and activate the dopants, additional heat provided by the susceptor is required. Typically, samples are placed in contacted or nearby the susceptor. This method is called hybrid heating, in which the sample is simultaneously subjected to the microwave heating and the conductive heating from susceptor[14]. The susceptor is typically a lossy material that can easily be heated up by absorbing microwave radiations. In our case, susceptor that is made up of Al_2O_3 infused SiC is employed. The large dielectric loss factor of SiC ensures that only its surface can be heated to very high temperatures, which in turn allows the sample on the susceptor to be heated up. More importantly, due to the large heat capacity (1.09 J/mol K) and high thermal conductivity (350 W/m K) of SiC, temperature gradients across the suscepotor surface do not exist, which allows an excellent uniform heating.

1.1.3.1.4 Volumetric Heating and Penetration Depth

Microwave heating is dominated by volumetric heating mechanism. In volumetric heating, the heat energy is transferred electromagnetically through the surface, rather than as a heat flux[18]. The rate of heating is no longer limited by thermally diffusivity and surface temperature[18]. However, the electric field decreases as it penetrates materials, which means volumetric heating is only valid for layers close to surface. The penetration depth is defined as the distance from the sample surface where the absorbed power is 1/e of the absorbed power at the surface[15].

$$D_p = \frac{\lambda}{4\pi k} = \frac{cn}{2\pi f \varepsilon''} \tag{1.1}$$

where λ is wavelength, n is real part of the refractive index, k is the imaginary part of refractive index (also called extinction coefficient or damping constant), c is speed of light, and f is frequency in Hz, ε" is a dielectric loss factor. According equation (1.2), materials with very high extinction coefficient have very small penetration depths, approaching to zero. Materials with such dielectric property are treated as reflectors, like Al. Similarly, materials with a very low extinction coefficient have a large penetration depth and are transparent to the microwave field, like Al_2O_3.

The power absorbed by the dielectric per volume can be calculated using the following equation[19]:

$$P = \omega \varepsilon_0 \varepsilon_{eff}'' E_{rms}^2 = \rho C_p \Delta T \tag{1.2}$$

where, ω is the angular microwave frequency, ε_0 is permittivity of free space, ε_{eff}'' is the relative effective dielectric factor. E_{rms} is the average electric field in dielectrics[19], ρ is the mass density of materials, C_p is the heat capacity, and ΔT is the temperature gradient.

1.1.3.2 Laser Annealing

Lasers are widely used for many applications, including growing crystal, depositing films, forming metallic glasses, cutting[23]. In terms of the output characteristics of lasers, lasers are divided into continuous wavelength (cw) and pulsed wavelength[23]. The pulsed laser typically offers high energy deposition pulse over a relatively short time while the cw laser produces continuous light and energy deposition. Various laser sources

are available such as gas lasers (i.e. Argon, Carbon dioxide), solid lasers (Ruby, YAG or glass), and liquid lasers (Dye).

Laser can be used to anneal ion implanted Si. While the liquid phase epitaxial regrowth is responsible for the transition from amorphous to signal crystalline silicon[24], the surface layer melts and solidifies in extremely short tim[25-28], as low as 2 ms. The laser energy is absorbed in the near surface region, causing the melting of the surface layer[29] and is able to remove nearly all the defects in surface layer[24]. The large diffusion coefficient in the liquid phase leads to the extensive dopant diffusion, therefore it hinders the achievement of a shallow junction for metal-oxide. However, the melt layer thickness can be controlled by the incident laser beam. These effects are demanded by semiconductor industry, particularly in the annealing of ion implanted Si.[23]

1.1.3.2.1 Laser Heating Mechanism

The wavelength of the typical commercial high power laser varies from UV region up to 10.6 μm[23], corresponding to a frequency of 3×10^8 to 2.8×10^4 GHz, whose frequency is much higher than 2.45 GHz microwave. Under such a high frequency, the dipoles that created by nuclei are too heavy to repose to the high-frequency oscillating field[23]. As a result, laser being an electromagnetic wave mainly interacts with the valence electrons. The bonded valence electrons only weakly respond to the light wave, and mainly affects its phase velocity[23]. Free valence electrons are accelerated and oscillate under the periodically changed electromagnetic field[23], i.e. extract energy from the field. The oscillating electrons either reradiate their kinetic energy or transfer their energy by colliding with the lattice atoms[23]. The reradiation corresponds to the light reflection[23].

When the photon energy is larger than the band gap of semiconductor, the light is absorbed by the interband transition of electrons, and the excited carriers are generated[23]. However, at high light intensity, the generation rate of excited electrons will dramatically increase[23]. The generated hot electrons will undergo the relaxation by either carrier-lattice collisions or recombination[23]. When the collision rate is higher than the recombination rate, the lattice heating occurs[23]. At a sufficient high intensity, the hot electron generation rate will be even higher than relaxation rate by carrier-lattice collision, then the large number of free hot electrons build up, collide with each other and establish a thermal equilibrium in 10^{-14} sec[23]. Therefore, this heating effect induced by carrier collision occurs even before the lattice heating[23]. The diffusion of these hot carriers determines the heated volume[23]. When the laser is off, these electrons will recombine within 10^{-9} sec[23].

In addition, As the incident laser raises the temperature of the semiconductor material more phonons are generated and these phonons contribute to the heating mechanism[23]. More photon will be absorbed by phonons and the phonons will interact with the carriers, and transfer the energy to the lattice[23]. As a result, the carrier-lattice collision frequency will increase, leading to the enhanced heating effect[23]. The increase in lattice temperature will in turn increase the collision frequency[23]. This is a positive feedback process.

1.1.3.2.2 Energy Deposition in Laser Annealing

Laser annealing is based on the interaction between light wave and valence electrons in material, so it greatly depends on the optical properties of the material. It is convenient to describe the energy deposition of laser using reflectivity (R) and absorption

coefficient α or the absorption length α^{-1}. The absorption length is also called penetration depth, which means the depth where the intensity of the light decreases to 1/*e* of its original value when the light propagates through the material. The energy absorbed per unit volume (in Joules per cubic centimeter) as a function of sample depth (z) during laser annealing can be calculated by [23]:

$$\Phi(z) = I_0[(1-R)/d]e^{-z/d} \tag{1.3}$$

where the I_0 is the output /incident energy density of the laser (in Joules per square centimeter), *R* is the reflectance of materials at the laser wavelength and *d* is the absorption depth, which is the reciprocal of the absorption coefficient α

Amorphous Si has large absorption coefficient than crystalline Si, which also means smaller absorption length in amorphous Si. Smaller absorption length means most of the energy is absorbed within a very thin layer, resulting in high volume energy density within the thin layer, and think layer is more likely to be melt. For materials with large α^{-1}, the volume energy density being absorbed is smaller, as a result, it requires higher energy input to melt the layer with the same thickness. In ion implanted materials, the thickness of the amorphous layer can be either smaller or larger than absorption length α^{-1}. If the amorphous layer is smaller than α^{-1}, only a portion of the laser energy is used to melt the amorphous layer, and rest of the laser energy is distributed in crystalline silicon in a larger depth due to the larger α^{-1} value of crystalline Si.

1.1.3.2.3 The Characteristics of Laser Annealing

The characteristics of laser annealing is fast heating and cooling of surface layer. The fast irradiation time varies from $10^{-5} – 10^{-12}$ sec depending on the laser types[23]. The

cooling rate of the surface layer is in the range of $10^9 – 10^{14}$ ℃/sec when annealed with pulsed laser[23].

The most common laser annealing technique is pulsed laser annealing, including, Q-switched solid state laser and mode-locked laser[23, 25, 30]. Pulsed laser means the optical power is not continuous but delivers in pulse at a repetition rate (i.e. 500 Hz). It is able to emit very high energy in a short plus. Pulsed laser anneals typically melt the Si surface, and the liquid phase epitaxial regrowth happens. The recrystallization/regrowth happens at the interface between the liquid layer and the crystal Si or amorphous Si, and the interface move towards the surface during the recrystallization[23, 25]. The recrystallization velocity is quite large because of the high temperature gradients across the melting surface[23]. Apart from the recrystallization, the melting of Si will lead to re-distribution of dopants[23, 25, 27, 28, 30]. The mobility of atoms is pretty fast in the liquid phase, as a result, the dopants diffusion will be severe. Even the dopants diffusion is undesired for the shallow junction devices, the re-distribution of dopants is favorable in making n-well and p-well of metal-oxide-semiconductor field effect transistor (MOSFET).

However, laser annealing of Si is not necessary to be the liquid phase recrystallization. The continuous wave laser, which has continuous wave and emits light continuously, can heat the ion implanted Si to a moderate temperature in less than 10^{-2} sec[23]. In this case, no liquid phase is formed, the amorphous Si undergoes solid phase crystallization in 10^{-2} sec[23]. However, the dopants do not have sufficient time to diffuse in such a short time[23]. This results in no measurable dopant diffusion, which is good for fabricating shallow junction devices.

1.2 Transparent Composite Thin-film

1.2.1 Indium Tin Oxide and Transparent Composite Electrode

Indium tin oxide (ITO) has been widely used as transparent conducting oxides (TCOs) in solar cells, flat-panel displays, organic solar cells and organic light emitting diodes[8, 31-33]. The large band bap of ITO thin film enables a high transmittance of 85-90% in visible light region [34]. Its low electrical resistivity ($< 10^{-4}$ Ohm·cm)[34] renders its popularity in the application of electrodes. However, ITO contains the rare earth element of indium, so its sustainability is limited for high volume manufacturing. In addition, TCOs on flexible substrate are also highly needed in flexible display and organic solar cells in order to achieve roll-to-roll fabrication of devices, but the deposition of ITO with a desired low resistivity needs the substrate above room temperature [35, 36] Hence, alternative TCOs without rare earth element and low deposition temperature are highly demanded.

The transparent composite electrode (TCE) is believed to be a promising alternative to ITO electrodes[8, 31, 32]. Compared to the ITO, TCEs are shown to have competitive optical and electrical properties[33, 37], while having a substantially lower cost of fabrication. An optical transmittance as high as 85% and a resistivity as low as 10^{-5} Ω·cm has been reported for TCEs[8, 31-33]. The TCE structure is comprised of a metal layer embedded between two transparent metal oxide (TMO) layers and it results in a TMO/metal/TMO composite structure [8, 9, 31-33, 37-44]. The materials selection for these TMO and embedded metal layers has significant effects on the optical and electrical properties of TCEs [9].

1.2.2 Optical and Electrical Consideration in TCEs

As a transparent conducting electrode, its resistivity has to be low enough to minimize its contribution to the series resistance of devices; meanwhile, light transmittance of the electrode has to be high enough to allow enough light to go through the electrode. In TCEs, the top and bottom transparent metal oxide layers are anti-reflection layers which is able to maximize the light transmission [45]. The desired transparent metal oxide should have a large band gap so that it is transparent in visible light region, meantime, the imaginary part of its refractive index should be as low as possible to avoid the light absorption. However, the TMO layers are typically quite resistive or not as conductive as the metal layer, as a result, the metal layer in TCE is responsible for the electrical conducting[45]. The low resistivity of metal layer can significantly contribute to lowering the resistivity of TCE. On the other hand, the low real part of metal film's refractive index is ideal for achieving high light transmittance in sandwiched TMO/metal/TMO structure[45, 46].

Apart from the nature of TMO and metal materials, the layer thickness of TMO and metal also affects the optical and electrical properties of TCEs. Increasing the metal layer's thickness can achieve lower resistivity, but the light transmittance will decrease accordingly. Therefore, there is a trade-off between the high transmittance and low resistivity when determining the thickness of metal layer. Typically, the metal layer is less than 20 nm to allow sufficient light transmission *Haacke* proposed a figure of merit

(φ_{TC}) to evaluate performance of the transparent conducting electrodes. *Haacke* figure of merit (FOM) takes into account of both thickness and transmittance [47]:

$$\varphi_{TC} = \frac{T^{10}}{R_s} \tag{1.4}$$

where, T is the transmittance and R_s is the sheet resistance. Typically, T is the average transmittance of the electrode across the visible light wavelength. Higher value of FOM represents better performance of the electrodes. A power of 10 is used because it is a favorable value that the impact of T is balanced with R_s, but not dominated over R_s.

Since the metal layer affects both the transmittance and sheet resistance, the performance of TCE is typically optimized and the high FOM value is achieved by varying the metal layer thickness. In the first stage of the metal film deposition, only separate nuclei are formed, these nuclei will gather into islands by surface diffusion, and these islands will gradually increase in the size, join one another and eventually form a continuous film [48]. The initial isolated islands explained why the very thin metal film is much more resistive than bulk metal. The conduction of the film starts at a critical thickness where a certain fraction of the metal filling is reached, and this fraction is called percolation threshold[49]. According to the percolation theory, the percolation threshold is where the initial separated clusters joined together to form a continuous cluster path enabling the current to flow through the film[49] ; therefore, the sheet resistance of film drops sharply at the percolation threshold. In the case of fabricating TCE, the metal layer has to be at or beyond the percolation threshold to achieve conductive film. Moreover, the isolated metal film embedded between TMO also reduce the transmittance of light

due to the light scattering effect of the isolated metal islands[31, 42, 44]. It is reported that the transmittance increases with the film thickness before the percolation threshold is reached. After the percolation threshold is reached the transmittance decreases as the thickness increase[31, 42, 44].

1.2.3 The Influence of Deposition Parameters on Properties of Film

Since the thickness and morphology of metal film have significant impacts on TCE's electrical and optical properties, the deposition has to be carefully controlled because the deposition condition affects the morphology of the films[50]. The deposition rate influences the size of grains. Higher deposition rate will form a metal film with smaller grain and less impurity, but high deposition rate will result in increased density of vacancies because they do not have enough time to leave the condensate [48]. In sputtering deposition, the deposition rate is controlled by the power and pressure; while, evaporation rate is controlled by the power solely.

The substrate temperature affects the grain size as well as the uniformity of the film. The higher temperature will increase the atoms diffusivity/surface mobility on the substrate, so that atoms tend to gather together and form larger grain size [48]. It is shown that the higher temperature will result in higher critical thickness where the percolation starts [48].

1.2.4 Prediction of the Optical Properties of TCEs

As mentioned above, the materials and layer thickness will affect the transmittance of TCE. Although the optimum TCE design and appropriate materials are

often found by means of trial and error, the high cost and involved time of this approach can impede the development of future TCEs. Building a proper TCE model to analytically predict its transmittance is therefore needed to facilitate materials selection and feature size design.

In its simplest form, the transmittance is defined as the ratio between the intensities of the transmitted and incident waves through a medium [51]. When light propagates in a TCE multilayer thin film, multiple reflections occur within each single layer. Hence, the total transmitted light through each layer becomes a summation of all the waves that are created due to directed transmittance and multiple reflections within the same layer and the previous ones[51-53]. It is arduous to derive the TCE's transmittance by analytically describing the multiple reflections in each layer. Invoking the transfer-matrix method can substantially simplify the calculations[52-56]. The transfer-matrix method has been widely used in terms of calculating the transmittance and reflectance of multilayer thin film structure[52-56]. In this approach, those waves (electric fields) that are propagating in the same direction and at the same side of an interface are represented by a single equivalent electric field, as shown in Figure. 1.2.

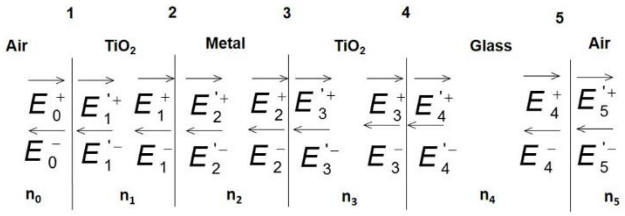

Figure 1.2 Schematic of light amplitudes and intensity within a TCE on glass. The subscripts signify the layer number; + and - signs represent forward and backward directions, respectively. A prime is used for waves at the right-hand side of an interface.

Then, the transmittance is calculated by relating the incident electric field and the ultimate transmitted electric field[52-56].

Considering a normal incidence of p-polarization wave, the wave propagation through interface 1 between air and layer 1 (top TiO_2 layer) shown in Figure. 1.2 is linked by transfer matrix L_{01}:

$$\begin{pmatrix} E_0^+ \\ E_0^- \end{pmatrix} = \frac{1}{t_{01}} \begin{pmatrix} 1 & r_{01} \\ r_{01} & 1 \end{pmatrix} \begin{pmatrix} E_1^{'+} \\ E_1^{'-} \end{pmatrix} = L_{01} \begin{pmatrix} E_1^{'+} \\ E_1^{'-} \end{pmatrix} \tag{1.5}$$

where, t_{01} and r_{01} are Fresnel transmission and reflection coefficients, respectively. E is the electric field propagating in corresponding direction and at corresponding interface. Wave propagation through layer 1 is linked by transfer matrix L_1:

$$\begin{pmatrix} E_1^{'+} \\ E_1^{'-} \end{pmatrix} = \begin{pmatrix} e^{-i\delta_1} & 0 \\ 0 & e^{i\delta_1} \end{pmatrix} \begin{pmatrix} E_1^+ \\ E_1^- \end{pmatrix} = L_1 \begin{pmatrix} E_1^+ \\ E_1^- \end{pmatrix} \tag{1.6}$$

where, $\delta_1 = 2n_1 d_1/\lambda$ is the phase change during the wave propagation through layer 1. It should be noted that n_1 and d_1 are refractive index and thickness of layer 1, respectively. Applying the same relations to the rest of the coherent interfaces and layers, the relationship of electric fields between a packet of coherent layers (TiO_2/Au/TiO_2), from medium 0 to right-hand side of interface 4, are related by the complete transfer matrix L_{04}:

$$\begin{aligned} \begin{pmatrix} E_0^+ \\ E_0^- \end{pmatrix} &= L_{01}L_1L_{12}L_2L_{23}L_3L_{34} \begin{pmatrix} E_4^{'+} \\ E_4^{'-} \end{pmatrix} \\ &= L_{04} \begin{pmatrix} E_4^{'+} \\ E_4^{'-} \end{pmatrix} = \begin{pmatrix} M_{11} & M_{12} \\ M_{21} & M_{22} \end{pmatrix} \begin{pmatrix} E_4^{'+} \\ E_4^{'-} \end{pmatrix} \end{aligned} \tag{1.7}$$

where, M_{ij} is the element in matrix L_{04}. The transmission and reflection coefficients of this coherent layer packet can be expressed by the elements of the above matrix L_{04}:

$$t_{04} = \left.\frac{E_4^{'+}}{E_0^+}\right|_{E_4^{'-}=0} = \frac{1}{M_{11}} \tag{1.8}$$

$$r_{04} = \left.\frac{E_0^-}{E_0^+}\right|_{E_4^{'-}=0} = \frac{M_{21}}{M_{11}} \tag{1.9}$$

$$t_{40} = \left.\frac{E_0^-}{E_4^{'-}}\right|_{E_0^+=0} = \frac{Det\,M}{M_{11}} \tag{1.10}$$

$$r_{40} = \left.\frac{E_4^{'+}}{E_4^{'-}}\right|_{E_0^+=0} = -\frac{M_{12}}{M_{11}} \tag{1.11}$$

Then, the elements M_{ij} in L_{04} can be replaced by transmission and reflection coefficients using the relations shown in Eqs. (1.8)-(1.11). The complete transfer matrix L_{04} then can be rewritten as:

$$L_{04} = \frac{1}{t_{04}}\begin{pmatrix} 1 & -r_{40} \\ r_{04} & t_{04}t_{40} - r_{04}r_{40} \end{pmatrix}. \tag{1.12}$$

When waves interact with the incoherent glass substrate, glass substrate is treated as incoherent layer, and the packet of coherent layers is treated as incoherent interface between air and glass substrate. The light intensity I (instead of electric field amplitude during the wave propagation) has to be used when deriving relationship of waves propagating through incoherent interfaces and layers; therefore, the transfer matrix is modified by replacing the transmission and reflection coefficients with their squared

amplitudes. The light intensity between the mixed coherent and incoherent multilayers system is linked by the complete transfer matrix for mixed layers M^{incoh}:

$$\begin{pmatrix} I_0^+ \\ I_0^- \end{pmatrix} = L_{04}^{incoh} L_4^{incoh} L_{45}^{incoh} \begin{pmatrix} I_5^{'+} \\ I_5^{'-} \end{pmatrix} = M^{incoh} \begin{pmatrix} I_5^{'+} \\ I_5^{'-} \end{pmatrix} \tag{1.13}$$

$$M^{incoh} = \frac{1}{|t_{04}|^2} \begin{pmatrix} 1 & -|r_{40}|^2 \\ |r_{04}|^2 & |t_{04}t_{40}|^2 - |r_{04}r_{40}|^2 \end{pmatrix} \bullet \begin{pmatrix} |e^{-i\delta_4}|^2 & 0 \\ 0 & |e^{i\delta_4}|^2 \end{pmatrix} \bullet \frac{1}{|t_{45}|^2} \begin{pmatrix} 1 & -|r_{54}|^2 \\ |r_{45}|^2 & |t_{45}t_{54}|^2 - |r_{45}r_{54}|^2 \end{pmatrix} . \tag{1.14}$$

In addition, rough surface and interface will lead to light scattering and reduce the light transmittance. For the roughness of layer surface and interface, the scattering factor s^r and s^t during reflection and transmission has to be considered in the matrix calculation as well[57, 58].

$$t'_{i-1,i} = t_{i-1,i} \cdot s^t_{i-1,i} = t_{i-1,i} \exp\left[-\frac{1}{2} \left(\frac{2\pi (n_{i-1} - n_i)\sigma_i}{\lambda} \right)^2 \right] \tag{1.15a}$$

$$r'_{i-1,i} = r_{i-1,i} \cdot s^r_{i-1,i} = r_{i-1,i} \exp\left[-\frac{1}{2} \left(\frac{4\pi n_{i-1}\sigma_i}{\lambda} \right)^2 \right] \tag{1.15b}$$

where $t'_{i-1,i}$ and $r'_{i-1,i}$ are modified Fresnel transmission and reflection coefficients, respectively. n is the real part of the refractive index, and σ_i is the RMS roughness of interface i. The final transmittance T_{05}, the transmittance of TCE with the consideration of interface scattering, is expressed by the modified elements in the transfer matrix M^{incoh} in Eq. (1.14):

$$T_{05} = \frac{I_5^{'+}}{I_0^+} = \frac{1}{M_{11}^{incoh}} = \left|t_{04}^{'}\right|^2 \frac{\left|t_{45}\right|^2}{1-\left|r_{40}^{'} r_{04}\right|^2} \tag{1.16}$$

where t_{04}', r_{40}', r_{04} are calculated using Eq. (1.8), (1.10), (1.15a) and (1.15b), and t_{45} is the Fresnel transmission coefficient for waves going from glass and air.

Hence, the transmittance is a function of layer thickness, refractive indices and roughness. Via transfer-matrix method, the dependence of light transmittance spectrum on materials, layer thickness can be calculated easily and quickly. It expedites the design of TCE, and facilitate the study of the materials' impact on light transmittance.

1.3 Organic Solar Cells

1.3.1 Current Solar Technology

As a result of increasing demands in the energy but limited resources on earth, solar power becomes one of the most promising clear and sustainable energy. Solar cell, which is one of the solar power technologies, has been intensively studied in many decades. The current solar cell technologies include: crystalline and multi-crystalline silicon based solar cells, inorganic thin film solar cells, dye-sensitized solar and GaAs solar cells, organic solar cells and perovskite solar cells[59].

The power conversion efficiency of solar cells is the fraction of incoming light power to the converted electrical power, and it determines the performance of solar cells. Due to the relatively high power conversion efficiency, solar cells based on crystalline and multi-crystalline silicon attract most of the interests. They have been commercialized in the last decades and takes 80% of the commercialized solar cell market[59]. However, the high cost of silicon wafer accounts for 50% of entire cost of solar cells[59]. This high cost of silicon based solar cell impends its wide-spread utilization. On the other hand, GaAs solar cells, which are III-V crystalline solar cells, propose the highest efficiency but the high cost of GaAs solar cell limits its application only in aerospace[59].

Inorganic thin film solar cell is also the commercialized solar cell. Even though the thin film solar cell suffers from its low efficiency, the low cost of thin film fabrication and low processing temperature makes it very competitive to silicon based solar cell[59].

Dye-sensitized solar cells are based on organic materials. The organic dye is coated on the porous electrode that has high surface area. As a result, the light absorption

is maximized by the porous electrode, and the efficiency can go up to 11%[59]. However, dye-sensitized solar cells contain liquid electrolyte which will cause reliability and portable issue[59], as a result, they are not suitable for commercialization.

Organic solar cells (OSCs) benefit from its low process temperature, light weight flexible substrate and high throughput process. Even though the highest efficiency of organic solar cells is only about 11%[60], the roll to roll printing of organic solar cell enable the high volume and low cost manufacturing. As a result, intensive studies have been done to improve its efficiency by modify the interfaces, polymer structure and replace electrodes.

1.3.2 Working Mechanism

A solar cell convert to solar energy into to electricity by generating electrons and holes and transporting these charges to the external circuit. To generate the electrons and holes pairs, band gap is need in the material, *i.e.* semiconductor material. When the light energy is higher than the band gap, the light will be absorbed by the material. The absorbed light energy will excite the electrons from the lower energy states to the high energy state leaving holes behind. The photo-generated carriers has to be pulled toward the external circuit by electric field before they recombine, so that the photo-current can be collected by the external circuit. In silicon solar cell, that electric field is provided by the built-in potential/voltage in p/n junction. The photo-excited electrons and holes that are generated in both n-type and p-type silicon are pulled to the corresponding electrode by the built-in potential in p/n junction.

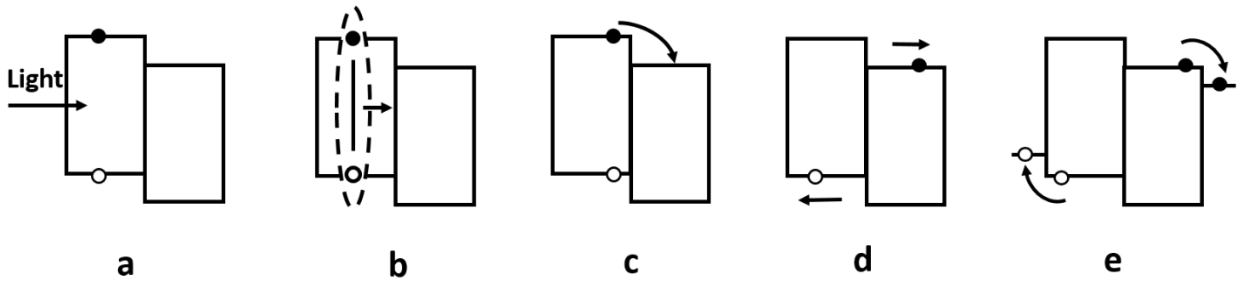

Figure 1.3 The schematic for photocurrent generation in organic solar cells: a) generation of exciton under light; b) exciton moves towards interface of donor and acceptor; c) dissociation of exciton at interface; d) electron and hole move towards cathode and anode, e) electron and hole are collected by cathode and anode.

Semiconducting polymers are analogous to conventional inorganic semiconductors. The highest occupied molecular orbital (HOMO) and the lowest occupied molecular orbital (LOMO) are equivalent to the valence band and conduction band, respectively[59]. The energy gap between HOMO and LOMO is equivalent to the band gap. Most of the semiconducting polymers are conjugated polymers and they are able to generate excited states after absorbing light[59]. The photocurrent generation process is shown in Figure. 1.3. The excited states are excitons that are bound electron-hole pairs. The organic solar cells consists of donor and acceptor. The donor polymer materials generate excitons after absorbing light. The excitons have to be separated into free electrons and holes by an effective field at donor and acceptor interface[61]. The organic semiconductor contains π molecular orbitals, in which the π electrons are loosely bound and can easily move along the backbone of the molecules/polymer[62]. After electron-hole pairs dissociate at the interface, the photo-generated electrons and holes can be transported though the overlapped π molecular orbitals between molecules. The electrons go to the LOMO of acceptor and diffuse to the cathode. Holes migrates at the

HOMO of donor and diffuse to the anode. In the end, they become conducting current in the external circuit. The crystallinity of organic semiconductors affects its long range charge carrier transport[63].

1.3.3 Heterojunction Organic Solar Cells

As discussed above, the effective filed is needed to disassociate excitons[61]. The heterojunction organic solar cells are designed to create the effective field at the interface (heterojunction) between donor polymer and acceptor polymer. The ionization potential difference and electron affinity difference between donor and acceptors create the effective field at the interface which separates the electron-hole pairs in the excitons.

However, the diffusion length and lifetime of excitons will impact efficiency of charge separation. The diffusion length of exciton is only about 10 nm[64]. As a result, the excitons that are generated more than 10 nm away from the donor/acceptor interface will decay to their ground state before they reach and dissociate at the interface. Instead of using planar heterojunction solar cells, bulk heterojunction (BHJ) solar cells are proposed to maximize the charge separation. The donor and acceptor polymers are mixed together and form an interpenetrating network as shown in Figure. 1.4. As a result, the most of the photo-generated excitons are able to diffuse to the nearby interface before decay. Moreover, the interface area increases by mixing donors and acceptors together, therefore the carrier generation centers increase dramatically.

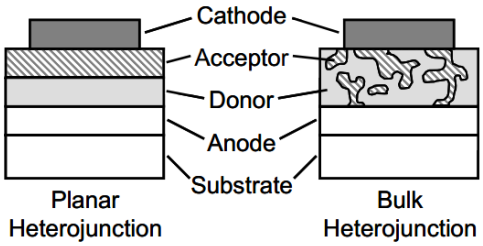

Figure 1.4 The schematics of planar heterojunction and bulk heterojunction solar cell[59].

The most widely used donor and acceptor polymers in bulk heterojunction solar cells are poly 3-hexylthiophene (P_3HT) and [6,6]-phenyl C_{61}-butyric acid methyl ester (PCBM). These two polymers are dissolved together and the phase-separation between them creates the intermixing structure. The layer contains the intermixing structure of donor and acceptor is called active layer. As mentioned before, the diffusion length of the excitons has diffusion length about 10 nm, so that the donor domain size has to be limited to within this diffusion length so that the excitons can reach the domain interface before they vanish. The control of domain size during the phase-separation is very important, and the domain size can be tailored by changing the baking temperate of the mixture, solvent vapor treatment, and high boiling point additive[65].

It has been observed that the separated electrons and holes need clear paths to go to their corresponding electrodes, and the path formation depends on the extent of the phase separation. If the path is not continuous, the electrons and holes will be recombine before they reach their corresponding electrodes. Hence, the time and temperature determining the extent of phase separation of donor and acceptor polymers are quite important. In addition, the holes in the donor phase that is in touch with the cathode have a chance to recombine with electrons collected by the cathode[65]. Similar recombination

will happen near the anode. As a result, ordered or graded BHJ is suggested. In graded BHJ, the continuous donor and acceptor phases are interlocked and has vertical phase separation, so that donor and acceptor phases are in direct contact with their corresponding electrodes[65]. Donor phase is rich at anode region while the cathode has the acceptor phase rich region. The graded BHJ can be fabricated by self-assembly of melecules or surface modification of substrate[65].

1.3.4 Interface Engineering in BHJ Organic Solar Cells

Apart from using bulk heterojunction to achieve better efficiency, hole transport layer and electron transport layers are also added to improve the power conversion efficiency. Hole transport layer are typically added to modify the energy level alignment between anode (typically indium tin oxide) and the HOMO of donor materials, and to facilitate the hole extraction from the active layer to electrode[66]. The most widely used hole transport layer is poly(3,4-ethylenedioxythiophene) polystyrene sulfonate (PEDOT:PSS). Lots of alternatives for PEDOT:PSS are also developed, including Polypyrrole-polystyrene sulfonate (PPy:PEDOT), copper iodide, graphene oxide, semiconducting transition metal oxide [67-71]. Similarly, the interface between cathode and active layers is modified by insertion of an electron transfer layer. It is reported that LiF is added between cathode (typically aluminum) and active layer to improve the electron ejections [66]. Apart from that, bathocuproine (BCP) is used as an exiton blocking layer between metal cathode and organic active layer[72, 73]. This blocking can prevent the exciton diffusing to and vanishing at the electrode, instead, the photo-generated excitons will dissociate at the nearby heterojunction interface[73].

1.3.5 Basics of Organic Solar Cells

1.3.5.1 *J-V* Curve

In the dark, solar cell is acting as a regular diode. If reverse bias is applied, there will only be small amount of current. If forward bias is applied, the junction barrier become small, then large current can be achieved after electrons overcome the small junction barrier. Under illumination, excitons will be generated and dissociate at the interface. Electrons will go to the cathode and holes will go to the anode, resulting in negative current. When the external potential is negative, namely under reverse bias, the built-in potential in the solar cell will be enhanced. The enhanced the built-in potential in turn enhances the charge dissociation, and results in large photo-current[74]. Moreover, the strong electric field results in the drift current[74]. When the applied negative bias gradually decreases, the drift current will become smaller[74]. Carriers are driven to their corresponding electrodes mainly by the internal built-in field[74]. When the applied bias turns to forward bias and equal to the built-in field, the current will mainly be the diffusion current. As the forward bias keeps increasing, the external potential is larger than the built-in field, and the potential gradient across the devices is reversed. As a result, the holes will be ejected from the anode to the cathode, leading to a positive current. The internal field under different bias is shown in following Figure. 1.5.

This characteristics of current under dark and light can be illustrated by the plot of the current density (*J*) as a function of voltage as shown in Figure. 1.6. The current always depends on the area that absorb light, in order to eliminate the area dependence, the *J* instead of current (*I*) is used in the plot.

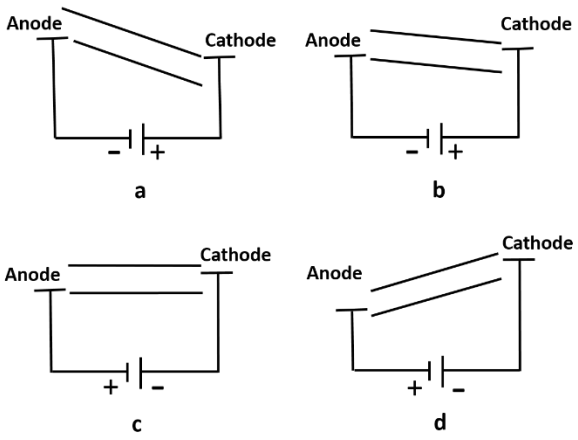

Figure 1.5 Operation of OSC at different bias: a) large revers bias; b) small reverse bias; c) small positive bias, zero internal field; d) large positive bias[74]

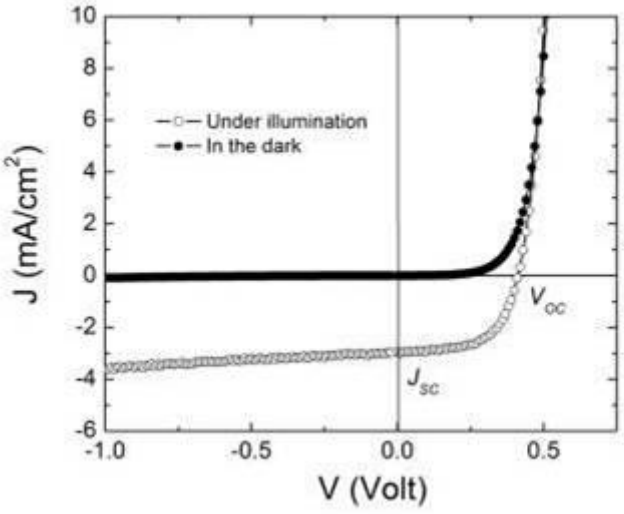

Figure 1.6 Current density (*J*) as a function of voltage (*V*) for organic solar cells

1.3.5.2 Short Circuit Current Density (J_{sc})

J_{sc} is defined as the current density when the external bias is zero[59]. At zero external bias, drift current due to the external electric filed disappears and only the build-in field drives the photo-generated carriers to their corresponding electrodes. The J_{sc}

determines how efficiently the photo carriers are generated in the active layer and collected by the electrode. The series resistance in the solar cell, the thickness of the active layer, light input affects J_{sc}[70, 71, 75].

1.3.5.3 Open Circuit Voltage (V_{oc})

V_{oc} is defined as the voltage when the output current density is zero. Theoretically, the current is close to zero when the external bias is same as the built-in field because few excitons are dissociated due to the absence of electric field. In this case, only diffusion current exists and it is almost negligible. V_{oc} relates to the built-in electric field in the solar cell and is mainly determined by the intrinsic properties of the active layer. It is reported that V_{oc} depends on the energy difference between HOMO of donor and LUMO of acceptor if ohmic contacts are formed at the electrode[74]. For non-ohmic contact, V_{oc} is determined by metal-insulator-metal model, and equals to the work function difference of the two electrodes[71].

1.3.5.4 Fill Factor (*FF*)

The quadrant IV of *J-V* curve represents the power generation[59]. The theoretical maximum power is the product of J_{sc} and V_{oc}. However, the practical power density of solar cell is the product of J_{max} and V_{max}. J_{max} and V_{max} are at the point where the output power density is maximum[59, 74]. Fill factor is defined as the ratio of the practical maximum power density output to the theoretical maximum power density output[59, 74]:

$$FF = \frac{J_{\max} V_{\max}}{J_{sc} V_{oc}} \tag{1.17}$$

The physical meaning of FF is how rectangular the J-V characteristic curve is[65]. If the FF is 100%, the photo-generated current remains constant as the external bias increases up to V_{oc}. In reality, the photo current typically decreases as the external bias increase, therefore the FF is less than 100%. In fact, the recombination in the OSC which reduces the photo current has a significant effect on FF. There are two kinds of recombination: geminate pair recombination and bimolecular recombination[65, 71].

The geminate pair recombination is that electrons and holes in the excitons recombine at the donor/acceptor interface before they split into free charges[71]. As the internal filed is weakened by the increasing external bias, the chance of geminate pair recombination increases, leading to the reduced photo current and FF[71]. This recombination is mainly determined by the donor domain size[71]. In addition, the LUMO offset between the LUMOs of donor and acceptor is important in geminate pair dissociation and recombination[71]. The LUMO offset is helpful in the electron transfer process right after the exciton split, and also in the free charge photo-generation. It is reported that the high LUMO offset can result in high FF and photo current[71].

The bimolecular recombination happens after the excitons split into free carriers, and this usually occurs at the anode/active layer interface when the anode is in direct contact with acceptor[71]. For examples, as the external bias increases to high voltage, the built-in potential/electric field that separates the electron-hole pairs will be weaken, diffusion electrons towards the anode is stronger than the drift electrons toward the cathode, and lots of the diffusion electrons will recombine with the holes in the anode, leading to the reduced photo current and FF[71]. This kind of recombination can be reduced

by adding the electron blocking layer (EBL)[71]. The EBL typically has high energy level of LUMO/conduction band[71], higher than the LUMO of acceptor. In this case, the diffusion electrons in acceptor's LUMO towards the anode will be blocked by the EBL before they enter the anode.

1.3.5.5 Power Conversion Efficiency (*PCE*)

PCE determines the performance of the solar cells. It is defined as the fraction of the input light power is converted into output electricity power [59]:

$$PCE = \eta = \frac{J_{sc} V_{oc} FF}{P_{in}} \times 100\% \qquad (1.18)$$

where P_{in} is the input light power density.

1.3.5.6 Resistive Effects

In practice, parasitic resistances exist in solar cells and reduce the PCE. Shunt resistance and series resistance are the two man parasitic resistances and shown in the equivalent circuit model of solar cells (Figure. 1.7)[76].

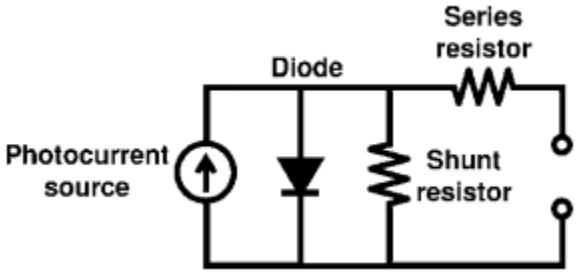

Figure 1.7 Equivalent circuit model of solar cell[76]

In this conventional equivalent circuit model of solar cells, photocurrent source represents the photocurrent generated by the solar cell. The diode is responsible for the dark current. The resistance of shunt resistor (R_{sh}) accounts for the leakage current due to the defects in the solar cell[76]. The resistance of series resistor (R_s) gives the internal resistance of the cell itself. This current density (J) in above model is mathematically represented by following equation[76]:

$$J = J_0\left[\exp\left(\frac{e(V - JR_s}{nk_BT}\right) - 1\right] + \frac{V - JR_s}{R_{sh}} - J_{ph} \tag{1.19}$$

where J_0 is the reverse bias saturation current density, e is the elementary charge, R_s is the series resistance, n is the diode ideality factor, k_B is the Boltzman's constant, T is temperature, and R_{sh} is shunt resistance. For ideal p-n junction diode, the J_0 represents the ideal saturation current density at reverse bias, and ideality n equal to 1[76]. The R_s and R_{sh} are can be calculated by fitting dark current of the solar cell with the Eq. xx. At low voltage, the dark J-V characteristics are mainly determined by R_{sh}, while the J-V characteristics at high voltage (above V_{oc})[76]. As rules of thumb, R_s, is estimated by the reciprocal of the slope in linear region of dark J-V at high voltage[76]. Another rule of thumb to estimate is using the illuminated J-V curve. R_{sh} is calculated by the reciprocal of the slope at zero voltage. R_s is calculated by the reciprocal of J-V slope at V_{oc}.

It is noticed that the OSC deviate from the model for tradition solar cell[76]. Hence, the rule of thumb for calculating R_s and R_{sh} is just a rough estimation. Accurate R_s and R_{sh} has to be estimated by the fitting the dark current using Eq. xx. It is reported that R_s of OSC shows dependence on the external field[76]. As a result, the fitting to the tradition

model should be near the cell operating voltage (V_{oc}) over a tight range (~400 mV)[76]. In addition, it is reported that R_s of OSC also shows dependence on the device area[76]. The smaller device area usually ends up with a smaller R_s. R_s have a significantly impact on J_{sc}, and is mainly affected by the interface at electrode/active layer, and resistance of each individual layer.

1.4 Printed Ag Thin-films

1.4.1 Reactive Ink and Printed Ag Thin-film

Printed metal thin-films have the potential for broad application and ease of use. Drop-on-demand (DOD) can be achieved by printing technology. Reactive inks are a new approach to DOD printed electronics that are easy to synthesize and that often do not require high-temperature sintering.[77, 78]. As a result, the photovoltaic industry have adopted silver inks for their metallization schemes[79]. Other application of reactive inks includes printed electronics[80] and stretchable electronics[78]. Reactive inks consist of dissolved metal salts, chelating agents, reducing agents, and solvent. Unlike traditional inks that print clusters of particles, reactive inks print chemical precursors that react to form a solid material.[80, 81] Hence, reactive inks are also called metal-organic complex inks, self-reducing inks [77]. The reactions to form solid material can be initiated by elevated substrate temperatures (thermally), solvent or stabilizing agent evaporation (chemically), or by some increased catalytic activity of the substrate (kinetically).[80, 82-88] Recent advances in silver,[80] copper,[81] and aluminum[84, 89] reactive inks have brought the reaction temperatures of these inks to below 180 ˚C and to even room temperature for silver-diamine based inks[77, 90, 91]. Compared to silver paste and nanoparticle-based inks, these new reactive inks provide superior conductivities (that are close to bulk material values) at lower temperatures and significantly lower costs.

The low temperature printing and reaction of silver-diamine based ink is based on Tollen's reaction as demonstrated by Walker *et al*.[77]. The silver-diamine inks is made up of silver acetate that dissolved in ammonium hydroxide with formic acid as the reducing

agent [77]. First, excess ammonia can enable the formation of stable diaminesilver (I) complex as follows [77]:

$$2AgCH_3CO_2 + 2NH_4OH \xrightarrow{H_2O} Ag_2O + 2NH_4CH_3CO_2 + H_2O,$$

$$Ag_2O + 4NH_3 + 2NH_4CH_3CO_2 + H_2O \xrightarrow{NH_3/H_2O} 2Ag(NH_3)_2CH_3CO_2 + 2NH_4OH.$$

The diaminesilver (I) cations, acetate anions and formate anions are mixed together and is stable with excess ammonia [77]. Once the excess ammonia evaporates after printing, the reduction of silver diamine to silver and silver acetate is triggered [77]. As a result, the printed Ag thin-film is obtained. The reaction is following [77]:

$$2Ag(NH_3)CH_3CO_2 + NH_4CO_2 \xrightarrow{\Delta} 2Ag + 5NH_3 + 2CH_3CO_2H + CO_2 + H_2O,$$

$$2Ag(NH_3)CH_3CO_2 + NH_4CO_2 \longrightarrow Ag + AgCH_3CO_2 + 5NH_3 + CH_3CO_2H + CO_2 + H_2O.$$

The solvent in the reactive silver ink can adjust viscosity, evaporation rate and surface tension for DOD droplet stabilization. The solvent and sintering temperature will affect reduction rates and morphology of the printed structure [77]. It is shown that the reactive inks currently print porous materials with a large volume-fraction of voids [77] due to the evaporation of solvent. By adjusting the sintering temperature (22 ^{o}C to 105 ^{o}C), solvent (ethanol, 2,3-butuanediol) and the ratio of solvent to silver acetate, the porosity can be reduced from 93% to 50% and the media resistivity is reduced to 1.8 μΩcm [77].

1.4.2 Electromigraion

Considering the porous nature of printed Ag, the reliability is a big concern. In this study, the reliability characterization regarding the electromigration of printed Ag will be studied. The electromigration happens when the current flow in metal lines for a long period of time. Due to motion of electrons, the momentum of the electrons transfer

to metal ions and push the ions to move [2]. This is called electron "wind" effect, and is the root cause for electromigration. The electrical force applied on metal ions due to the electric field can also play a role in electromigration [2]. The motion of the ions will results in the voids formation in one end of metal line and the hillocks at the other end [2]. The voids lead to reduction of metal line area, increase in the line resistance, and eventually the break of metal line. The voids typically form at the grain boundary and triple points since they are the region of imperfection and accumulation of vacancies [2]. Metal diffusion happens mainly through vacancies [2]. The median time to failure (t_f) for the elctromigration on solid metal line are typically predicted by Black's equation [2]. This equation is based on the assumption that the rate of mass transport is directly proportional to the momentum of electrons, to the number of activated ions, and to the number of electrons, and to the effective target cross-section [2]:

$$t_f = A_B J^{-n} \exp\left(-\frac{E_a}{k_B T}\right) \tag{1.20}$$

where A_B is a constant related to line cross-sectional area, J is the current density in A/cm^2, n is the current-density exponent, E_a is the activation energy in eV, k_B is Boltzmann's constant and T is the substrate temperature in Kelvin.

1.5 Summary

It has been more than 60 years since the invention of the first transistor[92] . The semiconductor industry has been well developed over the 60 years. Integrated circuits and photovoltaic technologies are parts of the semiconductor industry. The economics of

semiconductor industries drives the innovation of new processing method and material in order to lower the cost of fabrication or to improve the devices' performance. My research is focus on the characterization of novel thin-films in the integrated circuits and photovoltaic techniques.

Chapter 2 will be the study of ion implanted thin-film and microwave annealing technology. The rapid thermal annealing (RTA) is the most widely used method to repair damages, and active the implanted dopants in the ion implanted Si. Microwave (MW) annealing proposes fast, volumetric heating, and results in less dopants diffusion, so it is a promising alternative to rapid thermal annealing in terms of fabricating shallow junction devices. This study will be mainly focus on the electrical and structural characterization of MW annealed B^+, P^+ and As^+ implanted Si. During MW annealing, P^+ implanted samples show better dopant activation, recrystallization and less dopant diffusion than B^+ implanted samples. It is shown that the microwave annealing has advantages over RTA. The As^+ implanted samples are annealed by RTA and MW annealing using the similar heating curve/thermal budget. MW annealing results in lower sheet resistance and better extent of dopant activation than RTA does. On the other hand, when MW annealing and RTA results in same dopant activation in P^+ implanted samples, MW annealing achieves no measurable dopant diffusion in a short time and at lower temperature, as compared to RTA. In terms of boron implanted Si, MW annealing shows more efficient dopant activation than RTA, be still has dopants diffusion in the end of the dopant profile.

Chapter 3 will be the electrical and structural characterization of laser annealed and MW annealed of ion implanted Si. The dopant activation of As^+ implanted Si annealed are compared in regards to the energy absorbed during laser annealing and MW annealing. Laser annealing shows advantages for dopant activation. The two techniques show the same performance with respect to re-crystallization. The dopant depth profiles achieved by MW annealing and laser annealing have different characteristics that make them suitable for different applications. Laser annealing appears to be beneficial for annealing n-wells and p-wells for complementary metal-oxide semiconductor (CMOS) devices. Susceptor-assisted MW annealing is good for annealing source and drain regions in MOSFETs.

Chapter 4 will cover the study of transparent composite electrode (TCE), a promising alternative to ITO. Indium-free TCE has been studied a lot due to their low coat and room temperature fabrication. This study mainly focuses on the numerical prediction of optical transmittance of $TiO_2/Ag/TiO_2$ by transfer matrix method. Factors that affect the accuracy of prediction results are studied. When the metal layer become ultra-thin, the predication will deviate from the measurement. The morphology of ultra-thin Ag layer in TCE is studied to explain the deviation. It is shown that plasmonic nature of discontinuity of ultra-thin metal layer lead to enhanced optical absorption caused by localized surface plasmons. The predicted transmittance will deviate from the real transmittance when the TCE contains discontinuous Ag layer. However, the transfer matrix method is able to successfully predict the optical transmittance of TCE that have continuous Ag layer, and also able to roughly predict the transmittance dependence on layer thickness and estimate the optimal layer thickness for specific applications.

Chapter 5 will be the future work on fabricating and characterization of TCE tailored to P3HT:PC_{61}MB organic solar cells (OSCs). The characterization of TCE mainly focus on its optical and electrical properties, which are the major concerns in solar cell application. The optical absorption peak of P3HT:PC_{61}MB in OSC is between 450 nm to 600 nm. TiO_2/Ag/TiO_2 electrode is selected as the candidate of anode in OSC. To maximize the light input to the active layer, the Haacke figure of merit for TiO_2/Ag/TiO_2 electrode is optimized between 450 nm to 600 nm, including optimizing the Ag deposition rate, thicknesses of Ag and TiO_2 layers. The optimal layer thickness is first estimated by transfer matrix method to narrow down the range of layer thickness for experimental fabrication. TCEs with layers that is within estimated optimal thickness range are fabricated. Their transmittance and sheet resistance is characterized and compared with ITO. The optimal layer thickness and deposition rate is determined and TCE with optimal layer thickness shows much higher device-specific Haacke figure of merit than ITO.

Chapter 6 will focus on the fabricating P3HT:PC_{61}MB organic solar cell on TiO_2/Ag/TiO_2 (TAgT) electrodes. TAgT as an alternative of ITO, is successfully incorporated into OSCs. The compatibility of two different HTLs (PEDOT:PSS and MoO_3) with TAgT anode are studied. The impact of HTL on OSC's performance, especially on J_{sc}, are studied by characterizing its contact at anode and active layer interfaces, and its wettability effect on active layer thickness. When using PEDOT:PSS as HTL, PCE of TAgT based OSC is worse than that of ITO based OSC. This is because TAgT is very vulnerable to PEDOT:PSS's attack, which results in an extremely high sheet resistance in TAgT after PEDOT:PSS deposition. However, when MoO_3 is

employed as HTL, MoO_3 form ohmic contact with both ITO and TAgT anodes. As a result, MoO_3 as HTL is more compatible with TAgT because it does not attack the metal oxide in TAgT and forms ohmic contact with TAgT. To compare the performance of TAgT anode with ITO anode, ITO based OSCs using PEDOT:PSS and MoO_3 as HTLs are fabricated at the same time as control samples. Specifically, the impact of light transmittance and sheet resistance of two different anodes on the light input and seriers resistance (R_{series}) of OSC are studied. It turns out that the different light transmittance of the two anodes does not have an impact on the device's light absorption and PCE.

Chapter 7 focus on the characterization of printed Ag film, especially the electromigration reliability. The printed Ag thin film shows porous natural. We study the failure mechanisms of silver lines that were printed using a low-temperature, self-reducing, silver-diamine based ink (RSI). These studies demonstrate that Black's equation does not suitably account for morphology-induced current crowding when predicting the lifetimes of printed silver or other porous conducting elements. Overall, a percolation based model is proposed that can take into account the effects of physical structure, mass-transport, and other degradation mechanisms that can impact the lifetimes of porous or "imperfect" printed electronic devices. We demonstrate that percolation-based model (for predicting the electromigration failure time) is suitable for predicting the increase in resistance of porous conducting lines under a current bias.

Chapter 8 is about the future work on using TCE for inverted organic solar cells.

2. ELECTRICAL AND STRUCTURAL CHARACTERIZATION OF ION IMPLANTED SILICON ANNEALED BY MICROWAVE AND RTA

2.1 Introduction

In integrated circuit manufacturing, dopants are introduced into the substrate wafer and are then activated to alter the resistivity of the wafer surface [93]. Methods of dopant introduction include diffusion and ion implantation. The most commonly used method is ion implantation. With this technique, dopant atoms are ionized, accelerated to energies of 30-100 keV or higher, and then bombarded into the wafer[5]. During this process, a large number of vacancies and interstitials, and a disordered array of atoms are created at and near the wafer surface, typically leading to the creation of an amorphized layer [5]. To remove this implant damage, the wafers are annealed at elevated temperatures and dopant atoms are also electrically activated as they move into substitutional sites in Si lattice.

Anneal methods, which are widely used to achieve recrystallization, include laser annealing, rapid thermal annealing (RTA), and metal induced crystallization (MIC) [11, 12, 24, 29]. However, laser annealing suffers from non-uniform heating and surface melting, and MIC introduces contaminants during annealing. Driven by the International Technology Roadmap for Semiconductors (ITRS), device features and electrical junction depths are being scaled down significantly [94], necessitating precise control over position of dopant atoms in the devices. The low energy implantation could create a shallow junction, however, the post implantation thermal annealing will cause the dopants diffuse towards the substrate so the junction is not that shallow any more. In addition, minimization of dopant diffusion during the annealing processes is required. RTA, which

aims to minimize the diffusion of dopants by use of a steep temperature ramp [13] and reduced duration of anneal, still causes an undesirable amount of end-of-range diffusion [95]. On the other hand, it has been reported that susceptor-assisted microwave annealing (MWA) minimizes end-of-range diffusion while creating a high quality recrystallized Si layer in As^+ implanted Si wafers, in a short time [10].

In this study, susceptor-assisted MWA is used for electrical activation while minimizing the diffusion of dopant atoms into the substrate, when compared with RTA. For As^+ implanted Si, similar heating curves/thermal budgets of MWA and RTA are conducted. MWA achieves more efficient dopant activation than RTA does. The mechanism responsible for the observed better electrical activation achieved by MWA at low temperature is discussed. This study also elucidates the evolution of extended defects in boron implanted silicon, and correlates the defects with features observed in RBS/ion channeling spectra. Dopant diffusion is compared between samples that have almost the same resulting dopant activation after MWA and RTA.

2.2 Experimental

Silicon n-type wafers of (001) orientation with a resistivity range of 1-5 Ω-cm were implanted with boron (acceptor) atoms. The implantation was performed with an energy of 15 keV and doses of 2, 3, and 4×10^{15} cm^{-2} to achieve shallow as implanted junction. The expected range (R_p) calculated using SRIM was 58.7 nm [96]. The other set of (001) oriented, 1-5 Ω-cm p-type Si wafers was implanted with phosphorus (donor) atoms using the same energy and dosages as the boron implants, for an expected range (R_p) of 23.5 nm [96]. High energy arsenic implanted Si was also prepared. Arsenic ions were

implanted into (001) orientated Si wafers that are p-type boron doped. The implantation was performed with an energy of 180 keV and doses of 2×10^{15} cm^{-2}. During the implantation, the all wafers were titled at 7 °off the incident beam to minimize ion channeling.

A 2.8×10^{4} cm^{3} cavity microwave oven was used for post-implantation annealing with single frequency 2.45 GHz microwaves generated by a 1200 W magnetron source. All MWA were performed by mounting the samples onto a SiC susceptor. SiC is a high dielectric loss material, as a result of which, it strongly absorbs microwaves and can efficiently convert the microwave energy into heat. The susceptor heats up and then provides conductive heating to the ion-implanted silicon samples, causing the samples to ramp up to high temperatures [10, 97]. The surface temperature of the samples was monitored in-situ as a function of time, using Raytek Compact MID series pyrometers. The emissivity of the samples was estimated by calibration of the pyrometer's temperature reading against temperature measured by a thermocouple. To cover the large temperature range used in annealing, two pyrometers were used with measurement temperature ranges of 0-600 ℃ and 200-1000 ℃. The anneal time for boron implanted samples ranged 60-400 seconds and the corresponding surface temperature range was 663-747 ℃. The anneal time for phosphorus implanted samples ranged 10-240 seconds and the corresponding surface temperature range was 294-740 ℃. The anneal time for arsenic implanted sample was 50 seconds and 100 seconds and the highest surface temperature is 575 ^{o}C and 814 ^{o}C, respectively. RTA was compared with MWA. In RTA, samples were annealed in N_2, using a Tamarack 180M RTA oven, for various anneal time and temperature combinations.

Activation of dopant atoms, recrystallization, and diffusion effects were investigated by several characterization techniques. To estimate the extent of dopant activation, the sheet resistance (R_{sh}) of each sample was measured using a 4-point probe system equipped with a 100 mA Keithley 2700 digital multimeter. Hall measurements were also conducted to estimate the carrier concentrations as well as to determine the fraction of activated dopants. Indium was deposited to form Ohmic contacts on the Si samples, and then the samples were placed on a printed circuit board for measurements using a Van de Pauw method under a magnetic field of 5000 Gauss.

The presence of implantation damage and the extent of recrystallization after annealing were assessed by ion channeling based on Rutherford Backscattering Spectrometry (RBS) of as-implanted and annealed samples. A 2 MeV He^+ ion beam was focused on the samples along [001] channeling and random directions. The resulting RBS spectra were plotted using computer software, RUMP. In addition, the crystal structure of as-implanted and MWA samples were examined using Raman spectroscopy. A 532 nm argon laser beam was directed upon the samples and the resulting light was reflected into a Sopra 2000 2m double spectrometer with a 50% beam-splitter, and then collected using a 60 pixel/cm energy dispersion CCD Camera [98].

To investigate the presence and evolution of defects, transmission electron microscopy samples were prepared using a Nova 200 NanoLab focused ion-beam tool. The microstructure of the samples before and after annealing was evaluated using cross-section transmission electron microscopy (XTEM) with a beam energy of 200 keV.

Diffusion of dopants was investigated using secondary ion mass spectroscopy (SIMS) profiles from as-implanted and MWA samples. SIMS was also performed on RTA treated samples to compare the extent of diffusion in both MWA and RTA samples. Boron and phosphorus signals were monitored as a function of sputtering time, and were calibrated using a standard to provide the concentration of dopants as a function of depth.

2.3 Results and Discussion

2.3.1 Heating Curve

Figure 2.1 illustrates typical heating curves (anneal temperature as a function of time in the range of 200-1000 ℃) for these experiments. When the microwave power is turned off, the temperature drops rapidly. The anneal time is defined as the time interval between the power-on event and the power-off event. The maximum anneal times for the B^+ implanted and P^+ implanted samples in our study are 400 s and 240 s, respectively. The temperature of the B^+ implanted and P^+ implanted samples reached the highest value at ~160 s and began to decrease slowly after ~ 230 s. The highest temperature reached for both B^+ and P^+ implanted samples, with the various implant doses, was ~ 740 ℃. This indicates that for the experimental conditions used in this study, dopant species and dose have little influence on the maximum MWA temperature, when the annealing is performed with the assistance of a susceptor.

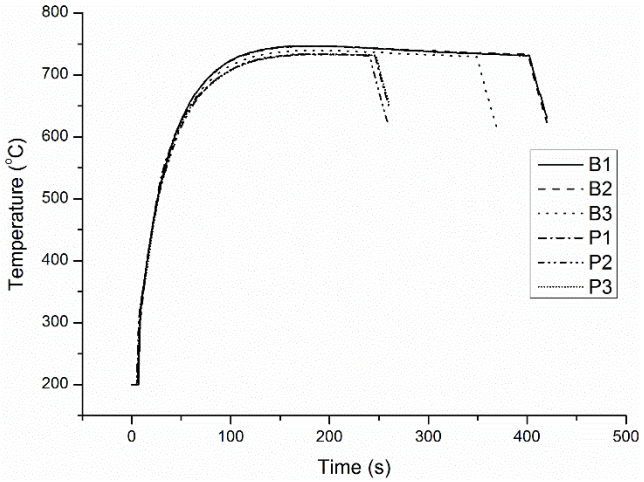

Figure 2.1 Temperature as a function of time measured by a pyrometer with a 200-1000 ˚C range for B^+ and P^+ implanted Si samples: 2×10^{15} B^+ cm^{-2} (B1), 3×10^{15} B^+ cm^{-2} (B2), 4×10^{15} B^+ cm^{-2} (B3), 2×10^{15} P^+ cm^{-2} (P1), 3×10^{15} P^+ cm^{-2} (P2), 4×10^{15} P^+ cm^{-2} (P3)

2.3.2 Dopant Activation and Recrystallization in MWA for P^+ Implanted Si and B^+ Implanted Si

During MWA, dopants move to substitutional positions and become electrically activated and this results in decreased R_{sh}. The drop in R_{sh} depends on the extent of dopant activation. The R_{sh} of the as-implanted samples is too high to be measurable via the four-point-probe set-up used in this study. The sheet resistances of P^+ implanted samples as a function of anneal time, in Figure 2.2, drop sharply within 40 s and then remain constant. However, the R_{sh} values of B^+ implanted samples, in Figure 2.2, decrease gradually and saturate at higher values (than the corresponding P^+ values) within 200 s of annealing.

Hall measurement results are tabulated in Table 2.1. The fraction of dopants activated is calculated by taking the ratio of sheet concentration (cm^{-2}) to the dose (ϕ). The average fraction is ~ 16% for B^+ implanted Si, much lower than the corresponding

value for P^+ implanted Si, in agreement with the R_{sh} measurements. In other words, the P^+ implanted samples show more efficient electrical activation than the B^+ implanted samples do.

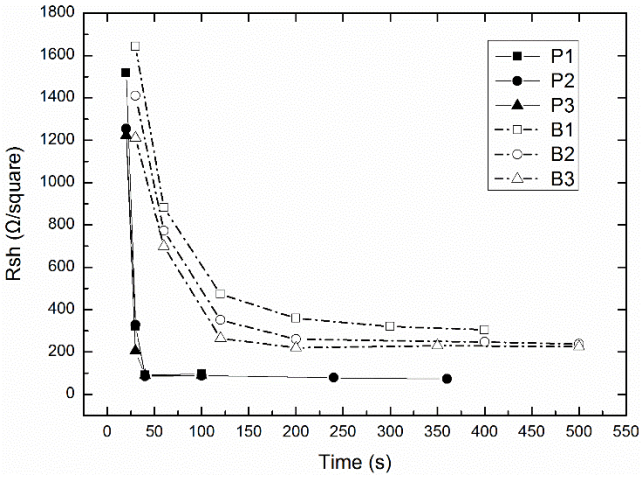

Figure 2.2 R_{sh} as a function of time for 2×10^{15} P^+ cm^{-2} implanted Si (solid square), 3×10^{15} P^+ cm^{-2} implanted Si (solid circle), 4×10^{15} P^+ cm^{-2} implanted Si (solid triangle), 2×10^{15} B^+ cm^{-2} implanted Si (open square), 3×10^{15} B^+ cm^{-2} implanted Si (open circle), 4×10^{15} B^+ cm^{-2} implanted Si (open triangle).

The regrowth rate of the amorphous layer during solid phase epitaxial growth significantly affects the efficiency of electrical activation [99]. After the initial 30 s anneal, the R_{sh} of P^+ implanted Si is lower than that of the B^+ implanted Si. The relatively high effective carrier concentration in P^+ implanted silicon enables its amorphous layer to regrow faster [99]. The regrowth rate and the electrical activity of the layer near the amorphous-crystalline interface are closely interrelated [99]. The faster regrowth rate in P^+ implanted silicon in turn enhances the electrical activity. This positive feedback enables the recrystallization and electrical activation to occur in a much shorter time, 40 s for the P^+ implanted Si, compared to the B^+ implanted Si.

Table 2.1 Hall measurement results and activation calculations for 40 s microwave annealed 2×10^{15} P^+ cm^{-2} and 4×10^{15} P^+ cm^{-2} implanted Si, 400 s microwave annealed 2×10^{15} B^+ cm^{-2} implanted Si and 350 s microwave annealed 4×10^{15} B^+ cm^{-2} implanted Si. The sheet thickness is approximated by $2R_p$ to obtain the sheet concentration.

Sample	Resistivity (Ωcm)	Carrier type	Sheet concentration (cm^{-2})	Bulk concentration (cm^{-3})	Mobility (cm^2/V-sec)	Activated Fraction (%)
2×10^{15} P^+ cm^{-2} front	95.063	N	1.28×10^{15}	2.72×10^{20}	51.3	64
4×10^{15} P^+ cm^{-2} front	83.071	N	1.63×10^{15}	3.47×10^{20}	46.1	41
4×10^{15} B^+ cm^{-2} front	219.66	P	5.97×10^{14}	5.10×10^{19}	47.2	15
2×10^{15} B^+ cm^{-2} front	313.623	p	3.58×10^{14}	3.05×10^{19}	55.6	18

Figure 2.3 displays Raman spectra obtained from as-implanted and annealed samples. In the Raman spectra from the P^+ implanted samples, shown in Figure 2.4(a), the as-implanted and 20 s annealed samples each have a broad peak at 470-480 cm^{-1}. This peak results from the amorphous Si layer that is created by ion implantation [10]. The sharp Raman peak at 520 cm^{-1}, from the as-implanted sample, is from crystalline Si in the substrate [21]. The sharp crystalline Si peak at 520 cm^{-1} from the 20 s annealed sample is attributed to both Si substrate and partially crystallized Si near-surface layers. The incident Raman laser beam penetrates beyond the amorphous layer and into the crystalline Si (c-Si) substrate and this results in the Si substrate contributing to the Si Raman line [21]. After a 40 s anneal, the broad amorphous Si (a-Si) peak disappears and the magnitude of the 520 cm^{-1} crystalline Si peak increases. This indicates that more crystalline Si has formed in the 40 s sample when compared to the 20 s annealed sample. Even with a 100 s anneal, the magnitude of the crystalline Si peak does not increase

further, which suggests that the damaged Si lattice has been almost completely repaired after 40s. It should be noted that the crystalline Si peaks in these samples originate from both the c-Si substrate and the recrystallized Si near the surface.

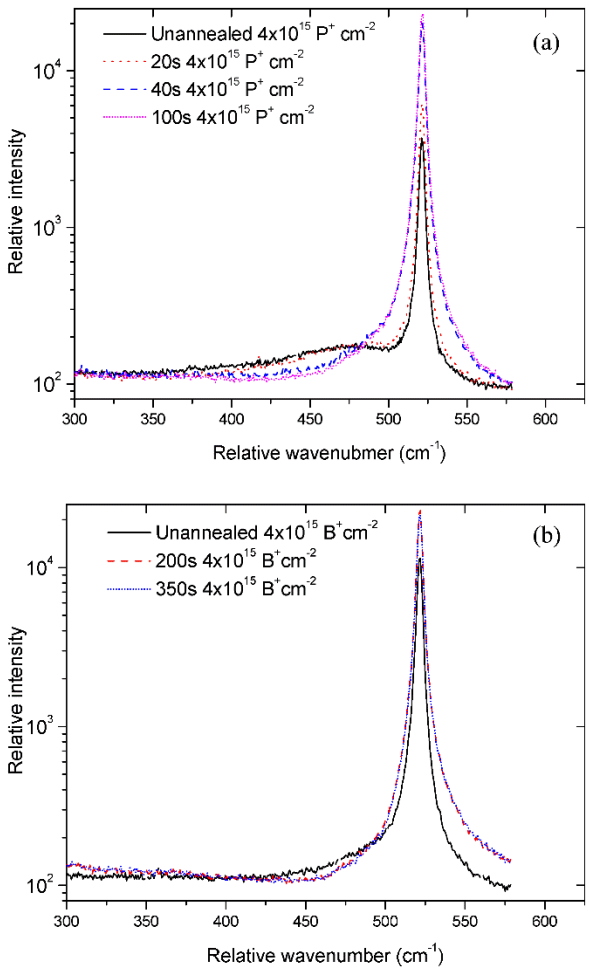

Figure 2.3 Raman spectra from ion-implanted Si: (a) 4×10^{15} P^+ cm^{-2} with different anneal times; (b) 4×10^{15} B^+ cm^{-2} with different anneal times.

In the Raman spectra from the B^+ implanted samples, shown in Figure. 2.3(b), the 520 cm^{-1} single-crystal Si peaks from the 200 s and 350 s annealed samples overlap, indicating that recrystallization of the amorphous Si layer is complete after 200 s. The broad amorphous Si peak in the B^+ as-implanted sample is barely distinguishable.

Furthermore, the single-crystal Si peak in the B^+ as-implanted sample is very strong and is comparable to the corresponding peak of the annealed samples. This result indicates that the amount of damage in the B^+ as-implanted sample is smaller than in the case of the P^+ implanted sample. Since the implantation energy of the boron falls into an energy range where electronic energy losses are greater than nuclear energy losses, the boron ions primarily experience electronic energy losses which cause lower amounts of damage in the Si [5].

Figure 2.4(a) shows RBS spectra from 4×10^{15} P^+ cm^{-2} implanted Si in random and [001] channeling directions. In general, lower backscattering yield in the spectra is indicative of better crystalline quality of the samples. The backscattering yields in the channeling direction for P^+ implanted samples after 40 s and 100 s annealing are similar and are much lower than the yield from the as-implanted sample. These results indicate that the repair of the damaged layer in ion implanted Si is complete after 40 s MWA. This finding is consistent with the Raman results.

Similarly, in the case of the 2×10^{15} B^+ cm^{-2} implanted Si in Figure. 2.4(b), the reduced backscattering yield in the MWA sample indicates that the damaged layer in the B^+ implanted Si is repaired after 200 s. A second peak is observed at a location immediately after the outermost surface peak, and is still present even after annealing. This suggests that there are extended defects beneath the Si surface. Such defects cause dechanneling and results in a second peak in the ion channeling spectra of the B^+ as-implanted sample. Upon annealing, the damaged layer is recrystallized, but extended defects such as dislocation loops are not removed. This results in the observed reduced

backscattering yield and the second peak remaining in the ion channeling spectrum from the microwave annealed sample.

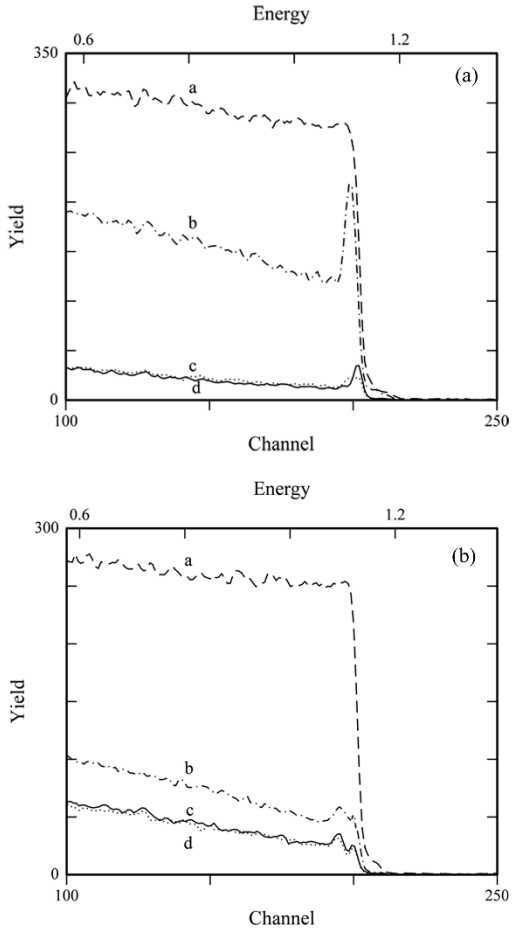

Figure 2.4 RBS spectra from ion-implanted Si samples: (a) ion channeling from 4×10^{15} P^+ cm^{-2} implanted Si: as-implanted in a random direction (dashed line), as-implanted in a [001] direction (dash-dotted line), annealed for 40 s in [001] direction (solid line), annealed for 100 s in [001] direction (dotted line). (b) ion channeling from 2×10^{15} B^+ cm^{-2} implanted Si: as-implanted in random direction (dashed line), as-implanted in [001] direction (dash-dotted line), annealed for 200 s in [001] direction (solid line), annealed for 400 s in [001] direction (dotted line).

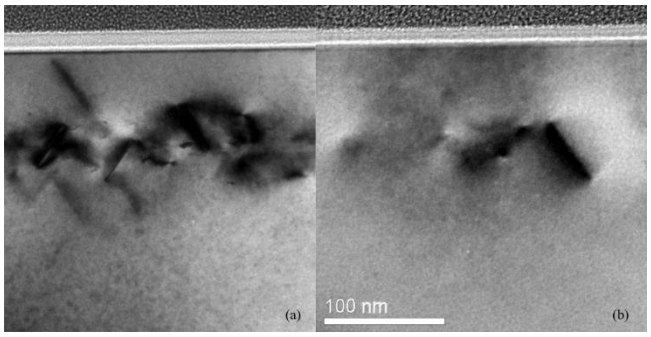

Figure 2.5 TEM micrographs from 2×10^{15} B^+ cm^{-2} implanted Si: (a) 200 s microwave annealed; (b) 400 s microwave annealed.

Transmission electron microscopy (TEM) analysis was performed to check for defects beneath the surface of the B^+ implanted Si. The TEM micrographs in Figure. 2.5(a) and (b) show a presence of extended defects in the 200 s and 400 s MWA 2×10^{15} B^+ sample. These defects lead to the second damage peak observed in the case of the annealed samples. With the 200 s anneal, boron interstitial clusters (BICs) and extended defects are formed as shown in Figure. 2.5(a) [94]. After an additional 200 s anneal at the same temperature, 747 ℃, the small extended defects and BICs dissolve by emitting Si interstitials. The emitted Si interstitials are transported to larger extended defects resulting in Ostwald ripening of the defects [100]. This mechanism then causes an increase in size and a decrease in areal density of the extended defects as seen in Figure. 2.5(b) compared with Figure. 2.5(a) [100].

2.3.3 Dopant Activation and Recrystallization in MWA vs. RTA for As^+ Implanted Si

For comparison of dopant activation, MWA and RTA were performed on As^+ implanted Si using similar heating curves/thermal budgets. Annealing was conducted for 50 seconds and 100 seconds, and the heating curves of both durations were intentionally kept almost the same for MWA and RTA. Heating curves for 50 seconds annealing is

shown Figure. 2.6. The ramp rate, the peak temperature of RTA and MWA were kept almost the same, which mean the total energy input to the sample are almost the same in those two process. The resulting sheet resistances are shown in Table 2.2. It turned out that sheet resistances of P^+ implanted Si samples after 50 sec RTA was significantly high and even out of the measurable range of the four point probe. In contrast, 50 sec MWA enables significantly drop of sheet resistance.

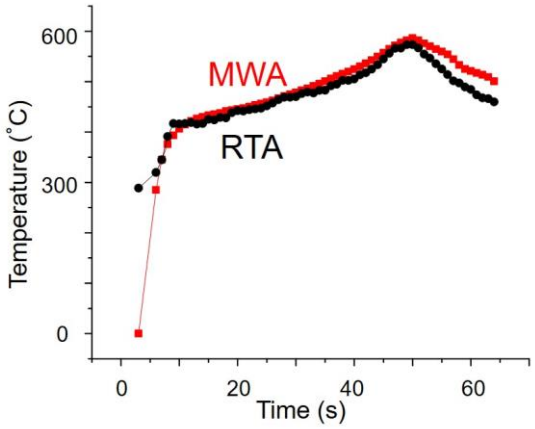

Figure 2.6 The heating curve of MWA and RTA for 50 sec duration.

After 100 sec annealing, dopant activation was achieved in RTA sample, but its sheet resistance is almost the same as the sheet resistance of 50 sec MWA sample, which is higher than the sheet resistance of 100 sec MWA sample. The sheet resistance of As+ implanted Si annealed by MWA for different duration is shown in Figure 2.7. It indicates that a sufficient dopant activation is achieved within 50 sec, which is more efficient than RTA.

Table 2.2 The sheet resistance for 2×10^{15} cm^{-2} As^{+} implanted Si annealed by MWA and RTA using the similar thermal budget for 50 sec and 100 sec.

Annealing condition	R_{sh} (Ω/square)
RTA 50s	N/A
MWA 50s	93
RTA 100s	90
MWA 100s	80

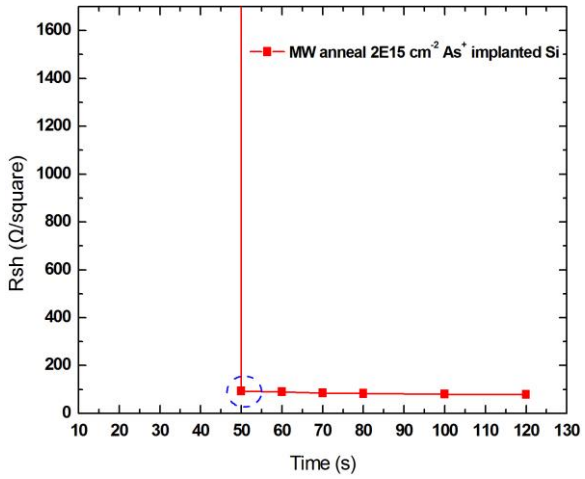

Figure 2.7 R_{sh} as a function of time for 2×10^{15} As^{+} cm^{-2} implanted Si annealed for different duration.

MWA and RTA are conducted using the similar heating curve as shown in Figure 2.6. The recrystallization during MWA and RTA are compared by inspecting the RBS ion channeling spectrum as shown in Figure 2.8. As ion channeling yield on the surface for as-implanted Si is as high as the yield in random direction, which indicates the formation of amorphous Si on the surface. After 50 sec RTA, there is still a relatively thick amorphous layer on the sample surface. Only a small amount of amorphous layer is recrystallized after 50 sec RTA since the width of amorphous Si signal is only reduced a little in comparison with as-implanted Si. However, the amorphous layer is completely recrystallized after 50 sec MWA since the yield of backscattered ions is significantly

reduced and no amorphous Si signal is observed. This result is consistent with the dopant activation that discussed in last section. After 100s, the ion channeling spectra of RTA and MWA are the same, indicating the same extent of dopant activation.

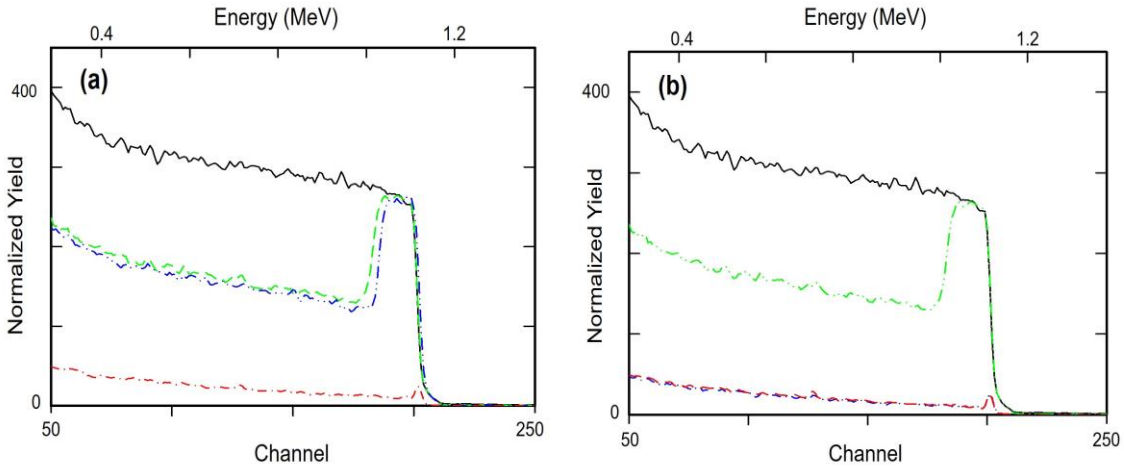

Figure 2.8 RBS spectra from 2×10^{15} As^{+} cm^{-2} implanted Si samples before and after annealing (a) 50 sec RTA and MWA and (b) 100 sec RTA and MWA. As-implanted Si in a random direction (black solid line), as-implanted Si in a [001] direction (green dashed line), RTA Si in [001] direction (blue dash-double dotted line), MWA Si [001] direction (red dash-dotted line)

A mechanism [101-103] that involves ion hopping caused by microwave field is proposed to be the source for the enhanced dopant activation resulting from MWA annealing. Ion hopping, which is known to be operational in ac conductivity of ionic glasses and disordered crystalline materials, can occur by two different processes: a translational process and a localized process[101-103].

The two ion-hopping processes are mathematically described by fitting the measured ac conductivity of ionic glasses as a function of frequency. The relationship between conductivity and frequency is shown as [101, 102]:

(2.1)

where σ_{dc} is DC conductivity, v is frequency, A and B are pre-factors, and p and q are exponents. Translational hopping is operative when the exponent p is found to be smaller than 1. A value of q between 1 and 2 corresponds to localized hopping [101, 102].

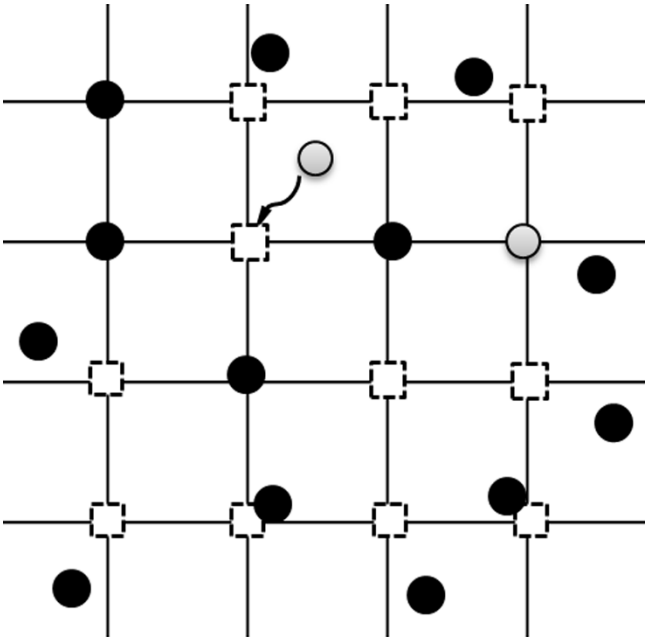

Figure 2.9 Schematic of the localized ion hopping process in disordered materials. (bulk material's atoms: solid circles; ions: open circles; vacancies: open squares)

The localized ion hopping process, as shown in Figure 2.9, is active at radio and microwave frequencies and can be applied to our case. The localized process occurs via small short-range hops and is enhanced by lattice disorder in the material [101, 102]. The disorder provides energetically favorable neighboring sites that are available for ion hopping [101, 102]. Since those positions are energetically favorable, once an ion hops into such a position it will tend to not leave that position [101, 102]. If this energetically favorable position is a neighboring vacancy site, then when an implanted dopant atom hops into that vacancy site and stays there, the dopant atom becomes a substitutional dopant atom, which is now electrically active. Hence, enhancement of such localized ion-hopping by

the oscillating microwave field, could be responsible for the enhanced dopant activation observed in the case of MWA.

When the thermal budgets for RTA and MWA are intentionally matched, the resulting thermal energy of the dopant atoms is the same during both MWA and RTA. However in the presence of a MW field, the ions experience an additional oscillating electric force that arises from interaction of the ionic charge with the electric field component of the microwave. This provides an additional force that causes the ions to move back and forth [14], and increases the likelihood of localized short-range hopping [101, 102]. In other words, dopants gain additional kinetic energy in the presence of a microwave field, and are therefore more likely to hop to nearby energetically favorable sites, such as adjacent vacancies, and thereby become substitutional atoms. This mechanism would explain enhanced activation of dopants during MWA in comparison with RTA.

2.3.4 Dopant Diffusion in MWA vs. RTA for P^+ Implanted Si and B^+ Implanted Si

The diffusion of B^+ and P^+ dopants before and annealing MWA and RTA are compared. The annealing conditions and resulting sheet resistance are shown in Table 2.3. Figure 2.10(a) shows SIMS profiles from 4×10^{15} B^+ implanted Si before and after annealing. Immobile boron peaks and extended diffusion in the tail region are evident in SIMS profiles of the MWA samples. Such phenomena are a common occurrence in boron implanted silicon that has been annealed, and is typical of transient enhanced diffusion (TED) [94-96]. The extended tail region is due to TED, in the course of which, Si self-interstitials kick-out substitutional boron atoms resulting in mobile boron interstitials, or alternatively, in the formation of mobile Si-B pairs that can diffuse rapidly through the Si

substrate [94, 96, 100]. The immobile peaks are associated with extended defects which trap the boron dopants, and with the formation of BICs that are immobile and which impede dopant activation [104]. In our case, the average boron dopant activation is only 16%. The presence of extended defects in TEM micrographs of the 200 s annealed 2×10^{15} B^+ implanted Si (Fig. 2.5(b)) is consistent with this explanation above.

Table 2.3 The thermal budgets for MWA and RTA for P^+ implanted Si wafers and B^+ implanted Si wafers, and the corresponding sheet resistances.

Thermal Budget No.	Dopant species	Annealing condition	Total time (s)	Ramp time (s)	Peak Temperature (^{o}C)	Dwell time (s)	R_{sh} (Ω/sq)
1	2×10^{15} cm^{-2} P^+	RTA 710^{o}C	74	34	710	40	93
2	2×10^{15} cm^{-2} P^+	Microwave 40s	40	40	584	0	91
3	4×10^{15} cm^{-2} B^+	RTA 738 ^{o}C	96	36	738	60	340
4	4×10^{15} cm^{-2} B^+	Microwave 200s	200	140	738	60	251

Boron profiles from the 200 s MWA samples are essentially the same as the boron profile from the 350 s MWA sample in Fig. 2.10(a). This suggests that no further diffusion occurs after 200 s of MWA. This absence of further diffusion is due to the strong dependence of TED on the supersaturation of free Si interstitials [94, 96]. Depending on processing conditions, the average local Si interstitial concentration (C_{int}) can exceed the equilibrium interstitial concentration (C_{eq}). In such a case, the supersaturation (S) can be defined as $S = C_{\text{int}} / C_{eq}$ [94]. The enhanced diffusivity of boron ($D_{B,TED}$) is proportional to the supersaturation, and can be be expressed as follows [94]:

$$D_{B,TED} = D_{B,eq} S = D_{B,eq} \frac{C_{\text{int}}}{C_{eq}} \tag{2.2}$$

where $D_{B,eq}$ is boron's diffusivity under equilibrium conditions. During the initial stages of annealing, the supersaturation S is large and therefore TED proceeds quickly. Meanwhile, small interstitial clusters form and then grow by consumption of free Si self-interstitials [94]. This results in the decay of the supersaturation of free Si interstitials and a gradually decreasing rate of TED [94].

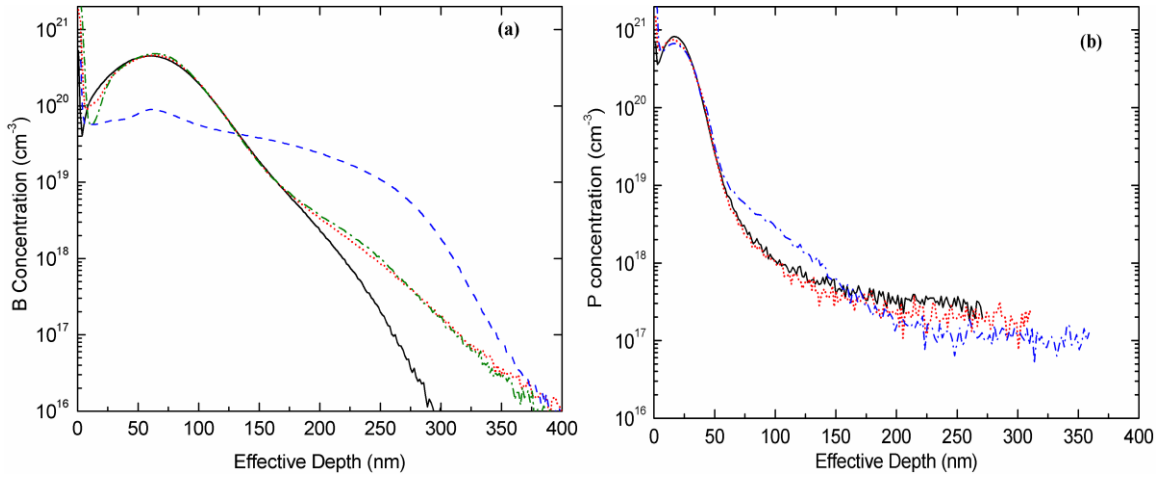

Figure 2.10 SIMS profile from ion implanted Si: (a) 4×10^{15} B^+ cm-2 implanted Si before annealing (solid line), after microwave annealing for 200 s (dotted line) and 350 s (dash dotted line) after RTA at 950 oC for 90 s (dashed line); (b) 2×10^{15} P^+ cm^{-2} implanted Si prior to annealing (solid line), after microwave annealing for 40 s (dotted line), after RTA at 710 ℃ for 40 s (dashed line).

In the later stages, Ostwald ripening[94] occurs and small extended defects emit Si atoms and finally disappear. Large extended defects grow in size by the consumption of Si atoms that are emitted from small-extended defects. Compared to the early stages, the supersaturation of Si interstitials at this later stage is much lower [94], and therefore there is

almost no enhancement of boron's diffusivity; and hence, TED essentially stops. Due to these reasons, no diffusion happens after the 200 s of anneal.

For the boron profile of the RTA sample (950 ^{o}C for 90 s) in Fig. 2.10(a), the significant boron diffusion observed in the profile is likely due to a large amount of Si interstitials and boron dopants which are released during dissolution of the extended defects in the sample [3, 94, 95, 104]. The high temperature of the RTA anneal can remove most dislocations and BICs [3, 5, 94, 104] and this results in a temporary supersaturation of free Si interstitials and boron atoms. It is this temporary supersaturation that gives raise to the enhanced local diffusion [94, 104]. Moreover, the diffusivity $D_{B,eq}$ also depends on temperature, as shown in following equation:

$$D_{B,eq} = D_0 \exp(-\frac{E_A}{kT}) \tag{2.3}$$

where D_0 is the pre-exponential parameter, E_A is the activation energy, k is Boltzmann's constant, and T is the temperature. Hence, the increased boron diffusion in RTA is also attributable to its high anneal temperature. In contrast, the reduced TED in microwave annealing is due to boron's low diffusivity at reduced anneal temperature, combined with a reduction in the removal of extended defects [105, 106].

The extent of dopant diffusion in P^+ implanted Si, with almost the same resulting sheet resistances after RTA and MWA, was compared in Fig. 2.10(b). The samples were annealed using RTA and MWA under thermal budgets 1 and 2 as shown in Table 2.1. The two techniques achieved almost the same sheet resistance, indicating equivalent dopant activation in both cases. SIMS profiles obtained from these P^+ implanted Si

samples are shown in Fig. 2.10(b). No measurable phosphorous diffusion occurred in the 40 s MWA sample, whereas significant phosphorus diffusion was observed after RTA. MWA (performed at lower temperatures and for shorter time durations) can achieve the same level of dopant activation in P^+ implanted Si as RTA (that is performed at higher temperature and for longer time durations). The reduced temperature and time of the MWA successfully minimizes the extent of dopant diffusion.

2.4 Conclusions

This work investigated the electrical and structural properties of B^+ implanted, P^+ implanted and As^+ implanted Si samples before and after MWA. The results of this study show that MWA is able to cause effective dopant activation and recrystallization of ion implanted Si. Due to ion hopping that occurs during MWA, the ion implanted Si samples experience more effective dopant activation after MWA than that achieved by a comparable thermal budget of RTA. This enables better dopant activation at equivalent thermal budget for MWA and RTA. The reduced temperature used in MWA enables the reduction of TED of boron dopants, but does not facilitate the complete removal of extended defects. P^+ implanted samples on the other hand, experience higher electrical activation than B^+ implanted samples, after annealing. Moreover, MWA of P^+ implanted samples lead to no measureable dopant diffusion, and result in equivalent phosphorus dopant activation at lower temperatures and in a shorter time, compared to RTA. For the conditions investigated in this work, the extent of microwave absorption in susceptor-assisted microwave heating depends on the bulk substrate material being heated, rather than the implanted dopant species or dose.

3. CHARACTERIZATION OF AS^+ IMPLANTED SI ANNEALED BY SCANNING LASER AND MICROWAVE

3.1 Introduction

The most widely used annealing method is rapid thermal annealing (RTA) [3, 10]. Some alternatives of RTA are merging, such as laser annealing and microwave annealing. We have showed that microwave annealing benefit from it low processing temperature and diffusion-less dopant profile in Chapter 2. Laser annealing benefit from its fast and epitaxial regrowth due to the presence of liquid phase during the annealing[23]. As a results, the comparison between microwave and laser annealing are proposed. The dopants activation, recrystallization and dopant diffusion obtained by the two process techniques will be compared and investigated.

Metal-oxide-semiconductor field-effect transistors (MOSFETs) are indispensable as electronic devices. During the fabrication of MOSFETs, dopants including As^+, B^+ and P^+ are incorporated into Si wafers to alter the resistivity of the wafer surface and to define active regions of devices.[3, 22, 107] Dopants are incorporated by diffusion or ion implantation, with ion implantation being the more common method. Ion implantation is performed by accelerating ionized dopants to energies of 30 – 100 keV, and then implanting them into the wafer.[4] During the implantation, these high energy ions bombard the atoms on the wafer lattice and disorder those atoms that are near the wafer surface.[4] As a result, lots of vacancies and interstitials are created, and an amorphous layer is formed in the vicinity of the wafer surface.[4] To recrystallize the amorphous layer, and to incorporate the dopant atoms into substitutional sites of the lattice, the wafer needs to be annealed at an elevated temperature.

The most commonly used annealing method is rapid thermal annealing (RTA). Some alternatives to RTA are emerging, such as laser annealing and microwave annealing[28, 108-110]. With RTA, the entire silicon wafer is heated to the annealing temperature[10, 21]. This can cause excessive dopant diffusion. In contrast, due to silicon's high optical absorptivity in the visible and near-IR regimes, laser annealing can target just the amorphous region[111]. This minimizes the thermal budget needed for the annealing process. In addition, laser annealing can provide a higher degree of dopant activation than RTA, by overcoming the solid solubility limits for the dopant ions[23]. Microwave (MW) annealing also reduces the thermal budget with respect to RTA because dopant activation can be accomplished at a lower annealing temperature[112]. However microwave annealing is still limited by the solid solubility limits for the dopant ions.

In this study, As^+ implanted Si wafers are annealed by susceptor-assisted microwave and laser annealing. The dopant activation is estimated by measuring the sheet resistance of annealed samples via four-point probe analysis. The extents of recrystallization of the amorphous layers during MW and laser annealing are assessed by ion channeling and Rutherford Backscattering Spectrometry (RBS). The dopant distributions before and after annealing are studied by Secondary Ion Mass Spectrometry (SIMS). Laser annealing shows advantages for dopant activation. The two techniques show the same performance with respect to re-crystallization. The dopant depth profiles achieved by MW annealing and laser annealing have different characteristics that make them suitable for different applications. Laser annealing appears to be beneficial for annealing n-wells and p-wells for complementary metal-oxide semiconductor (CMOS)

devices. Susceptor-assisted MW annealing is good for annealing source and drain regions in MOSFETs.

3.2 Experimental

Arsenic ions were implanted into (001) orientated Si wafers that are p-type boron doped. The implantation was performed with an energy of 180 keV and doses of 1×10^{15} cm^{-2} and 4×10^{15} cm^{-2}. To minimize ion channeling during implantation, the wafers were titled at 7 ° off the incident beam.

Microwave (MW) annealing of the As^{+} implanted Si was conducted in a 2.8×10^{4} cm^{3} cavity MW oven with a 1200 W magnetron source, and using a single frequency of 2.45 GHz. Implanted Si samples were mounted on a SiC susceptor. SiC can efficiently convert the MW energy into heat, and rise to a relatively high temperature, due to its high dielectric loss and strong absorption efficiency for MWs.[21] As a result, the ion-implanted silicon samples on the susceptor were heated by conductive heating from the susceptor[21, 97]. Raytek Compact MID series pyrometers (measurable range of 200-1000 ^{o}C) were used to monitor the in-situ sample surface temperature as a function of time. The anneal time varied from 20 s to 100s, and the corresponding temperature ranged from 449 ^{o}C to 815 ^{o}C.

The laser annealing was performed on a Universal Laser Systems PLS6MW with a 1.06 μm wavelength fiber laser. The fiber laser had an average output power of 40 Watts. For the laser annealing experiments, the laser power was modulated from 65% (26 Watts) to 85% (34 Watts). The laser beam was focused to a circular spot with a size

of 25 μm. The beam was rastered across the ion implanted silicon sample at a speed of 30 cm/s, and at a frequency of 500 kHz.

The extent of dopant activation was estimated by measuring the sheet resistance (R_{sh}) of each sample. The measurements were conducted using a four-point probe system equipped with a 100 mA Keithley 2700 digital multimeter.

The presence of implantation damage in as-implanted Si and the extent of recrystallization in annealed As^+ implanted Si samples were studied by ion channeling based on RBS. Since the As^+ implanted samples are prepared from (001) oriented Si wafers, a 2 MeV He^+ ion beam was aligned along the sample's [001] channeling direction. A channeling spectrum was then obtained by tilting the sample to 5^o from the normal and rotating the sample in the azimuth until the yield reached a minimum.

Diffusion of dopants was investigated by comparing depth profiles of arsenic ions before and after the samples were MW or laser annealed. The depth profiles were obtained by SIMS. The primary ion used for SIMS was Cs^+, and secondary 30 Si^+ and 75 As^+ ion signals were alternatively collected as a function of sputtering time. The depth was calibrated by measuring the crater depth, and the concentration was calibrated by equating the area under the profile to the dose of arsenic ions. Using this method, the ion signal as a function of time was converted to an As^+ concentration as a function of depth. The depth values were corroborated using RBS analysis.

3.3 Results and Discussion

The output power was varied for the laser anneals, while the annealing time was varied for the MW anneals. For a side by side comparison, the absorbed energy density

was calculated for both laser and MW annealing. The resulting sheet resistances of laser annealed and MW annealed samples are compared as a function of absorbed energy density, in Figure. 3.1. The results show that the laser annealing achieves a similar or even lower sheet resistance while using only ~$^1/_7$ of the energy density that is required for the MW annealing. With laser annealing, the sheet resistance of the annealed sample drops abruptly as the energy density is increased. In contrast, once the energy density in the MW annealing is above a threshold, the sheet resistance of the MW annealed samples begins to drop dramatically to a certain level, and then decreases slowly as the energy density increases. Based on the above comparison, laser annealing shows great advantage over MW annealing for dopant activation, since it enables higher levels of dopant activation at a lower energy density.

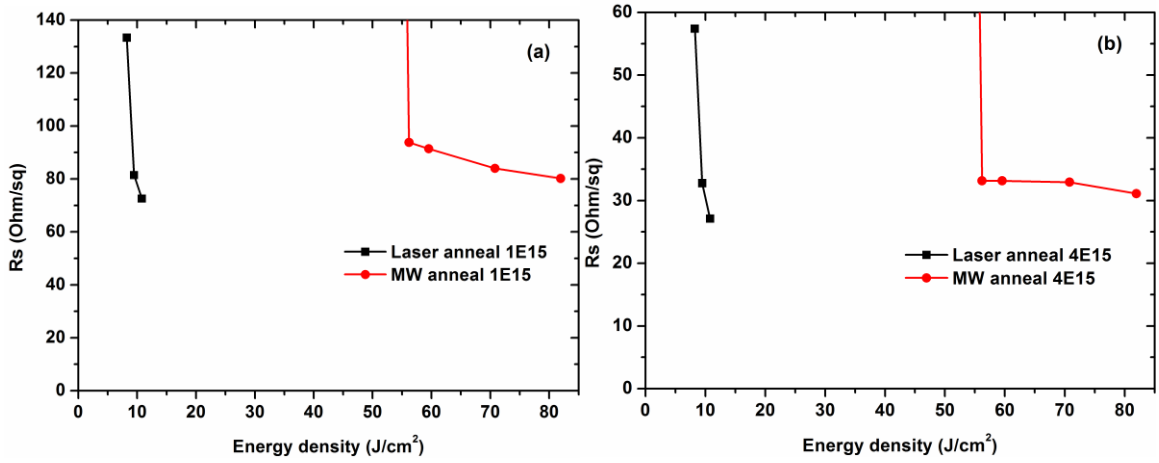

Figure 3.1 The sheet resistance of As^+ implanted Si after laser annealing with various powers and MW annealing with various times (a) 1×10^{15} As^+ cm^{-2} implanted Si, (b) 4×10^{15} As^+ cm^{-2} implanted Si.

The high extent of dopant activation, achieved at a lower energy density in laser annealing, is due to surface heating during laser annealing. The amorphous Si has a larger absorption coefficient α (10^4 cm^{-1}) at a wavelength of 1.06 μm (laser wavelength used in

this study).[23] As a result, most of the laser energy is absorbed in the thin amorphous layer as opposed to the crystalline substrate. This causes the Si surface to melt. According to SRIM simulation, the thickness of the amorphous layer is about 0.24 μm ($2R_p$) [14]. Once the laser beam penetrates down to the crystalline Si substrate, the energy density is diluted due to the relative small absorption coefficient α (50 cm^{-1}) of crystalline Si. The energy absorbed per unit volume (in Joules per cubic centimeter) as a function of sample depth (z) during laser annealing can be calculated by [23]:

$$\Phi(z) = I_0[(1-R)/d]e^{-z/d} \tag{3.1}$$

where the I_0 is the output /incident energy density of the laser (in Joules per square centimeter), R is the reflectance of Si at the laser wavelength (1.06 μm) and d is the absorption depth, which is the reciprocal of the absorption coefficient α. According to the above equation, the absorption depth d could be calculated from the reciprocal of the absorption coefficient, as 1 μm and 200 μm for amorphous silicon and crystalline silicon, respectively.[23] Note that the absorption depth here denotes a penetration depth at which the magnitude of the laser beam has decayed to *1/e* of its surface value. Compared to the absorption depth, the 0.24 μm thickness of the amorphous silicon layer is relative small. Therefore, a Φ(z) plot with a near-linear shape was observed rather than an exponential function. This calculated result for the absorbed energy density per unit volume across the sample depth z during laser annealing is shown as the solid black curve in Figure. 3.2. The energy absorbed per volume by the amorphous layer is almost three orders of magnitude greater than that absorbed by the crystalline layer.

MW annealing results in volumetric heating [14]. Instead of being mainly absorbed by the amorphous layer, the energy will be absorbed uniformly across the entire Si

sample. Therefore, the energy absorbed per unit volume becomes lower (compared to laser annealing) because it is uniformly distributed across the 625 μm thick Si sample. Figure 2 compares the energy absorbed per unit volume as a function of sample depth for laser annealing and MW annealing. The energy distributions across the sample during laser annealing and MW annealing are quite different. Due to the different energy distributions, laser annealing causes liquid phase growth,[23, 25] while MW annealing provides solid phase regrowth[10]. These different regrowth processes result in different dopant activation processes. As a consequence, the laser annealing is more efficient in terms of dopant activation.

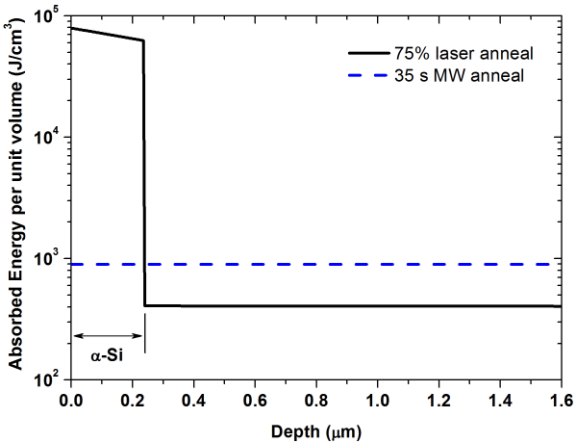

Figure 3.2 The calculated absorbed energy per unit volume during laser annealing and MW annealing

The annealing process involves not only dopant activation but also the recrystallization of the amorphous layer at the surface. Ion channeling can be used to determine the levels of recrystallization that result from the MW and laser annealing processes.[113] The crystalline material typically results in a low yield of backscattering ions during ion channeling. However, the amorphous material has a high yield of backscattering ions because of the disordered atoms in the layer.[113] Moreover, defects in

the material cause dechanneling of the incident ions, and this then leads to an increased yield of backscattering ions.[113] Figure 3.3 compares the [001] ion channeling spectra of As^+ implanted Si before and after laser annealing.

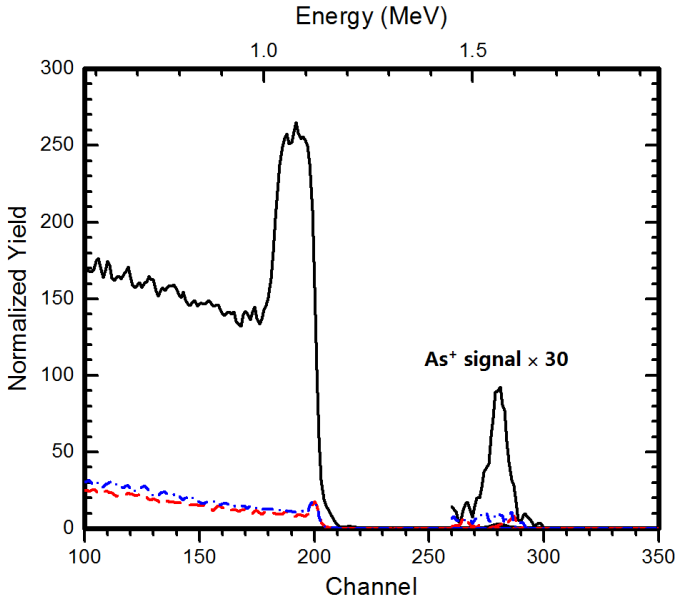

Figure 3.3 RBS ion channeling spectra in the [001] direction from 1×10^{15} As^+ cm^{-2} implanted Si samples: as-implanted sample (black solid line), 75% power laser annealed sample (blue dashed-dotted line), and 85% power laser annealed sample (red dashed line).

In Figure 3.3, the dramatic decrease of the backscattering ion yield after annealing indicates that the amorphous layers are recrystallized during laser annealing. The As^+ peak also drops after laser annealing. This is because the majority of the As^+ ions move from interstitial positions to substitutional positions in the lattice, after annealing. As a result, the probability of the incident ions being backscattered from interstitial As^+ ions is reduced, leading to a reduced yield of backscattering ions for the annealed samples. A slightly higher backscattering ion yield is seen, in the low energy region, for the 75% power laser annealed sample. This might be due to the presence of interstitial point

defects in the sample.[113] Such interstitial point defects might result from inadequate crystal regrowth, since the 75% power laser yields a lower annealing temperature locally, compared to the 85% power laser. This would result in a correspondingly slower mass transportation. These point defects can cause dechanneling of the channeling ions and thereby increase their chance of being backscattered, leading to an increased ion backscattering yield in the low energy region of the spectrum.[113]

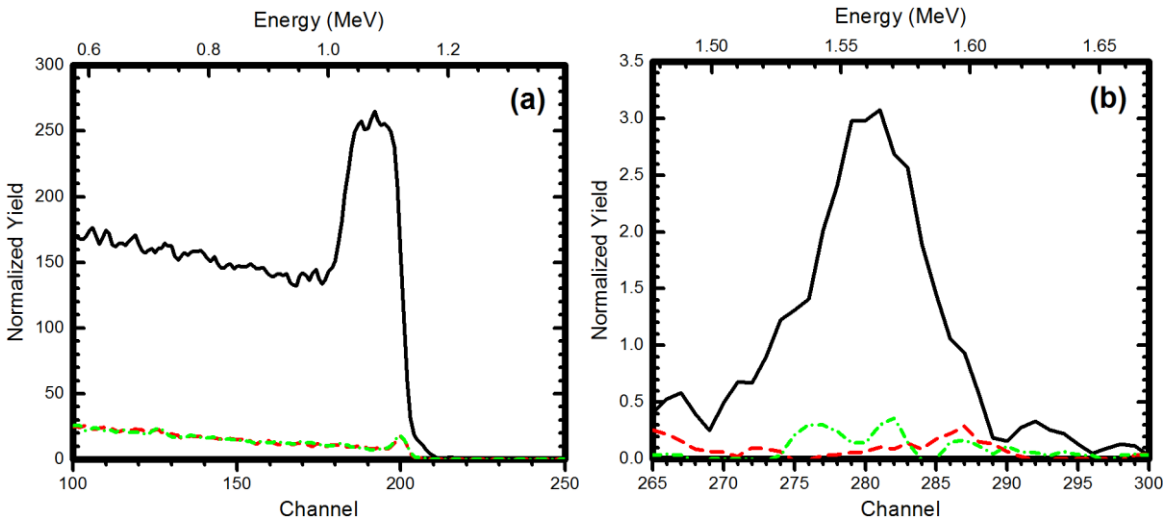

Figure 3.4 The RBS ion channeling spectra in a random and in the [001] direction from 1×10^{15} As^{+} cm^{-2} implanted Si samples. (a) Si signal, (b) magnified arsenic signal: as-implanted sample in the [001] direction (black solid line), 100 sec MW annealed sample in the [001] direction (green dashed-dotted line) and 85% power laser annealed sample in the [001] direction (red dashed line).

Figure 3.4 compares the ion channeling spectra of 100 sec MW annealed and 85% power laser annealed samples. The black line is the backscattering ion yield from an as-implanted sample. After MW and laser annealing, the backscattering ion yield drops. The ion channeling yields immediately after the first surface peak indicate the crystallinity of each sample. In Figure 3.4(a), the yields after the two first surface peaks are the same,

indicating that the same crystallinity is present, regardless of their extent of dopant activation.

Figure 3.4(b) shows the yields of the ions that are backscattered from interstitial As^+. These provide a good estimation of dopant activation. The yield of the As^+ peak from the 85% power laser annealed sample is slightly lower than that of the 100 sec MW annealed sample. This indicates that there is a slightly lower amount of interstitial As^+ ions and a higher extent of dopant activation in the 85% power laser annealed sample. This fact is supported by the lower sheet resistance of the 85% power laser annealed sample in Figure 3.1(a). The 85% power laser annealed sample has a 10% lower sheet resistance than the 100 sec MW annealed sample.

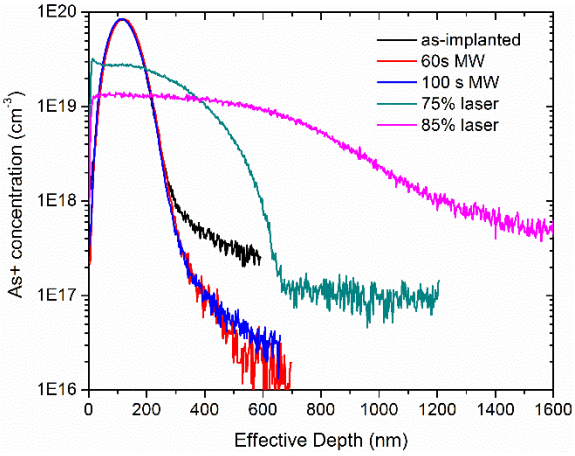

Figure 3.5 SIMS profile from 1×10^{15} As^+ cm^{-2} implanted Si samples before annealing (as-implanted), and after MW annealing (60 sec and 100 sec) and laser annealing (75% and 85% power).

Dopant atoms will typically diffuse under heat treatment. Both the laser and the MW anneals result in heating of the implanted layers. In this study, dopant diffusion is assessed by measuring the depth profiles of As^+ before and after laser and MW annealing via SIMS analysis. Figure 3.5 shows the depth profiles for the as-implanted, laser

annealed, and microwave annealed samples. The profiles show that the laser annealing results in significant dopant diffusion, and that increased power enhances the diffusion. This is due to liquid phase epitaxy in laser annealing.[23] A large portion of the laser energy is absorbed at and near the Si surface as shown in Figure 3.2. This high energy input per unit volume of pulsed laser annealing melts the Si surface layer[23, 25]. After a typical irradiation of 2×10^{-6} sec, the surface recrystallizes quickly at the liquid-solid interface.[23] In the melted layer, the mobility of the dopants is much larger than that in the solid phase. Therefore, dopants are more likely to diffuse and redistribute toward low concentration regions. As a result, the As^{+} concentration in the 75% and 85% power laser annealed samples are quite uniform within 200 nm and 600 nm (from the surface), respectively. The characteristics of such depth profiles are quite suitable for ion implanted n-wells in CMOS technology.

In conventional CMOS processing, n-well and p-well regions are formed by implanting dopants to define the well region first. Then, the ion implanted wafers are annealed in a drive-in furnace to enable diffusion. To control the diffusion depth, and to obtain a uniform distribution of dopants, and to obtain a well depth of 2-3 microns, the thermal cycle is typically 4 to 6 hours at 1000 to 1100 ^{o}C [3]. In contrast, we find that laser annealing can achieve a uniform and deep dopant profile in a much shorter time through liquid phase regrowth. In addition, the diffusion depth that results from laser annealing can be controlled by adjusting the energy output and the wavelength of the laser [111]. However, the energy density distribution in our pulsed laser beam itself is Gaussian. Rastering of the pulsed laser beam across the sample results in slightly non-uniform energy distribution. This in turn results in only 7.5-10% of maximum difference in Rs

across the 1 cm × 1 cm Si sample. As a result, laser annealing appears to be an efficient alternative to drive-in furnace annealing for n-well and p-well formation; however, the control of the energy density uniformity during the laser raster must be improved in order to achieve necessary uniformity required for large-scale manufacturing.

On other hand, there is no measurable dopant diffusion in the As^+ depth profiles of the MW annealed samples. In addition, the MW annealing achieves the same extent of dopant activation as laser annealing does. This absence or minimization of diffusion results from the low temperature and short duration of the MW annealing. The highest temperature that is reached during the 60s and 100s MW annealing is only 706 ^oC and 815 ^oC, respectively. These low temperatures are below the melting point of silicon. This means that solid-phase regrowth occurs during MW annealing. During solid-phase regrowth, dopant atoms are only able to diffuse to nearby atom sites, with the help of lattice distortion and vibration. This minimizes long range diffusion. As a result, MW annealing is a suitable technique for annealing ion implanted source, drain and channel regions (that require minimized dopant diffusion) for MOSFET fabrication.

3.4 Conclusion

Our study shows that laser annealing has advantages for dopant activation when compared to MW annealing. The laser anneal is beneficial for deep well formation with a uniform dopant concentration. The relatively high diffusion depth that is observed for laser annealing can be addressed by choosing a shorter wavelength laser[111]. The shorter wavelength will have a lower penetration depth into the silicon, thereby reducing the

depth of the surface melting[111]. The minimization of diffusion that is achieved by MW annealing provides a marked benefit for shallow junction devices.

4. NUMERICAL PREDICTION OF TRANSMITTANCE SPECTRA FOR TRANSPARENT COMPOSITE ELECTRODES WITH ULTRA-THIN METAL LAYERS

4.1 Introduction

Transparent conducting oxides (TCOs), especially indium tin oxide (ITO), are widely used for electrodes in solar cells, flat-panel displays and organic light emitting diodes.[8, 31, 33, 42] However, since ITO contains the expensive rare-earth element indium, it cannot be used for low-cost high-volume manufacturing.[114] Transparent composite electrodes (TCE) are promising alternatives to ITO electrodes.[8, 31, 42] TCEs have optical and electrical properties[33, 37] that are comparable to those of ITO, with the added benefit of a substantially lower cost of fabrication (due to the absence of indium). Optical transmittances as high as 85% and resistivities as low as 10^{-5} Ω-cm have been reported for indium-free TCEs.[8, 31, 33, 42]

In a TCE, a layer of metal is embedded between two layers of transparent metal oxide (TMO), forming a TMO/metal/TMO composite structure.[8, 9, 31, 33, 37-44, 114] The choice of materials for the TMO and the embedded metal layer has a significant effect on the final optical and electrical properties of the TCEs.[9] As a result, TCE design is often optimized by trial and error. However, the high cost and the time required for this approach can impede the development of future TCEs. In contrast, having a proper model to analytically predict the TCE transmittance can effectively facilitate materials selection and feature-size design. The transfer-matrix method has been widely used for calculating the transmittance of multilayer thin-film structures.[51, 52, 54-56] However, we have to be careful when predicting the transmittance of ultra-thin films. In this study, two different

TCEs, $TiO_2/Au/TiO_2$ and $TiO_2/Ag/TiO_2$, are fabricated on glass, and their transmittance spectra are measured. The measured spectra are then compared with spectra calculated using the transfer-matrix method. We find that the transmittance predicted by the transfer-matrix method deviates significantly from the measured transmittance when the TCE includes an ultra-thin plasmonic Ag layer. This finding implies that the continuity of the metal layer in the TCE sample significantly impacts the accuracy with which the transmittance can be predicted. To validate it, we will fabricate $TiO_2/Ag/TiO_2$ that contains thick and continuous Ag layer. If the predicted transmittance and measured transmittance of $TiO_2/Ag/TiO_2$ that contains continuous Ag layer match, the conclusion that ultra-thin plasmonic Ag layer in TCEs affects the accuracy of transmittance prediction.

4.2 Model

An electromagnetic wave contains two perpendicular components: an electric field and a magnetic field. In its simplest form, the transmittance is defined as the ratio of the intensities of the transmitted and incident waves through a medium. The transmittance depends on the refractive index, thickness, and roughness of each of the layers through which the light is propagating.[51]

When light propagates in a TCE multilayer thin film, multiple reflections occur in each layer. Therefore, the total light transmitted through all of the layers becomes a summation of the directly transmitted wave plus all of the other transmitted waves that are created by the multiple reflections.[51, 52, 115] It is laborious and time-intensive to determine the TCE's transmittance by analytically calculating the multiple reflections in

each layer and summing them up as described above. However, the calculations can be simplified by using the transfer-matrix method[52, 54-56]. In this approach, those waves (electric fields) that are propagating in the same direction and at the same side of an interface are represented by a single equivalent electric field, as shown in Figure 4.1. The transmittance is then calculated by correlating the incident electric field and the ultimate transmitted electric field via matrix operations.[54-56]

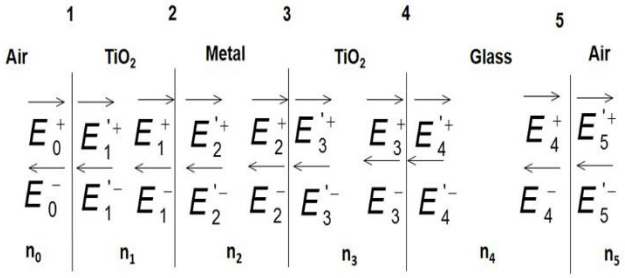

Figure 4.1 Schematic of light amplitudes and intensities within a TCE on glass. The subscripts signify the layer number; + and – signs represent forward and backward directions, respectively. A prime is used for waves at the right-hand side of an interface.

In the transfer matrix method, different layers can be treated as being either coherent or incoherent depending on their thickness, and different matrix operations are used for the coherent and the incoherent layers.[54-56] The thin-film layers in a TCE whose thicknesses are smaller than the wavelength of light will experience internal interference. To account for this, narrow oscillations must be considered in the calculations, and the thin TCE layers have to be considered as coherent layers.[55, 56] The transparent glass substrate of a TCE, on the other hand, has a thickness that is much greater than the wavelength of light. Interference-destroying effects will occur, and narrow oscillations are typically not observed in the measured spectra. This is due to the nonparallel surfaces of the thick layer and the limited resolution of the measurement equipment.[55, 56]

Therefore, the glass substrate should be treated as an incoherent layer. This makes TCE on glass a combination of coherent and incoherent layers for the purpose of transfer-matrix calculations.

As mentioned above, the transmittance depends on the roughnesses of the thin-film interfaces, and of the surface. These roughnesses can cause light scattering, and therefore, a decrease in transmittance[57, 58]. Scattering factors, defined by scattering theory,[57, 58] are incorporated into the matrix operators to account for these effects[56].

4.3 Experimental

Multilayer thin films of TiO_2/Au/TiO_2 and TiO_2/Ag/TiO_2 were used to study the factors that affect the accuracy of the prediction of transmittance. TiO_2/Au/TiO_2 and TiO_2/Ag/TiO_2 thin films were deposited onto glass substrates by RF sputtering of a TiO_2 target (99.9% purity) and DC sputtering of an Au or Ag target (of 99.9% purity), sequentially. The sputtering was performed at room temperature. The TiO_2 thin films were deposited under a pressure of 20 mTorr of Ar gas and with an RF power of 150 W. Au and Ag thin films were deposited under 10 mTorr of Ar gas with 40 W DC power. Different layer thicknesses were obtained by changing the deposition time.

The optical transmittance of the TCE samples was measured for a wavelength range of 300 to 1050 nm. The measurements were performed using a double-channel spectrometer, with air as a reference. A variable angle spectroscopic ellipsometer and WVASE 32 software were used to determine the refractive indices of all of the layers and the thicknesses of the TiO_2 and Au layers. The Ag layer thickness was determined by Rutherford backscattering spectrometry (RBS). The refractive indices of the Au and Ag

films were extracted from metal/TiO_2/glass structures that were fabricated using the same deposition conditions as their corresponding TCE layers. The RMS roughness values of the surface and each interface were estimated by atomic force microscopy (AFM) analysis in tapping mode. Table 4.1 lists the thickness and roughness of each layer. The morphologies of the metal layers (in the Ag/TiO_2/glass and Au/TiO_2/glass stacks) were evaluated using plan-view and cross-section secondary electron microscopy (SEM) and secondary-electron imaging in a Nova 200 Nanolab focused ion beam (FIB) tool.

Table 4.1 The thickness of each layer and the rms roughness of each surface and interface in TCEs

		TiO_2/Au/TiO_2	*TiO_2/Ag/TiO_2*
Thickness (nm)	Layer 1	38	30
	Layer 2	10.5	12
	Layer 3	40	30
	Layer 4	10^6	10^6
RMS roughness (nm)	Surface 1	1.75	1.82
	Interface 2	0.68	1.19
	Interface 3	0.77	0.77
	Interface 4	0.26	0.26

4.4 Results and Discussion

Experimentally extracted physical parameters (thickness, roughness and refractive indices) were incorporated into transfer matrices to determine the TCE transmittance. Subsequently, the calculated and the measured transmittance spectra of the TCE were compared with each other. As is evident in Figure 4.2, the calculated and measured transmittance spectra of TiO_2/Au/TiO_2 are in good agreement over the entire 300 to 800 nm range.

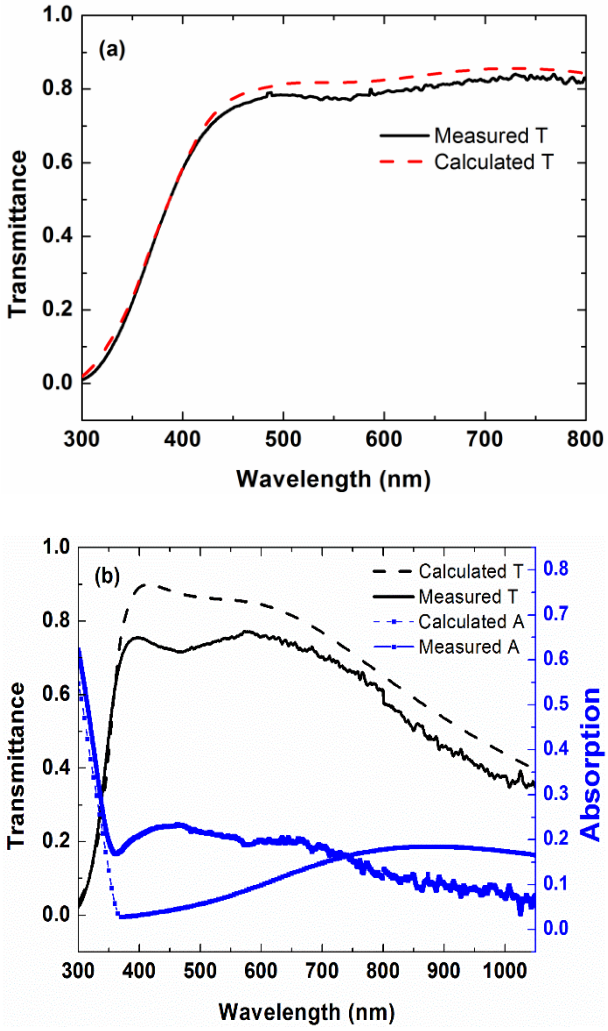

Figure 4.2 (a) Measured and calculated optical transmittance spectra from TiO_2/Au/TiO_2 multilayer thin-film on glass substrate; (b) Measured and calculated optical transmittance and absorbance spectra from TiO_2/Ag (12nm)/TiO_2 multilayer thin-film on glass substrate.

However, there is an offset between the calculated and measured transmittance spectra of TiO_2/Ag/TiO_2/glass (Figure 4.2 (b)). The calculated transmittance is approximately 20% higher than the measured transmittance. Han *et al.* have reported that a discontinuous Ag layer in MoO_3(30 nm)/Ag(11 nm)/MoO_3(30 nm) can cause a decrease in transmittance over the visible light region.[116] They showed that increasing the number of voids in the Ag layer will lead to increased light absorption, and therefore, decreased

transmittance.[116] However, they did not provide a clear explanation for the extra light absorption.

Based on the inference of Han *et al.*[24], we inspected the morphology of the Ag and Au layers using SEM. The Ag/TiO_2/glass and Au/TiO_2/glass samples were fabricated using the same deposition conditions as their corresponding TCEs. Therefore, the Ag and Au layers in these samples can be viewed as being representative of the metal layers that are embedded within the TCEs. Plan-view SEM micrographs of the Ag and Au surfaces are shown in Figure 4.3. These show a relatively smooth Au surface and a more islanded (or hillocked) Ag surface. Cross-section SEM micrographs (not shown here) also confirm that the Ag layer is islanded. The data indicate that a continuous Au layer is present in TiO_2/Au/TiO_2 (whose calculated and measured transmittance spectra are quite similar). In contrast, the Ag layer in TiO_2/Ag/TiO_2 is actually a mixture of Ag islands interspersed with TiO_2. The presence of these Ag islands results in localized surface plasmons (LSPs). This then causes increased light absorbance and lower transmittance as seen in the measured spectra.

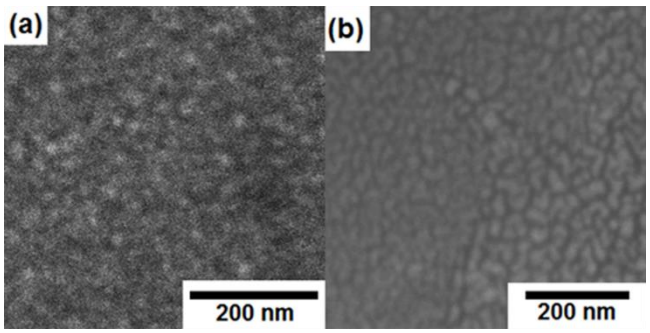

Figure 4.3 SEM images from the surface of (a) Au (10.5 nm)/TiO_2 on glass and (b) Ag (12 nm)/TiO_2 on glass.

The Ag islands interspersed with TiO_2 are analogous to Ag nanoparticles embedded within TiO_2.[117] It is known that localized surface plasmons will occur when incident light interacts with free electrons in Ag nanoparticles.[118-120] These surface plasmons are collective oscillations of electrons that are mostly confined to the vicinity of the nanoparticle's surface.[120] Such LSPs can cause enhanced light absorption.[117-121] As a result, an absorption peak will be observed at the LSP resonance frequency.[120, 121] The measured absorption spectrum of our TiO_2/Ag/TiO_2 sample, in Figure 4.2(b), shows a broad absorption band, indicating the occurrence of LSP. The absorption is in a broad band rather than a sharp peak at the resonance frequency. This is because the LSP absorption band will be broadened when the size and the size distribution of the nanoparticles increases.[122, 123] As can be seen in Figure 4.3, the sizes of the Ag islands are in the range of 10 to 80 nm. Such a wide distribution of island sizes can give rise to LSP absorption over a broad range of wavelengths. The calculated absorption (in the wavelength range of 300 nm to 750 nm) is lower than the measured absorption, as shown in Figure 4.2(b). This is because the effects of LSPs are not included in the proposed calculation/model. Therefore, the calculation cannot correctly predict the absorption when LSPs are present.

In our proposed model, the Ag layer is considered to be continuous and to have the same roughness as that of the Ag layer in the experimental TCE. At the interface between the dielectric and the continuous Ag layer, surface plasmon polaritons (SPPs) can occur instead of LSPs, under certain circumstances. Such SPPs can propagate along the interface, and cause light absorption.[120, 121] However, SPPs cannot be excited as easily as LSPs, and they can only occur when the horizontal part of the incident light's wave

vector matches the wave vector of the surface plasmon.[117, 124, 125] Therefore, SPPs cannot be excited directly by light that is traveling (through a planar dielectric medium that is adjacent to the Ag) in a direction that is perpendicular to the dielectric/Ag interface. Instead, a prism, grating or large surface roughness is needed to induce the appropriate propagating wave vectors of the light.[117, 125] Normal incident light is used in our approach. As a result, SPPs and the corresponding extra light absorption will not occur in the proposed model.

LSPs, SPPs and their corresponding light absorption are not taken into account in the proposed calculation model. Therefore, the calculated transmittance is higher than the measured transmittance for the TiO_2/Ag/TiO_2 sample (over the wavelength range of 360 to 750 nm). Above 750 nm, the LSP absorption (in the measured spectrum) is negligible. In this region, absorption is caused by intraband transitions of electrons (classic infrared absorption), and this depends on the density of electrons.[15] As a result, the discontinuous Ag layer in the TiO_2/Ag/TiO_2 sample (which has a lower electron density than that of the continuous Ag layer in the TCE model) causes less light absorption (than the continuous Ag layer in the TCE model does) above 750 nm.

As discussed above, the discontinuous metal layer in TCE cannot results in an accurate prediction of optical transmittance, and the predicted transmittance is lower than the measured transmittance. However, we have another interesting finding that the dependence of transmittance on layer thickness can be roughly predicted using this transfer matrix method even when TCE contains discontinuous metal layer. 10 nm Ag layer is picked as the middle layer and the TiO_2 layer is varied from 35 nm to 42 nm.

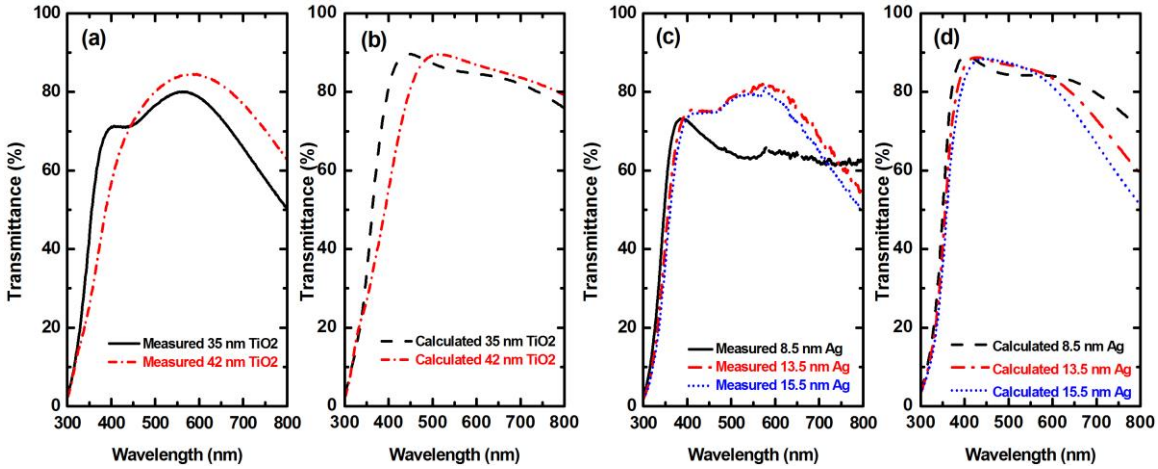

Figure 4.4 Transmittance spectrum for TiO_2/Ag/TiO_2: (a) measured transmittance for TiO_2/(10nm) Ag/TiO_2 with TiO2 thickness at 35 nm and 42 nm, (b) calculated transmittance for TiO_2/(10nm) Ag/TiO_2 with TiO2 thickness at 35 nm and 42 nm, (c) measured transmittance for (30 nm)TiO_2/Ag/(30 nm) with Ag thickness at 8.5 nm, 13.5 nm and 15.5 nm, (d) calculated transmittance for (30 nm)TiO_2/Ag/(30 nm) with Ag thickness at 8.5 nm, 13.5 nm and 15.5 nm.

Figure 4.4 (a) and (b) show the measured and calculated transmittance. The measured transmittance decreases as TiO_2 thickness increases in low wavelength range, but it increases as TiO2 thickness in long wavelength range. It turns out the transfer matrix method successfully predict this trend. Then the TiO_2 thickness is fixed at 30 nm, and the Ag layer thickness varies from 8.5 nm to 15.5 nm to study the transmittance dependence on Ag thickness as shown in Figure 4.4 (c) and (d). Blow 400 nm, the transmittance does not show significant dependence on Ag thickness. Between 400 and 700 nm wavelength, transmittance increases as Ag thickness, and then the transmittance decreases as the thickness increases beyond 700. The calculated transmittance successfully predict this dependence between 400 nm and 600 nm and beyond 700. According to these results, the transfer matrix method can successfully predict the dependence of transmittance on the layer thickness. As a result, the trend of transmittance

when the layer thickness changes can be successfully estimated, which is helpful for estimating the optimal layer thicknesses for specific applications.

The discussion above suggests that if the TCE sample has a continuous Ag layer, the conventional (previous) model can represent the TCE sample well, and it can accurately predict the transmittance. Hence, the transmittance spectrum that is calculated for the $TiO_2/Ag/TiO_2$ structure with a continuous silver layer should agree with the corresponding measured transmittance spectrum.

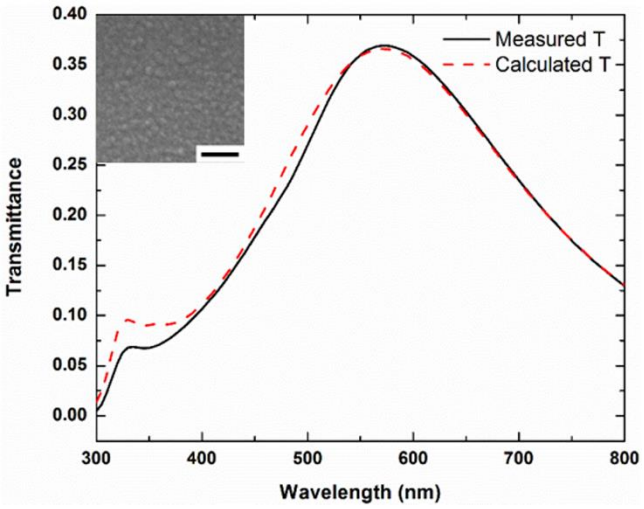

Figure 4.5 Measured and calculated optical transmittance for TiO_2/Ag (36 nm)/TiO_2 multilayer thin-film on glass substrate for 300 nm to 800 nm wavelengths. The insert is a SEM micrograph obtained from Ag (36 nm)/TiO_2 on glass. The scale bar in the SEM image is 200 nm.

To validate this, a $TiO_2/Ag/TiO_2$ sample with a thick Ag layer (36 nm) was fabricated. The thickness was deliberately chosen to be high enough to ensure continuity of the Ag layer. The morphology of the 36 nm Ag film on TiO_2/glass substrate is visible in Figure 4.5. A cross-section of this Ag/TiO_2/glass (not shown here) indicates that the Ag layer is continuous. AFM analysis of the 36 nm Ag layer shows a *Z* range of 16.6 -19.5 nm,

which further confirms the continuity of the 36 nm Ag layer. The calculated and measured transmittance spectra of the TiO_2/Ag (36 nm)/TiO_2 are presented in Figure 4.5. As expected, the two spectra match quite well. This confirms that the prediction of TCE transmittance using transfer-matrix calculations is valid. However, such predictions are valid only for designing TCEs with continuous layers. It can be seen that the transmittance of TiO_2 /Ag (12 nm)/TiO_2/glass that is calculated assuming a continuous metal layer is more than 85% across 400 nm to 670 nm. This implies that a transmittance as high as 90% can be achieved for a TiO_2/Ag/TiO_2 TCE, if the TCE contains a continuous Ag layer with a thickness of 12 nm.

4.5 Conclusion

The transfer-matrix method for mixed coherent and incoherent layers was used to predict the optical transmittance of TiO_2/Au/TiO_2 and TiO_2/Ag/TiO_2 TCEs. The factors that might affect the accuracy of the prediction were studied. It was shown that predicting the transmittance of a TCE with a continuous metal layer is quite reliable using the transfer matrix method. For a TCE with a discontinuous and plasmonic metal layer, the predicted transmittance no longer matches the measured values. Our results show that a discontinuous metal layer in a TiO_2/Ag/TiO_2 sample, which results in an intermixed layer of Ag islands and TiO_2, causes the actual transmittance to be lower than the predicted values. This happens due to enhanced light absorption that is caused by LSPs in the surface of Ag islands. The enhanced light absorption in the TiO_2/Ag/TiO_2 sample, over the wide visible light range, is due to the large size distribution of the Ag clusters. However, the prediction typically assumes that the metal layers are continuous and that there are no LSPs occurring. Therefore, this results in a predicted transmittance that is

higher than the measured values. On the other hand, the trend of transmittance as layer thicknesses changes can be successfully predicted by transfer matrix method. It's helpful for estimating the optimal layer thickness for specific application. the Our study shows that the plasmonic nature of metals and the continuity of metal layers significantly impact the accuracy of the transmittance prediction for multilayer thin film structure.

5. THE OPTIMAL TRANSPARENT COMPOSITE ELECTRODES FOR ORGANIC SOLAR CELL APPLICATION WITH HIGH DEVICE-SPECIFIC HAACK FIGURE OF MERIT

5.1 Introduction

A typical TCE is a three-layer structure: equivalent top and bottom transparent metal oxide (TMO) layers and an intermediate metal layer [9, 33, 37-41, 126-133]. TiO_2 has a wide band gap of ~ 3.4 eV, and this renders it to be transparent in the visible light spectrum [127]. The high dielectric constant, strong mechanical and chemical stability and low fabrication cost make TiO_2 a suitable material for TMO layer in TCE [127]. Ag is an ideal candidate for the metal layer in TCE [134]. Its real part of the refractive index is the one of the lowest among metals and this will help minimize the light absorption of metal layer. Moreover, the resistivity of Ag is one of the lowest of the noble metals, which will help improve the resistivity of TCE. As a result, TiO_2/Ag/TiO_2 is a potentially promising candidate of TCEs. Moreover, our previous work has demonstrated that the TiO_2/Ag/TiO_2 transparent composite electrode is a promising alternative to ITO[32]. The Haacke figure of merit of the optimized TiO_2/Ag/TiO_2 on flexible polymer substrate over the whole visible light spectrum is as high as 61.4×10^{-3} Ω^{-1}/sq, which is higher than ITO[42]. The superior properties of TiO_2/Ag/TiO_2 drive us to fabricate organic solar cells (OSCs) on it, and to study and compare their performance with OSCs on ITO.

To be a desired electrode, the layer thickness of TCE has to be optimized such that its transmittance and resistance are desirable. The optimization of the transmittance of TCE across the entire visible light region has been studied by several investigators [38, 42, 114, 126-128, 133]; however, few report actually tailoring the indium-free electrode's

transmittance to the organic solar cell's absorption spectrum. As discussed in last chapter, the transfer matrix method was proved to be able to estimate the optimal layer thickness of TCE for specific application since it can roughly predict the transmittance dependence on layer thickness. As a result, In this study, the transfer matrix method will be employed to estimate the optimal thickness of TCE for P_3HT:PCBM organic solar cell application.

In our study, multilayer structures of TiO_2/Ag/TiO_2 are fabricated on glass substrates by room-temperature sputtering. Initially, the effect of Ag deposition rate on TCE's optical transmittance and sheet resistance is studied. Once the optimal Ag deposition rate is obtained that gives a relatively low sheet resistance and high transmittance in TCEs, then the thicknesses of TiO_2 and Ag layers are optimized, such that the maximum transmittance of the TiO_2/Ag/TiO_2 electrode is within the specific wavelength region (450 nm - 600 nm). Results demonstrate that the device-specific Haack FOM for optimized TiO_2/Ag/TiO_2 is significantly higher than that of ITO-based structures. Hence, TCE parameters can be tailored for the specific a photovoltaic application.

5.2 Experimental

The multilayer structure of TiO_2/Ag/TiO_2 was sputter deposited on glass substrate at room temperature with a base pressure of 8×10^{-7} Torr. The bottom TiO_2 layer was deposited by RF sputtering of a TiO_2 target (99.9% purity) with a power of 66 W and Ar pressure of 2.5 mTorr. Sequentially, the middle Ag layer was deposited by DC sputtering of an Ag target (99.9% purity) at Ar pressure of 4 mTorr. Various DC power were used

to achieve different deposition rate of Ag. Finally, the top TiO_2 layer was deposited on Ag layer using the same deposition condition as the bottom TiO_2. The thickness of each layer is confirmed by the variable angle spectroscopic ellipsometer measurement and WVASE 32 software analysis. The optically transmittance was measured by Cary 5000 UV-Vis spectrometer over 300 nm to 800 nm. The sheet resistance was determined by four-point probe analysis. Secondary electron microscopy (SEM) was conducted to evaluate the surface morphology of Ag layers that were deposited on TiO_2/glass using different sputtering rates.

5.3 Results and Discussion

The deposition rate of Ag affects the morphology of Ag layer [50], which in turn might impact the optical transmittance of TCE [116] due to the light scattering effect at the Ag and TiO_2 interface [57, 58] or light absorption caused by localized surface plasmons at the Ag vicinity [135]. To study the effect of the Ag deposition rate on TCE's optical transmittance and sheet resistance, three sets of TCE samples with the same layer thickness were prepared using various Ag deposition rates (0.03 nm/s, 0.18 nm/s, and 0.40 nm/s). Their optical transmittance and sheet resistance are compared in Figure 5.1.

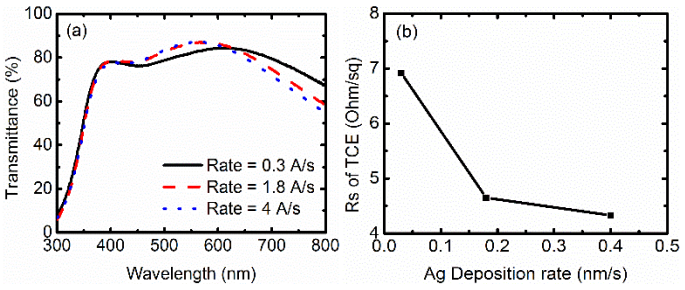

Figure 5.1 (a) The optical transmittance of (30 nm) TiO_2/ (10 nm) Ag/ (30 nm) TiO_2 fabricated with various Ag deposition rate. The glass substrate is taken as

the reference. (b) The sheet resistance as a function of Ag deposition rate from (30 nm) TiO_2/ (10 nm) Ag/ (30 nm) TiO_2

The TCEs with high Ag deposition rate (0.18/s and 0.40 nm/s) shows almost identical transmittance spectrum and similar sheet resistance values. On the other hand, TiO_2/Ag/TiO_2 prepared by low Ag deposition rate (0.03 nm/s) gives two times higher sheet resistance and relatively lower transmittance in the wavelength range of 400 nm to 600 nm. To investigate the reason for the differences and similarities in the transmittance and sheet resistance of above TECs, the morphology of Ag layers deposited by different rates is further studied with the use of SEM. The SEM micrographs of Ag films are shown in Figure. 5.2, and indicate that all three deposition rates result in non-continuous films that contain voids. The voids are relatively large but in a small amount when the Ag deposition rate is 0.18 nm/s and 0.40 nm/s. This similarity in morphologies of Ag deposited at 0.18 nm/s and 0.04/s explains their similarity in TCEs' transmittance spectra and sheet resistances. On the other hand, many tiny voids are evenly distributed in the Ag film when deposition rate is low (0.03 nm/s). These voids tend to disrupt the continuous path of the flowing current. As a result, the sheet resistance of TCE is the highest when its Ag layer is deposited at 0.03 nm/s. Similarly, due to this relatively high voids density in Ag layer deposited at low rate (0.03 nm/s), its TCE's transmittance is lower in the wavelength between 450 nm and 600 nm. Based on the comparison above, the TECs with the Ag layers deposited at 0.18 nm/s and 0.40 nm/s both shows the optimal sheet resistance and optimal transmittance between 450 and 600 nm. As a result, 0.4 nm/s is selected as the optimal deposition rate for Ag layer in our study.

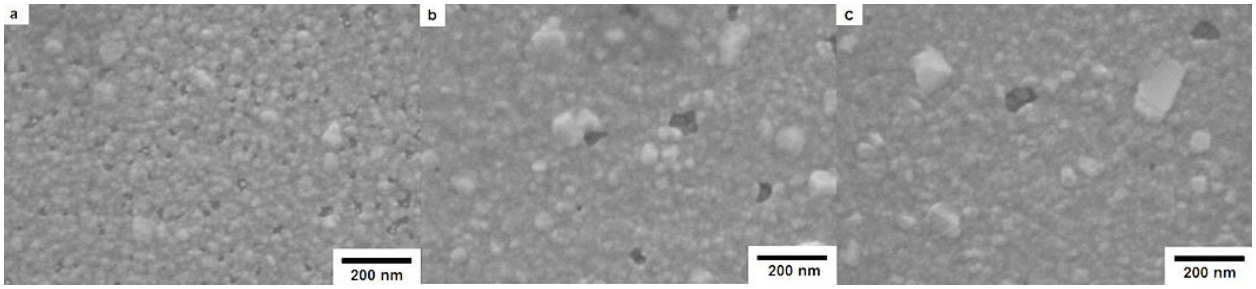

Figure 5.2 SEM micrographs for 10 nm Ag film on TiO2/glass deposited at rates of a) 0.03 nm/s, b) 0.2 nm/s, and c) 0.4 nm/s.

For electrodes used in organic solar cell and light emitting diodes, optimizing the average transmittance over the entire visible light spectrum might not be able to satisfy the specific needs of the devices. For example, the light absorption peak of the active layer in $P_3HT:PC_{61}MB$ organic solar cell is between 450 nm to 600 nm [136]. Maximizing the average transmittance of TCE across 450 nm to 600 nm can specifically increase the light input to the organic solar cells. Before the experimental optimization of layer thickness to achieve high transmittance over the wavelength of 450 nm to 600 nm, the numerical simulation of TCE's transmittance via transfer-matrix method is used to estimate the optimal thickness of TiO_2 and Ag layers [135]. Through the simulation, the range of desired thickness for experimental fabrication is narrowed, which facilitates the optimization process. Our previous study has shown that the percolation threshold (where the Ag islands begin to connected with each other and form network) of Ag film is approximately 9.5 nm in TiO_2/Ag/TiO_2 structures on flexible substrate [127]. Hence, the Ag layer is fixed at 10 nm in the simulation, then the TiO_2 layers are varied from 30 nm to 50 nm to determine the optimal thickness. The simulated dependence of transmittance spectrum on the TiO_2 layer thickness is shown in Fig. 4.3(a). The red shift occurs at the absorption edge when the top and bottom TiO_2 thickness increases. Results show that

TiO_2 thickness between 35 nm to 45 nm gives the optimal transmittance over 450 nm and 600 nm.

To determine the optimal Ag thickness, the TiO_2 layers are fixed at the 40 nm and the silver thicknesses vary from 8 nm to 14 nm. The simulated dependence of transmittance on Ag layer thickness is shown in Fig. 4.3(b). In this case, the TCE having 10 nm Ag layer shows the optimal transmittance over 450 to 600 nm.

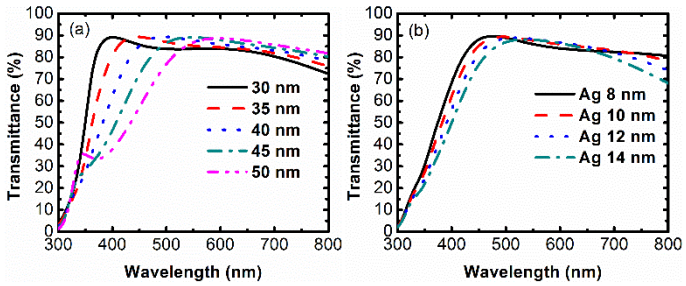

Figure 5.3 (a) The simulated transmittance of TiO_2/Ag (10 nm)/TiO_2 with different TiO_2 thicknesses of 30 nm, 35 nm, 40 nm, 45 nm and 50 nm. (b) The simulated transmittance of TiO_2 (40 nm)/Ag/TiO_2 (40 nm) with different Ag thickness of 8 nm, 10 nm, 12 nm and 14 nm.

It is noticed that the simulation results can only provide the first-order approximation of the transmittance's dependence on the layer thicknesses. The actual transmittance of the fabricated TCE might deviate from simulated transmittance due to the discontinuity of the metal film [135]. The optimal layer thickness obtained by simulation is ideal for continuous films; however for the non-continuous film in this study, the thicknesses obtained by simulation are in the range of optimal thickness values. Hence, the layer thicknesses near the optimal thickness are selected for fabrication.

Based on the transmittance simulation results, two different thicknesses (35 nm and 42 nm) of TiO_2 are selected for experimental fabrication. In addition to the consideration of optical transmittance, the sheet resistance of TCE has to be taken into

account in order to maximize the Haacke FOM [47] across 450 nm to 600 nm. The sheet resistance of TCE is mainly determined by metal layer[134]. A thicker metal film in the TCE results in a lower sheet resistance and unfortunately a lower transmittance as well. As a result, even 10 nm is the optimal Ag thickness for achieving high transmittance, the Ag thicknesses of 8.5 nm and 13 nm are also selected for TCE fabrication in order to achieve a trade-off between sheet resistance and optical transmittance.

Six sets of TCEs are fabricated. As the alternative to ITO, their properties are compared with ITO. The optical transmittance spectra are shown in Fig. 4.4. The sheet resistances are shown in Table 4.1. From these results, the TCEs show an overwhelming advantage over ITO in terms of sheet resistance; where, the sheet resistance values of the TCEs are typically at least three times lower than that of the ITO.

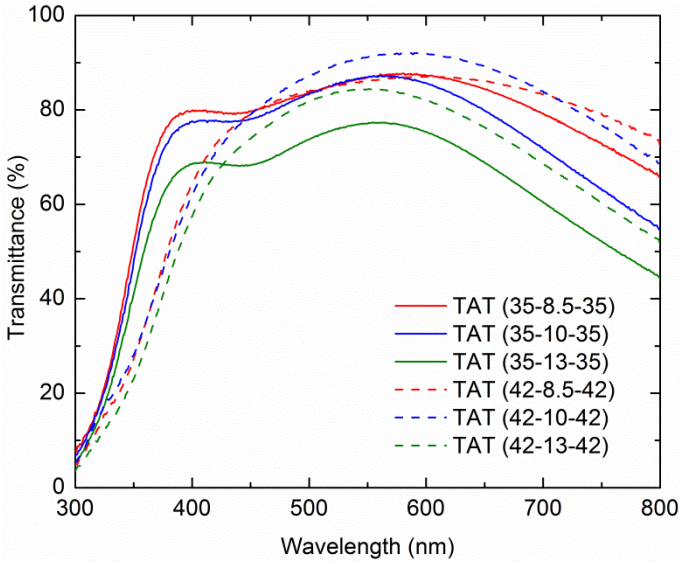

Figure 5.4 The optical transmittance spectra for TiO_2/Ag/TiO_2 (TAT) on glass as a function of TiO_2 thickness and Ag thickness. Glass substrate as the reference.

The Haack figure of merit (φ_{TC}) takes into account of both sheet resistance and transmittance, and it is calculated as following [47]:

$$\varphi_{TC} = \frac{T_{av}^{10}}{R_s} \tag{5.1}$$

where the T_{av} is the average transmittance, R_s is the sheet resistance.

Table 5.1 The sheet resistance, average transmittance over 450 nm and 600 nm and the corresponding Haacke FOM of ITO and TiO_2/Ag/TiO_2 that having different TiO_2 and Ag thickness.

Sample	*R*s	T_{ave}	Device specific Haack FOM (sq/Ω)
ITO	18.9	0.96	35.2×10^{-3}
TiO_2(35 nm)/Ag(8.5 nm)/ TiO_2 (35 nm)	5.62	0.85	35.0×10^{-3}
TiO_2(35 nm)/Ag(10 nm)/ TiO_2 (35 nm)	4.33	0.84	40.4×10^{-3}
TiO_2(35 nm)/Ag(13 nm)/ TiO_2 (35 nm)	3.74	0.74	13.2×10^{-3}
TiO_2(42 nm)/Ag(8.5 nm)/ TiO_2 (42 nm)	5.95	0.85	33.1×10^{-3}
TiO_2(42 nm)/Ag(10 nm)/ TiO_2 (42 nm)	4.48	0.89	69.6×10^{-3}
TiO_2(42 nm)/Ag(13 nm)/ TiO_2 (42 nm)	3.50	0.82	39.3×10^{-3}

Since the TCEs are used in the application for P_3HT:$PC_{61}MB$ organic solar cell (OSC), we are interested in the wavelength range between 450 nm and 600 nm (where the OSC is most efficient [136]). The Haccke FOM in this wavelength range is defined as device-specific Haacke FOM here. The average transmittance over 450 nm and 600, and device-specific Haacke figure of merit are compared in Table 4.1. Among all the TCEs and ITO, TiO_2 (42 nm)/Ag (10 nm)/ TiO_2 (42 nm) proposes the highest device-specific Haacke FOM. More importantly, its device-specific Haack FOM is two times higher than

that of ITO. In conclusion, we have demonstrated that the optimized $TiO_2/Ag/TiO_2$ shows much better performance regarding the Haacke FOM.

5.4 Conclusion

As the alternative electrodes for organic solar cell (OSC) devices, $TiO_2/Ag/TiO_2$ TCE's thicknesses were optimized for that specific wavelength range of 450 nm to 600 nm. This range corresponds to the light absorption peak of the active layer in $P_3HT:PC_{61}MB$ OSC. The morphology of the Ag layer in TCE impacts the transmittance and sheet resistance of TCE. Hence, the Ag deposition rate that affects the morphology of the Ag layer was studied in the beginning. The high deposition rates, 0.18 nm/s and 0.40 nm/s, both result in less void density in Ag layer, leading to lower sheet resistance and higher transmittance in the TCEs, as compared to low deposition rate (0.03 nm/s). Therefore, the optimal Ag deposition rate is determined as 0.40 nm/s. To increase the light input to the $P3HT:P_{61}MB$ layer, the Haacke FOM of $TiO_2/Ag/TiO_2$ electrode are specifically optimized across the wavelength from 450 nm to 600 nm. Initially, theoretical simulations are used to estimate the optimal layer thicknesses for achieving highly transparent TCEs. It narrows the possible layer thicknesses for experimental fabrication and facilitates experimental optimization. In experimental fabrication, by varying the layer thickness of Ag and TiO_2 near the optimal values, it shows that TiO_2(42 nm)/Ag(10 nm)/ TiO_2(42 nm) has the device-specific Haacke FOM as high as 69.6×10^{-3} sq/Ω, which is two times better than that of the ITO-based structure. In other word, the TCE parameters is able to be tailored for the specific a photovoltaic application.

6. THE INDIUM-FREE TRANSPARENT COMPOSITE ELECTRODE AND ITO ELECTRODE BASED P_3HT:PCBM ORGANIC SOLAR CELLS AND THEIR COMPATIBLE HOLE TRANSFER LAYERS

6.1 Introduction

The transparent conductive electrodes that allows the light transmission and emission as well as electrical conduction is an essential component in the organic solar cells (OSCs) and light emitting diodes [33, 126-128]. Their electrical and optical properties significantly affect the device's efficiency. Indium-tin oxide (ITO) is one of the most widely used transparent conductive electrode materials due to its high optical transmittance and low resistivity[33, 126-129]. However, the rare-earth element indium in ITO limits its sustainability and increases its coat. More importantly, ITO is brittle. This becomes a major concern during the implementation of this material into flexible devices [127, 129, 137]. As a means to address this concern, transparent composite electrodes (TCEs) have been reported as a promising alternative to ITO-based electrodes due their indium-free composition, good mechanical flexibility, the low processing temperature, and superior figure of merit (FOM) [38, 126-128].

A typical TCE is a three-layer structure: equivalent top and bottom transparent metal oxide (TMO) layers and an intermediate metal layer [9, 33, 37-41, 126-133]. The optical properties of TCE can be tailored to different application by varying the thickness and materials of each individual layer [138]. In last chapter, we have studied the optimal thickness and materials for TCE when it was employed as electrode for bulk heterojunction organic solar cells [139]. TiO_2/Ag/TiO_2 (TAgT) on glass with 42 nm TiO_2 top and bottom layers and 10 nm Ag layer showed a high device-specific Haacke figure

of merit of 69.6 x 10^{-3} sq/Ω, which is almost twice higher than that of ITO [139]. In this chapter, this optimized TAgT will be incorporated into OSCs, and compared with ITO based OSC. The effect of TAgT and ITO anodes on OSC's performance will be further compared and studied in this paper.

Apart from anode, the interface layer also plays an important role in the performance of OSC. The interface layer is typically used to: adjust the band alignment between electrode and active layer to form ohmic contact, selectively transport only one type of carriers, prevent the chemical reaction between electrode and active layer and act as an optical spacer to adjust incident light distribution [70, 75]. The interface layer between the anode and active layers is called the hole transfer layer (HTL). Typical HTL materials include: conventional poly(3,4-ethylenedioxythiophene):poly(styrene sulfonate) (PEDOT:PSS), semiconducting transition metal oxide such as molybdenum oxide (MoO_3), vanadium oxide (V_2O_5) , nickel oxide (NiO) and tungsten oxide (WO_3), organic hole-transporting materials such as poly[9,9-dicotylfluorene-co-N-[4-(3-methylpropyp)]-diphenyl-amine] (TFB) and 4,4'-bis[(p-trichlorosiylpropylphenyl)phenylamino]biphenyl ($TPDSi_2$) [70, 71, 75, 140]. Particularly, PEDOT:PSS is the most widely used HTL materials due to its ease for fabrication; however, PEDOT:PSS etches the anode (ITO and other transparent conductive oxide) due to its acidic nature and results in degradation of OSC [70, 75, 140, 141]. To avoid the attack of PEDOT:PSS to anode, MoO_3 is reported as a promising alternative by many researchers [70, 71, 75, 140, 142, 143], considering it has no chemical reaction with the anode. Due to the high work function of MoO_3, the band bending of HOMO at MoO_3/organic interface and gaps states due to oxygen vacancy defects in MoO_3 enhances the hole extraction from the donor to anode [142-145]. Since new

anode TAgT are used in our study, both PEDOT:PSS and MoO_3 will employed as HTL to study the their compatibility with TAgT. For comparison, ITO based OSC using PEDOT:PSS and MoO_3 HTL are also fabricated and studied as control samples.

In this study, OSCs with different anodes (ITO and TAgT) and two different HTLs (PEDOT:PSS and MoO3) are fabricated, and their performance is compared. The impact of anode and HTL on performance of OSC are investigated. Specifically, the impact of light transmittance and sheet resistance of two different anodes on the light input and seriers resistance (R_{series}) of OSC are studied. In terms of HTL, its impact on OSC's performance, especially on J_{sc}, are studied by investigating its contact at anode and active layer interfaces, and its wettability effect on active layer thickness.

6.2 Experimental

6.2.1 Electrode Fabrication

The multilayer structure of TiO_2/Ag/TiO_2 was sputter deposited on glass substrate at room temperature with a base pressure of 1×10^{-6} Torr. According to our previous finding [139], TiO_2 top and bottom layer with a thickness of 42 nm and Ag middle layer with a thickness of 10 nm are the optimal thickness for OSC application. The bottom TiO_2 layer was deposited by RF sputtering of a TiO_2 target (99.9% purity) with a power of 90 W and Ar pressure of 2.5 mTorr. Sequentially, the middle Ag layer was deposited by DC sputtering of an Ag target (99.9% purity) at Ar pressure of 4 mTorr, and with a power of 235 W.

6.2.2 OSC Fabrication

6.2.2.1 Reagent and Materials

The electrode donor material regioregular poly (3-hexylthiophene) (P_3HT) was from Reike Metals, Inc. The electron acceptor material [6,6]-phenyl C_{61} butyric acid methyl ester (PCBM) and 1,2-dichlorobenzene were from Sigma Aldrich. The hole transfer layer material, poly(3,4-ethylenedioxythiophene):poly (styrenesulfonate) (PEDOT:PSS) with neutral PH value was purchased from Sigma Aldrich as well.

6.2.2.2 Device Fabrication and Testing

Two different types of anodes, ITO and TiO_2/Ag/TiO_2 (TAgT) were used. Two different hole transfer layers, MoO_3 and PEDOT:PSS, were deposited on each type of anodes, respectively. As results, OSC with four different structures were fabricated: ITO/PEDOT:PSS/P_3HT:PCBM/LiF-Al (ITO+PEDOT:PSS), ITO/MoO_3/P_3HT:PCBM/LiF-Al (ITO+MoO_3), TAgT/PEDOT:PSS/P_3HT:PCBM/LiF-Al (TAgT+PEDOT:PSS), TAgT/MoO3/P_3HT:PCBM/LiF-Al (TAgT+MoO_3). MoO_3 film with a thickness of 14 nm, was thermally evaporated from MoO_3 powder (99.99% purity, Alfa Aesar) on ITO and TAgT anodes, respectively. PEDOT:PSS was spin coated on ITO and TAgT anodes at 5000 rpm for 60 s, followed by baking on hot plate at 200 ^oC for 15 min in nitrogen-filled glove box. The electron donor P_3HT and electron acceptor $PC_{61}BM$ with a weight ratio of 1:0.8 were dissolved in the 1,2-dicholorobenzene to make solution containing 20 mg/ml P_3HT. The solution was stirred at room temperature for overnight in nitrogen-filled glove box. Then the blended solution was spin coated at 600 rpm for 60 s, and then baked at 150 ^oC for 30 min in glove box. In the end, the electron transfer layer LiF of 0.7 nm and metal cathode Al of ~80 nm were sequentially deposited

by thermal evaporation using a shadow mask that defines an active area of 0.2 cm^2. The current density-voltage (*J*-*V*) curve were measured under simulated AM 1.5 global solar irradiation (100 mW/cm^2) using a xenon-lamp solar simulator (Spectra Physics, Oriel Instruments, USA).

The evaporation of solvent during and after spin coating enables the phase separation of the immiscible polymer bends (P_3HT:PCBM), resulting in the formation of bulk heterojunction film [71]. However, the solvent evaporation kinetics during spin coating is difficult to control experimentally because of small variation during the process [146]. This results in different extents of phase separation at different days and consequential variation of the power conversation efficiency for solar cells fabricated at different days but using the same process recipe. To take into the account of this variation and obtain sound results and conclusion, we repeated OSC s with four different structure at four different days.

6.2.2.3 Characterization

The work function of ITO and TAgT on glass were measured using Kelvin Probe (McAllister 6500). A highly ordered pyrolytic graphite (HOPG) film with a work function of 4.5 eV was used as the reference sample [147]. Two methods were used to measure the sheet resistance of various films. One method is implemented by a 4-point probe system equipped with a 100 mA Keithley 2700 digital multimeter. Another method is implemented by Van Der Pauw method and equation, and conducted using Ecopia HMS-3000 system. The thickness of MoO_3 film, and spin-coated active layer (P_3HT:PCBM) are measured by stylus profilometer (Dektak XT). The roughness of PEDOT:PSS and MoO3 films are inspected by atomic force microscopy (AFM) (Bruker

Dimension 3100) under 2 μm × 2 μm scan. At the same time, the cross-section profile in Z direction of a 1 μm line in the scanning area are inspected to give a direct profile of the surfaces. The light absorption of anode/HTL/P_3HT:PCBM/LiF-Al OSCs were calculated by subtracting light transmittance from 100%. The light transmittance was measured by Ocean Optics double channel spectrometer (model DS200) in a wavelength range of 300–800 nm. The external quantum efficiency (EQE) in wavelength range of 300–800 nm was evaluated by a QEX10 quantum efficiency measurement system with a xenon arc lamp source and dual-grating monochromator. The internal quantum efficiency (IQE) was calculated by dividing the EQE by the light absorption of the devices.

6.3. Results and Discussion

6.3.1 Overall Performance of Four OSC Structures

Figure 6.1 shows the variability charts of device parameters for the four sets of OSCs fabricated at different days. The centered line indicates the average value of those device parameters. The average values of device parameters for all the four structures are listed in Table I. As an alternative for ITO, TAgT+PEDOT:PSS device shows the worst overall performance in all the device parameters and the bad performance is due to the significantly high R_s. Such high R_s implies that TAgT anode is attacked by PEDOT:PSS even with the use of neutral PH PEDOT:PSS as HTL. To avoid the attack of PEDOT:PSS to TAgT, MoO_3 is used as hole transfer layer to replace PEDOT:PSS. With the use of MoO_3 on TAgT anode, all the device parameters are significantly improved and highest PCE of TAgT+MoO_3 device is 2.38%.

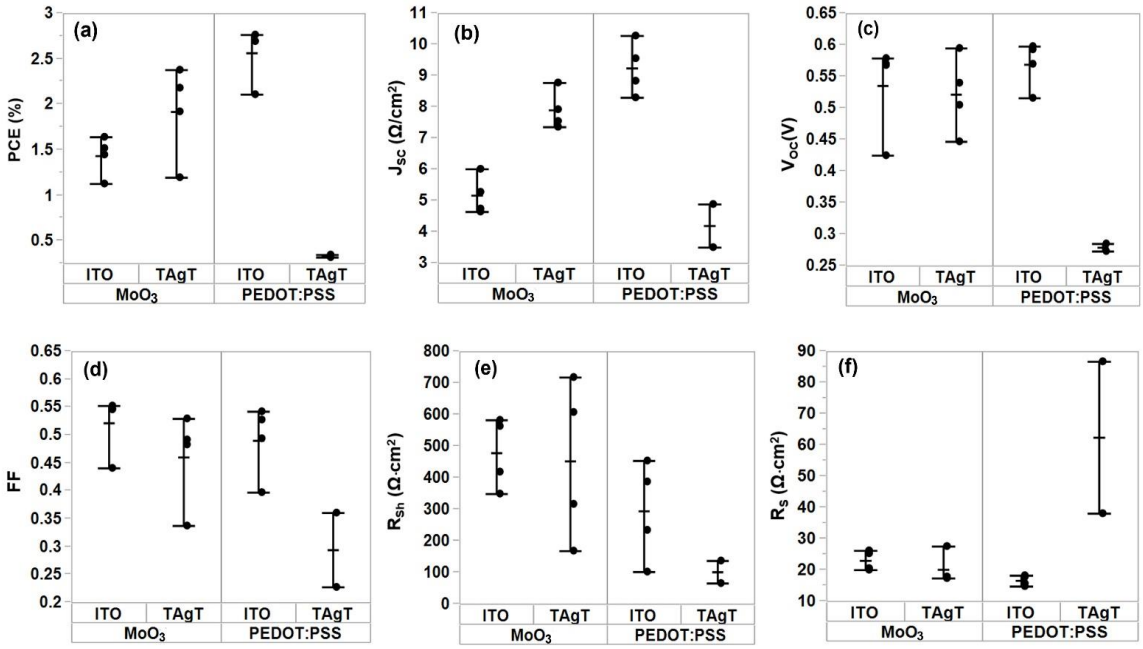

Figure 6.1 The variability charts for device parameters of anode/HTL/P_3HT:PCBM/LiF-Al with ITO and TAgT as anodes and MoO_3 and PEDOT:PSS as HTLs: (a) PCE; (b) J_{sc}; (c) V_{oc}; (d) Fill Factor (FF); (e) shunt resistance (R_{sh}); (f) R_s. The top and bottom line indicates the highest and lowest values, respectively. The centered line indicates the mean value.

Table 6.1 Device parameters of Anode/HTL/P_3HT:PCBM/LiF-Al solar cells with ITO and TiO2/Ag/TiO2 as the anode, and MoO_3 and PEDOT:PSS as HTLs

Anode	HTL	V_{oc} (V)	J_{sc} (mA/cm^2)	FF (%)	PEC (%)	R_s (Ωcm^2)	R_{sh} (Ωcm^2)
ITO	PEDOT:PSS	0.57	9.25	0.49	2.56	16.64	294.65
TiO_2/Ag/TiO_2	PEDOT:PSS	0.28	5.17	0.29	1.91	62.44	101.57
ITO	MoO3	0.53	7.90	0.52	1.43	23.02	478.7
TiO_2/Ag/TiO_2	MoO3	0.52	4.20	0.46	0.33	20.15	452.98

For comparison of anodes, the performance of ITO based OSCs are studied. ITO+PEDOT:PSS device shows the best overall performance than other three devices in terms of power conversion efficiency (PCE), short circuit current density (J_{sc}), open circuit voltage (V_{oc}) and R_s. However, using MoO_3 on ITO anode leads to reduced PCE,

Jsc, and increased R_s, when comparing to ITO+PEDOT:PSS device. Contradictory to lots of reports that MoO_3 is a good HTL replacement of PEDOT:PSS and gives comparable and even higher PCE [70, 75, 142, 148], our finding shows the ITO based OSC has a lower PCE when PEDOT:PSS is replaced by MoO_3. Detailed explanation will be given later. More importantly, PCE of ITO+MoO_3 device is lower than that of the TAgT+MoO_3 device, and both of their PCE are lower than that of ITO+PEDOT:PSS device. This indicates an appropriate hole transfer layer in regard to different electrode is important.

According to Figure 6.1 and Table 6.1, V_{oc} for ITO+PEDOT:PSS, TAgT+MoO_3, ITO+MoO_3 devices are close to each other and the maximum difference between their V_{oc} is only 9%. Moreover, devices with high J_{sc}, and low R_s always show high PCE; therefore, their PCE are dominantly determined by their J_{sc}. Hence, J_{sc} can be affected by several factors, including R_s, active layer thickness, and light absorption efficiency [65, 76]. All these factors can be impacted by HTL and anode, since electrical resistance of anode and contact at anode/HTL and HTL/active layer interfaces affect R_s [71, 75]. The wettability of HTL layer affects the thickness of spin-coated active layer. The transmittance of anode affects the light input into the device and the resulting light absorption efficiency in the active layer [71].

6.3.2 HTL Effect on R_s and J_{sc}

It is known that R_s has a major impact on J_{sc}. According to the average R_s in Table I, devices with low R_s always shows high J_{sc}. The interface layer between electrode and active layer, like HTL, has major influence on the R_s, since HTL can adjust the band alignment between electrode and active layer, and reduce their contact barriers [71]. The

work function of ITO and TAgT on glass measured by Kelvin Probe are 4.3 eV and 4.9 eV, respectively. MoO_3 is reported as a n-type semiconductor and its work function is 5.4 – 6.9 eV [142-144, 149-151], which is higher than the work function of both ITO and TAgT electrodes. As a result, Ohmic contact is expected at ITO/MoO_3 and TAgT/MoO_3 interfaces. The sheet resistances of anode/HTL are Table II, which can be an implication of the contact between HTL and anode. First of all, the anode/MoO_3 films have almost the same R_s as the anodes. This indicates 14 nm MoO_3 on ITO and TAgT barely impacts the resistance of ITO and TAgT, and ohmic contacts are formed at ITO/MoO_3 and TAgT/MoO_3 interfaces. Due to the low sheet resistance of TAgT anode itself, the TAgT/MoO_3 film has a lower sheet resistance than ITO/MoO_3 film, and this is consist with R_s of their corresponding OSC. Considering TAgT+MoO_3 and ITO+MoO_3 devices has the same MoO_3 HTL layer in contact with active layer, the contact barrier between HTL and active layer should be similar in those two devices. As a result, the lower R_s in TAgT/MoO_3 device is mainly due to the low sheet resistance TAgT anode, and contributes to its higher J_{sc}, in comparison of ITO/MoO3 devices.

Table 6.2 The sheet resistance for ITO, TAgT, and anode/HTL films.

Anode	HTL	Sheet resistance (Ω/sq)
ITO	N/A	20.3
TiO_2/Ag/TiO_2	N/A	4.4
ITO	PEDOT:PSS	20.7
TiO_2/Ag/TiO_2	PEDOT:PSS	24475
ITO	MoO_3	19.1
TiO_2/Ag/TiO_2	MoO_3	4.2

With the PEDOT:PSS as the HTL, the extremely high sheet resistance of TAgT/PEDOT:PSS confirms that attacking of PEDOT:PSS to TAgT anode. The sheet

resistance of ITO/PEDOT:PSS film is same as the individual ITO film, but is higher than the sheet resistance of TAgT/MoO_3. However, the R_s of ITO+PEDOT:PSS device is lower than the R_s of TAgT+ MoO_3 device. The lower R_s in ITO/PEDOT:PSS device is most likely attributed to the better contact at PEDOT:PSS/active layer interface than that at MoO_3/active layer interface. It is known that the work function of PEDOT:PSS is between ITO's work function and HOMO of P_3HT [152], as a result, it can adjust the energetic barrier between active layer and the electrode, and enables a sufficient hole extraction [70]. On the other hand, due to the high work function of MoO3, it is believed that the band bending of HOMO at MoO_3/organic interface enables the hole extraction from HOMO to the electrode [142-145]. However, it is reported that as-deposited MoO3 is not efficient to achieve favorable energy alignment and enhance the hole extraction due to the limited amount of intrinsic oxygen vacancy defects [144]. It is believed that generating oxygen vacancies in MoO_3 can enhance the hole extraction from the donor HOMO to electrode [144]. The more oxygen vacancy defects in MoO_3 can extend and broaden the energy range of defect states near Fermi level, as a result, the energy alignment between the defect states in MoO_3 and the HOMO of P_3HT become favorable for the hole injection from P3HT to defect states and being collected by the electrode [144, 145]. However the generation of oxygen vacancy gap states in MoO_3 film need annealing, and the intrinsic defects in as-deposited MoO_3 is not sufficient [144]. Similarly, the as-deposited MoO_3 in our case, due to the lack of oxygen vacancy defect generation, cannot offer a favorable energy alignment and sufficient hole extraction as the PEDOT:PSS does. This results in relatively higher R_s in the MoO3 based devices. The better contact

at PEDOT:PSS/active layer interface enables the eventually lower R_s in ITO+PEDOT:PSS device even though ITO anode has a higher sheet resistance.

6.3.3 HTL Wettability Effect on Active Layer Thickness

It is reported that increasing the active layer thickness is possible to enhance J_{sc} value, because thicker polymer film enables more light absorption [62, 65]. However this enhancement will be terminated or even become worse when the thickness is beyond a certain value [62, 65]. This is because the photo-generated electrons and holes cannot reach the electrode before recombination if the active layer is too thick [62, 65]. The typical thickness of active layer is 100-300 nm [62, 65]. The different underlying HTL might result in different active layer thickness, which in turn affects J_{sc}. As a means to validate this, an active layer is spin-coated onto three different substrates (ITO/PEDOT:PSS, ITO/MoO_3, TAgT/MoO_3) using the same process conditions and each active layer thickness measured using profilometer. The variability chart of the active layer thickness are shown in Figure 6.2. The active layers spin-coated on different HTLs do have different thickness. The active layers spin-coated on MoO_3 HTL shows the same average thickness (205 nm) regardless of anode. As a result, active layer thickness has nothing to do with the higher J_{sc} in TAgT+MoO_3 device than that of ITO+MoO_3 device. It is noticed that the average active layer thickness is higher (282 nm) when it is spin-coated on ITO/PEDOT:PSS. This thicker active layer on ITO/PEDOT:PSS probably contributes to the higher J_{sc} of ITO+PEDOT:PSS device, in comparison with ITO+MoO_3 and TAgT+MoO_3 devices.

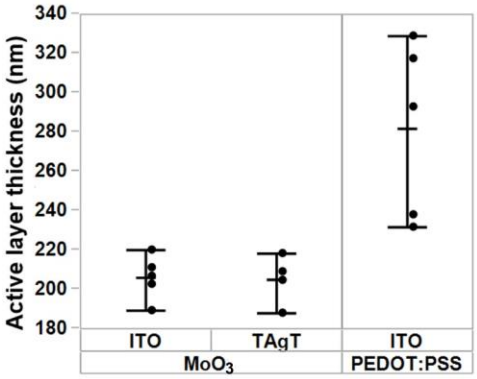

Figure 6.2 The variability chart for active layer thickness on ITO/PEDOT:PSS, ITO/MoO_3 and TAgT/MoO_3 films.

To further validate that statement, we intentionally spin-coated active layers with similar thickness on ITO/PEDOT:PSS, ITO/MoO_3 and TAgT/MoO_3 substrates, respectively. All the active layers were spin-coated using 600 rpm for 5 min. For comparison, the control sample's active layer is spin-coated on ITO/PEDOT:PSS using original recipe (at 600 rpm for 1 min). The active layer thickness and device parameters of each OSC are listed in Table 6.3. When the active layer thickness of the ITO+PEDOT:PSS device is reduced after 5 min spin coating its PCE and J_{sc} are significantly reduced in comparison with 1 min spin-coated active layer. This indicates that the active layer thickness does play an important role in PCE and J_{sc}, and thicker active layer in ITO+PEDOT:PSS device contributes to higher PCE. With the similar active layer thickness in ITO+PEDOT:PSS, TAgT+MoO_3 and ITO+MoO_3 devices, PCE and J_{sc} of the ITO+PEDOT:PSS device are even smaller than those of TAgT+MoO_3 device, but larger than those of ITO+MoO_3 device. This indicates that the combination of TAgT anode and MoO_3 HLT is promising and the PCE can be potentially further improved if a uniform and thicker active layer (240 ~ 300 nm) can be achieved.

Table 6. 3 Device parameters and active layer thickness for anode/HTL/P_3HT:PCBM/LiF-Al solar cells with ITO and TiO_2/Ag/TiO_2 as the anode and MoO_3 and PEDOT:PSS as HTLs

Anode	HTL	Spin Coating duration (min)	Active layer thickness (nm)	V_{oc} (V)	J_{sc} (mA/cm2)	FF (%)	PCE (%)	R_{series} ($\Omega \cdot cm^2$)	R_{sh} ($\Omega \cdot cm^2$)
ITO	1	243	0.58	7.81	0.56	2.53	2.53	16.28	329.95
ITO	5	193	0.51	5.59	0.42	0.42	1.21	24.15	196.17
ITO	5	198	0.55	3.98	0.54	0.54	1.18	19.40	560.89
TAgT	5	191	0.55	7.37	0.46	0.46	1.84	23.18	352.63

To find out the reason for active layer thickness dependence on the HTL, the roughness and wettability of two different HTLs are further studied. The polymer blends (P_3HT:PCBM) contact angle measurement is done on ITO/PEDOT:PSS, ITO/MoO_3, TAgT/MoO_3 films and their average contact angles are 12.3^o, 16.2^o and 15.7^o, respectively. First of all, all the films have good wettability for polymer blends. PEDOT:PSS has a slightly better wettability than MoO_3. We believe this better wettability of PEDOT:PSS results in the thicker spin-coated active layer on ITO/PEDOT:PSS substrate as mentioned in Table 6.3. ITO/MoO_3 and TAgT/MoO_3 films have the similar wettability since they are using the same HTL. The similar wettability also implies that the underlying anodes barely have any effect on the wettability of MoO_3. The AFM images and cross-section profiles are shown in Figure 6.3. The RMS roughness of ITO/PEDOT:PSS, ITO/MoO_3, TAgT/MoO_3 films are 1.45 nm, 0.56 nm and 1.55 nm, respectively. The ITO/PEDOT:PSS and TAgT/MoO_3 has the similar roughness, and ITO/MoO_3 has the smallest roughness. This indicates the roughness of those films does not correlate to their wettability in this case.

6.3.4 Anode Effect on Light Absorption in The Device

As discussed in previous section, TAgT+MoO_3 devices shows higher J_{sc} than ITO+MoO_3 device. We ruled out the effect of active layer thickness on J_{sc} in those two structures, and demonstrated the low R_s of TAgT+MoO_3 device contributes to its high J_{sc}. In this section, the impact of anodes' transmittance on light absorption of the devices and J_{sc} are studied. In our previous study, TAgT has lower light transmittance (89%) than ITO (96%) [139], and their different transmittance can potentially impact the amount of light absorbed by devices. The absorption of anode/MoO_3/P_3HT:PCBM/LiF-Al were measured by UV-Vis to investigate the effect of anodes on light absorption of OSC.

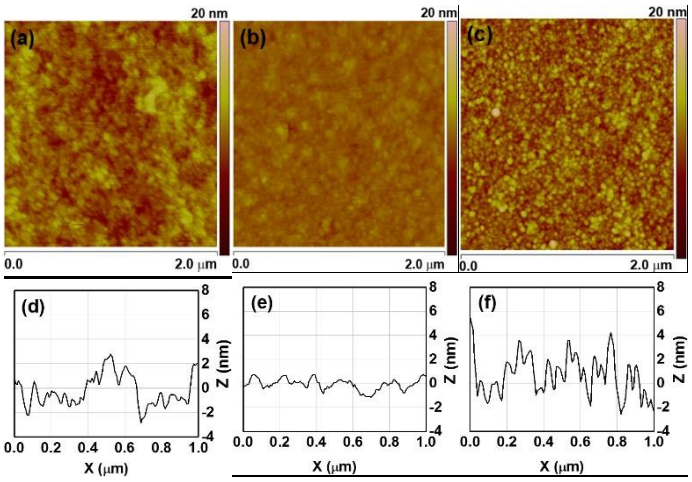

Figure 6.3 AFM images (2 μm × 2 μm scan) for (a) ITO/PEDOT:PSS film, (b) ITO/MoO_3 film, and (c) TAgT/MoO_3 film and cross-section profiles for (d) ITO/PEDOT:PSS film, (e) ITO/MoO_3 film, and (f) TAgT/MoO_3 film

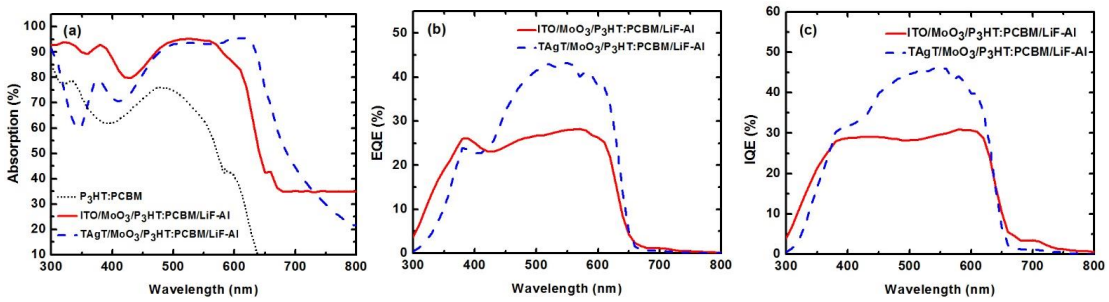

Figure 6. 4 Absorption spectrum for absorption spectrum for anode/MoO_3/P_3HT:PCBM/LiF-Al and solely P_3HT:PCBM/glass, (b) EQE of anode/MoO_3/P_3HT:PCBM/LiF-Al, (c) IQE of anode/MoO_3/P_3HT:PCBM/LiF-Al

Figure 6.4 (a) shows the absorption of Anode/MoO_3/P_3HT:PCBM/LiF-Al and solely P_3HT:PCBM/glass. The light mainly absorbed by P_3HT:PCBM layer is in the wavelength range of 400 nm to 600 nm. The absorption spectrum of ITO+MoO_3 device and TAgT+MoO_3 device in this wavelength range is quite similar, and their average absorption in this wavelength range are 89% and 87%, respectively, which only is slightly different. This indicates that the different light transmittance of those two anodes does not significantly impact the amount of light being absorbed by the device. Since the two devices has the similar light absorption, their different J_{sc} cannot be attributed to the different light transmittance of anodes, but is related to the extent of quantum efficiency of absorbed photon in the devices. The internal quantum efficiency (IQE) indicates the how efficiently the absorbed light are converted to the electricity and collected by the electrodes. IQE can be calculated by measuring external internal quantum efficiency (EQE) and light absorption spectrum. The IQE for ITO+MoO_3 and TAgT+MoO_3 devices are compared in Figure 6.4 (c). The lower EQE and IQE in ITO+MoO_3 devices indicate its inefficient photo-carrier generation and inefficient collection of photo-carriers. This give rise to its lower J_{sc} than that of TAgT+MoO_3 device. In a word, the transmittance

difference in ITO and TAgT anodes are not responsible for their different J_{sc}, but the higher photon generation and collection efficiency of TAgT+MoO_3 device result in its higher J_{sc} than ITO+MoO_3 device.

6.4 Conclusion

TAgT as an alternative of ITO, is successfully incorporated into OSCs. The compatibility of two different HTLs (PEDOT:PSS and MoO_3) with TAgT anode are studied. To compare the performance of TAgT anode with ITO anode, ITO based OSCs using PEDOT:PSS and MoO_3 as HTLs are fabricated at the same time as control samples. When using PEDOT:PSS as HTL, PCE of TAgT based OSC is worse than that of ITO based OSC. This is because TAgT is very vulnerable to PEDOT:PSS's attack, which results in an extremely high sheet resistance in TAgT after PEDOT:PSS deposition. However, when MoO_3 is employed as HTL, MoO_3 form ohmic contact with both ITO and TAgT anodes. TAgT+MoO_3 device has better performance than ITO+MoO_3 device. This is attributed to lower sheet resistance of TAgT anode than that of ITO anode. The different light transmittance of the two anodes does not have an impact on the device's light absorption and PCE. As a result, MoO_3 as HTL is more compatible with TAgT because it does not attack the metal oxide in TAgT and forms ohmic contact with TAgT.

It is noticed that the average PCE of ITO/PEDOT:PSS/P_3HT:PCBM/LiF-Al is PCE is 2.65%, better than the average PCE (1.91%) of TAgT/MoO_3/P3HT:PCBM/LiF-Al. This is due to better hole extraction at PEDOT:PSS/active layer interface, in comparison with MoO_3/active layer interface. In addition, the better wettability of

PEDOT:PSS surface and the resulting thicker active layer in ITO+PEDOT:PSS device contributes to the better performance in ITO+PEDOT:PSS.

7. THE ELECTROMIGRATION RELIABILITY CHARACTERIZATION OF PRINTED AG STRUCTURE FOR PHOTOVOLTAIC METALLIZATION APPLICATION

7.1 Introduction

Printed microelectronics have the potential for broad application and ease of use. This has been a driving force for significant advances in the inks that are used to print conducting lines. Such advances include lower sintering temperatures and lower resistances.[153-156] For example, newer nanoparticle-based silver inks can be chemically sintered at room temperature using polyanionic compounds.[157, 158] Despite these advances, very few industries outside of the photovoltaic industry have adopted silver inks for their metallization schemes and even fewer use drop-on-demand (DOD) printed inks in real-world applications. This limited adoption of DOD printed electronics can be attributed to the limited availability of commercial-scale DOD printers capable of handling large production volumes with high resolutions and the high cost of DOD-compatible nanoparticle inks. Reactive inks are a new approach to DOD printed electronics that are easy to synthesize and that often do not require high-temperature sintering.[77, 78] Unlike traditional inks that print clusters of particles, reactive inks print chemical precursors that react to form a solid material.[80, 81] These reactions can be initiated by elevated substrate temperatures (thermally), solvent or stabilizing agent evaporation (chemically), or by some increased catalytic activity of the substrate (kinetically).[80, 82-88] Recent advances in silver,[80] copper,[81] and aluminum[84, 89] reactive inks have brought the reaction temperatures of these inks to below 180 ˚C and to even room temperature for silver-diamine based inks.[77, 90, 91] Compared to silver paste and

nanoparticle-based inks, these new reactive inks provide superior conductivities (that are close to bulk material values) at lower temperatures and significantly lower costs. Applications for reactive inks include printed electronics[80], stretchable electronics[78], photovoltaic metallization[79] and more.

The long-term performance of conducting lines that are printed with reactive Ag inks is currently unknown. This is because the most promising, low-temperature reactive ink chemistries for Ag, Cu, and Al are fairly new, with keystone publications having appeared only within the last few years [80, 81, 84, 91, 159]. As a result, the relationships among processing parameters, printed physical structure, material properties, and long-term performance have yet to be studied in detail. Of particular concern is how the porous nature of silver that is printed from a reactive silver ink impacts its properties and reliability. Electromigration and Joule heating are two phenomena that contribute to early failure in electronic devices. For a high-quality, solid material, electromigration generates voids that, due to current crowding, lead to localized Joule heating and rapid device failure.[160] The failure time of metal lines due to electromigration is typically predicted by Black's equation, which correlates the lifetime with the current density and temperature during the electromigration.[161] Since reactive inks currently print porous materials with a large volume-fraction of voids[77], these materials should experience earlier failure than conducting elements fabricated using traditional methods (DC sputter coating, evaporation, electrochemical deposition, etc.). However, no studies have been published that detail the performance reliability of these printed reactive inks under a bias (temperature or current). Initial stress tests of printed silver reactive inks showed lifetimes that were quite random and that were independent of the current density. A

deeper understanding of the relationship between morphology and failure mechanisms is needed before reactive silver inks can replace more established particle-based inks and pastes.

In this work, we have studied the failure mechanisms of silver lines that were printed using a low-temperature, self-reducing, silver-diamine based ink (RSI). These studies demonstrated that Black's equation does not suitably account for morphology-induced current crowding when predicting the lifetimes of printed silver or other porous conducting elements. Overall, a model is needed that can take into account the effects of physical structure, mass-transport, and other degradation mechanisms that can impact the lifetimes of porous or "imperfect" printed electronic devices. In this work, we demonstrate that a percolation-based model (for predicting the electromigration failure time) is suitable for predicting the increase in resistance of porous conducting lines under a current bias.

7.2 Experimental

The base silver ink (that was used for this study) was prepared following Lewis' reactive silver ink recipe.[80] All of the chemicals were used as received: silver acetate ($C_2H_3AgO_2$, anhydrous 99%, Alfa Aesar); ammonium hydroxide (NH_4OH, 28-30 wt%, ACS grade, BDH Chemicals); formic acid (CH_2O_2, ≥96%, ACS reagent grade, Sigma Aldrich); and ethanol (EtOH, C_2H_6O, 99.5 wt%, Koptec). 1.0 g of silver acetate was dissolved in 2.5 mL ammonium hydroxide. The solution was then stirred for 2 minutes on a vortex mixer to dissolve the silver acetate. Next, 0.2 mL of formic acid was added in two steps with a quick stir at the end of each step. The ink was then allowed to sit for 12

hours in the dark at room temperature before being filtered through a 450 nm nylon filter. Following this, the ink was stored at 4 ˚C (refrigerator temperature) until it was used.

A mixture of 0.5 M tin (II) chloride solution in DI water mixed 1:1 by volume with 0.5 M HCl was used as a sensitizing adhesion promoter [85] to keep the silver samples from peeling off from the glass substrate . The substrates were dipped in this solution for 300 seconds and dried using N_2. Silver reactive ink lines and contact pads were printed using a MicroFab Jetlab II micro-dispensing inkjet printer. Drop volume, velocity, and quality were observed using a horizontal camera and strobe light. The Jetlab II was equipped with an MJ-ATP-01 piezoelectric-driven printer head with a 60 μm orifice coated with a diamond-like coating to reduce wetting. The mean measured droplet size was 40 μm when printed with rise and echo driving voltages of ±25 V and dwell and echo times of 5 μs and 5 μs, respectively.

Single-line test structures were printed using 1:1 EtOH:Ag ink on the glass substrates, at 78 ºC. Each of the printed lines had a length of 5 mm with a pitch of 25 μm between droplets and a measured droplet diameter of 100 μm. A Dektak XT stylus (12.5 μm stylus tip diameter) profilometer was used to collect cross-section profiles across each sample. The cross-section area of each sample was calculated by integrating the area under the measured profile.

The structures were then tested for reliability on a probe station (MC Systems Inc. Model 8832) equipped with a temperature-controlled hot stage. The samples were tested at an elevated temperature of 94 ºC to accelerate the failure process. Since early failure modes occurred at the interface between the probe and the contact pad instead of at the

Ag line, conductive silver paint (Colloidal silver liquid, Ted Pella Inc.) was applied on the contact pads in order to increase the contact surface area and to decrease the contact resistance between the probe and the contact pads to avoid the failure at their interface. The samples were tested using two probes in contact with opposite pads. A constant current was applied across the probes using an Agilent DC power supply (N5752A) and the voltage drop between the probes was measured every 1 second using a Keysight digital multimeter (34461A) until an open occurred in the line. Several different current values were applied to study the failures under different current stresses.

7.3 Results and Discussion

Typically, the failure time of a metal line can be predicted by using Black's equation: [161]

$$t_f = A_B J^{-n} \exp\left(-\frac{E_a}{k_B T}\right) \tag{7.1}$$

where A_B is a constant, J is the current density in A/cm^2, n is the current-density exponent, E_a is the activation energy in eV, k_B is Boltzmann's constant and T is the substrate temperature in Kelvin. From Black's equation, n can be extracted by fixing the test temperature and varying the current density.[162, 163]

The printed Ag line has a porous microstructure. A representative cross-section secondary electron microscopy (SEM) image of an as-printed Ag line is shown in Figure. 7.1(a). The micrograph shows that the printed Ag film is porous and not solid. Due to the porous microstructure, only the Ag component (in the printed line) carries the current. As a result, the actual current-carrying cross-section area is equal to the cross-section area of

Ag (A_{Ag}) if the pores are taken out from the printed Ag sample and the sample is 100% dense (0% porosity) as a result. A_{Ag} is calculated by dividing the volume of silver used in each printed Ag line by the line length. Each Ag line was printed using the same known amount of silver. Therefore, A_{Ag} is 152 μm^2 and it has the same value for all of the samples (the calculation of A_{Ag} is shown in supporting information). Next, the current density (J) is obtained by dividing the current (I) by A_{Ag} (to take into the account of current-carrying cross-section area). Six samples were tested using the same temperature but different current densities, until they failed. Their failure times (t_f) are plotted on a log-log scale, as function of current density (J), as shown in Figure 1(b). For this study, the failure time is defined as the time that Ag line breaks. According to Eq. (7.1), t_f vs. J should be a linear function on the log-log plot and the current exponent n can be estimated by calculating the slope. However, it is evident from Figure 7.1(a) that the experimental results do not fall on a straight line as would be predicted by Black's equation.

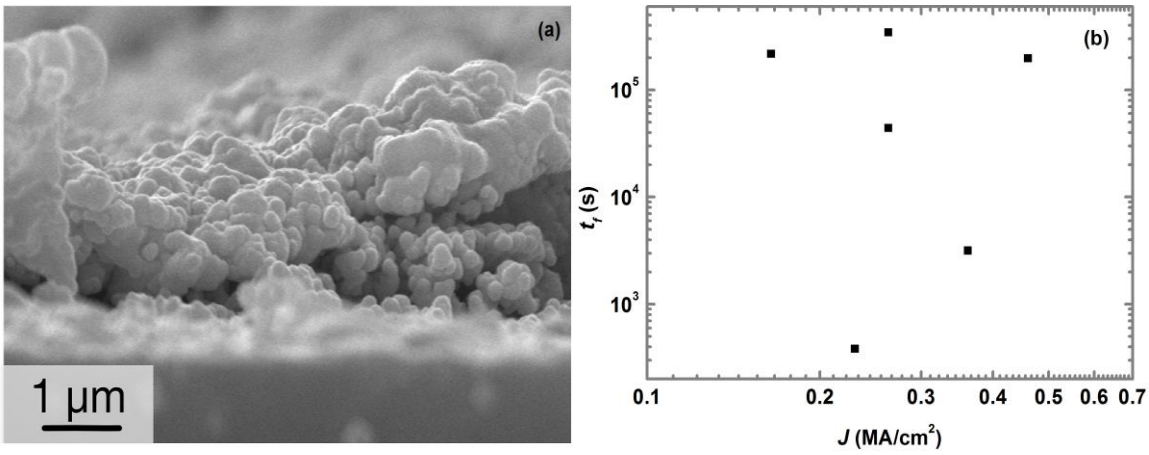

Figure 7.1 (a) A cross-section SEM image of an as-imprinted Ag line; (b) Log t_f as a function of Log J in printed Ag samples. Note that the data do not lie on a straight line as would be predicted by Black's equation. This indicates that

Black's equation cannot be applied to materials where the actual current density is not well known.

We suspect that the erratic lifetimes of the RSI printed Ag lines is likely due to the porous microstructure of the lines, and that Black's equation cannot be used for these material systems because the equation assumes a solid cross-section for calculating the current density. This assumption breaks down for porous conductors because it does not account for current crowding in such porous materials.[164-166] With this in mind, it is clear that failure models that account for porosity and morphology must be used when working with porous printed conductors.

Percolation theory has been used to study the conductivity of carbon nanotube thin film networks [167]. Similarly, to take into the account of the porosity of our printed sample, the conduction of this porous structure can be described by a standard (unbiased) percolation model.[168, 169] The line can be viewed as a random network of insulators (voids) and conductive resistors (silver).[168, 169] All of the resistors are assumed to have the same resistance, in order to simplify the model. Based on percolation theory, the resistivity (ρ) is a function of the void fraction, and is given by the following equation[170] :

$$\rho = \rho_0 (1 - f_V)^{-m} \tag{7.2}$$

where ρ_0 is the pre-factor and is proportional to the metal's bulk resistivity, and m is the percolation coefficient. The resistivity (ρ) of a printed Ag line is obtained from the measured resistance, the measured area and the line length. f_V is the fraction of voids in the printed sample.

Our measurements show that the measured cross-section areas are different from sample-to-sample, even though the lines were printed using the same amount of Ag ink.

This is an indication of the variation in porosity from sample-to-sample and even within the same sample. The porosity can be estimated by calculating the fraction of the voids in the sample (f_V):

$$f_V = 1 - \frac{V_{Ag}}{V_{measured}} = 1 - \frac{A_{Ag} \cdot l}{A_{measured} \cdot l} = 1 - \frac{A_{Ag}}{A_{measured}} \tag{7.3}$$

where V_{Ag} and A_{Ag} are the volume and cross-section area if the printed Ag sample was 100% dense (0% porosity), $V_{meaured}$ and $A_{measured}$ are the measured volume and measured cross-section area of the printed Ag sample as determined by profilometry, and l is the length of the printed Ag sample.

The ρ and f_V of several printed Ag samples were determined, to validate the percolation model on the printed Ag sample. The resulting ρ is plotted as a function of f_V and can be fitted by Eq. 7.2, as shown in Figure 7.2. The values of ρ_o and m were calculated to be 1.51×10^{-5} Ω-cm, and 0.91, respectively. Using a least-squares model, the Adjusted R-square of fit was 0.97. Based on this fit, we conclude that the conduction pathways of the printed reactive inks can be described by the standard percolation model.

Given that the conduction occurs via a percolation process, one would expect that the failure should also occur by such a process. When failure occurs by the standard percolative model, the damage would be uniform and dependent on a single test parameter.[168, 169] In the case of electromigration, the failure occurs due to void formation and coalescence during the current stressing.[160] The percolative model for predicting the electromigration failure has to be biased given that the failure is nonhomogeneous, and it depends on the position and time.[168, 169] Monte-Carlo simulations have been used to

describe the evolution of resistance for biased percolation.[168, 169] The scaling of the resistance as a function of time ($R(t)$) is given by:

$$R(t) = \gamma R_0 \left(1 - \frac{t}{t_f}\right)^{-u} \tag{7.4}$$

where R_0 is the initial resistance, γ is a statistical variation factor which does not have physical meaning but is due to statistical variation during data collection, t is time under bias, t_f is the failure time and μ is the percolation parameter. μ is dependent on the current density and the temperature applied on the sample [168, 169].

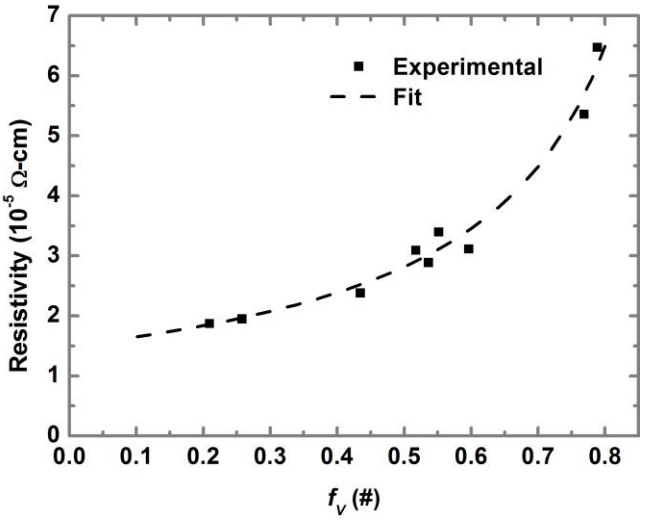

Figure 7.2 ρ as a function of void fraction (f_V) from the printed Ag samples before EM testing. Experimental fit of $\rho = \rho_0(1-f_V)^{-m}$ with ρ_0 = 1.5×10-5 Ω-cm m = 0.91; the Adjusted R-square of fit was 0.97 using a least square fit method to fit ln*R* vs. ln$(1- f_V)$ in order to fit a linear line. These results show that the percolation model adequately models the conduction pathways for these materials.

Two printed samples were tested under current densities of 2.63 MA/cm^2 and 3.62 MA/cm^2. Both samples were tested at 94 ^{o}C until an open-circuit was measured (*i.e.*, failure). Their resistance as a function of time is plotted in Figure. 3. Given that their initial resistance and failure times are known, the γ and t_f can be extracted by fitting the *R*

vs. *t* curves using Eq. (7.4). A typical fit using Eq. (7.4) is shown in Figure 7.3. The extracted results and detailed parameters from the samples are listed in Table I. The results show that μ has the same value (of 0.012) when the samples have the same current density (of 2.63 MA/cm^2). However, μ had a value of 0.048 when the sample was tested under a different current (of 3.62 MA/cm^2). This result is consistent with the fact that μ depends on the current density and temperature in the percolation model. The deviation of *R* from the fitting model between 2000-2500 sec is probably due to the evolution of the voids/pores in the printed Ag line. It has been proposed [171] that the resistance change depends on the void shape and the change in void volume, $\Delta R/R = f\,\Delta V/V$ [171].The volumes and shapes of the local pores/voids in the porous Ag line are more likely to change due to current-induced mass transportation. This will cause a deviation of the R from the model, since the model does not take into account the effects of changes in the local voids.

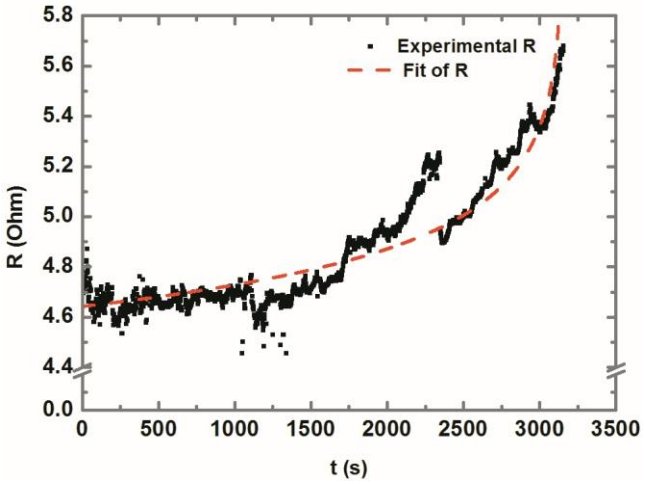

Figure 7.3 Resistance of printed Ag sample as a function of time for a current density of 3.62 MA/cm^2.

Table 7.1 The current density (J), void fraction (f_V), initial resistance (R_o), failure time (t_f) and parameters (γ and μ) extracted by fitting Eq (7.4)

Sample ID	J (MA/cm^2)	f_V	R_o	t_f (s)	γ	μ
a	3.62	0.926	4.75	3159	0.97	0.048
b	2.63	0.960	4.13	43994	0.96	0.012
c	2.63	0.955	5.00	342536	0.93	0.012

The percolative model can be further modified to incorporate the void fraction. In the percolative model, R_0, which is the initial resistance of the sample, can be related to the void fraction using Eq. 7.2. This can be be expressed as:

$$R_0 = \frac{\rho \cdot l}{A_{measured}} = \frac{\rho_0 (1 - f_V)^{1-m} \cdot l}{A_{Ag}} \tag{7.5}$$

Hence, the void fraction can be incorporated into Eq. 7.4, by using Eq. 7.5:

$$R(t) = \gamma \cdot \frac{\rho_0 (1 - f_V)^{1-m} \cdot l}{A_{Ag}} \left(1 - \frac{t}{t_f}\right)^{-u} \tag{7.6}$$

Inspection of Eq. 7.6 shows that the porosity has a direct impact on the time dependent resistance during biasing at high current levels. In addition, the EM failure-time and the reliability of printed lines can be predicted using percolation theory. Future work will focus on the use of Eq. 7.6 to experimentally demonstrate that for similar structures (i.e., similar metals and with similar porosity) that are undergoing EM degradation, the exponents m and n can be accurately extracted from a small population of samples.

7.4 Conclusion

Ag metallization structures were printed by using reactive Ag ink. The reliability of the printed single-line Ag structure were tested through EM. The test results were first

analyzed using Black's equation. However, J vs. t did not follow Black's equation. SEM analysis showed that the printed Ag lines are porous. These results indicated that it is inappropriate to apply Black's equation to porous structures. In contrast, the conduction in the porous Ag line was successfully described by using percolation theory. Therefore, we expected that the percolative model should be able to describe the failures of the porous printed Ag lines. Our analysis shows that R vs. t can be fitted well by the percolative model. A dependence of μ on current density is observed in the experiment. This further supports the hypothesis that the percolative model is valid for describing failures of porous printed Ag lines. A model that links the physical structure and mass-transport to the lifetime is obtained by modifying the percolative model.

8. FUTURE WORK

TAgT has been proved to be a beneficial anode to conventional P3HT:PCBM BHJ solar cell, and we are interested in applying it to the inverted BHJ solar cells. In inverted BHJ OSC, the high work function metal is used as the top anode and transparent conductive film is used as the bottom cathode[172]. The advantage of this structure is the high work function metal has less chance to be contaminated, in comparison to the low work function metal cathode in conventional OSC[172]. Moreover, due to the inherent vertical phase separation in the polymer active layer, the acceptor tends to segregate to the bottom. In conventional BHJ OSC, accepter tends to in contact with the bottom anode which cause the electrons lose their path to cathode and recombine with holes in the anode. However, inverted structure solve this problem by placing the cathode at the bottom so that acceptor tends to in contact with cathode. The electron transfer layer in inverted BHJ OSC is typically TiO_2. If TAgT is used as the cathode in inverted BHJ OSC, the TiO2 layer in the electrode can also act as the electron transfer layer, this would reduce the fabrication steps and might also improve the light input into the organic solar cell.

REFERENCE

1. Alford, T. L.; Feldman, L. C.; Mayer, J. W., *Fundamentals of nanoscale film analysis*. Springer Science & Business Media: 2007.

2. Schroder, D. K., *Semiconductor material and device characterization*. John Wiley & Sons: 2006.

3. Plummer, J. D., *Silicon VLSI technology: fundamentals, practice, and modeling*. Pearson Education India: 2000.

4. Mayer, J.; Lau, S., Electronic Materials Science: For Interconnection Circuits in Si and GaAs. Macmillan: New York: 1990; pp 222-242.

5. Mayer, J. W.; Lau, S. S., *Electronic materials science: for integrated circuits in Si and GaAs*. Prentice Hall: 1990.

6. Mahajan, S.; SreeHarsha, K., *Principles of growth and processing of semiconductors*. McGraw-Hill Science, Engineering & Mathematics: 1999.

7. Pelaz, L.; Marqués, L. A.; Barbolla, J., Ion-beam-induced amorphization and recrystallization in silicon. *Journal of applied physics* **2004,** *96* (11), 5947-5976.

8. Dhar, A.; Alford, T. L., Optimization of Nb2O5/Ag/Nb2O5 multilayers as transparent composite electrode on flexible substrate with high figure of merit. *Journal of Applied Physics* **2012,** *112* (10), 103113.

9. Jeong, J. A.; Park, Y. S.; Kim, H. K., Comparison of electrical, optical, structural, and interface properties of IZO-Ag-IZO and IZO-Au-IZO multilayer electrodes for organic photovoltaics. *Journal of Applied Physics* **2010,** *107* (2).

10. Vemuri, R. N.; Gadre, M. J.; Theodore, N. D.; Chen, W.; Lau, S. S.; Alford, T. L., Susceptor assisted microwave annealing for recrystallization and dopant activation of arsenic-implanted silicon. *Journal of Applied Physics* **2011,** *110* (3), 034907.

11. Konno, T. J.; Sinclair, R., Metal-contact-induced crystallization of semiconductors. *Materials Science and Engineering: A* **1994,** *179*, 426-432.

12. Hultman, L.; Robertsson, A.; Hentzell, H.; Engström, I.; Psaras, P., Crystallization of amorphous silicon during thin-film gold reaction. *Journal of applied physics* **1987,** *62* (9), 3647-3655.

13. Seidel, T.; Lischner, D.; Pai, C.; Knoell, R.; Maher, D.; Jacobson, D., A review of rapid thermal annealing (RTA) of B, BF 2 and As ions implanted into silicon. *Nuclear Instruments and Methods in Physics Research Section B: Beam Interactions with Materials and Atoms* **1985,** *7*, 251-260.

14. Clark, D. E.; Sutton, W. H., Microwave processing of materials. *Annual Review of Materials Science* **1996,** *26* (1), 299-331.

15. Hummel, R. E., *Electronic properties of materials*. Springer Science & Business Media: 2011.

16. Meredith, R. J., *Engineers' handbook of industrial microwave heating*. IET: 1998.

17. Metaxas, A. a.; Meredith, R. J., *Industrial microwave heating*. IET: 1983.

18. Thostenson, E.; Chou, T.-W., Microwave processing: fundamentals and applications. *Composites Part A: Applied Science and Manufacturing* **1999,** *30* (9), 1055-1071.

19. Grant, E.; Halstead, B. J., Dielectric parameters relevant to microwave dielectric heating. *Chemical Society Reviews* **1998,** *27* (3), 213-224.

20. Nelson, S. O.; Trabelsi, S., Factors influencing the dielectric properties of agricultural and food products. *Journal of Microwave Power and Electromagnetic Energy* **2012,** *46* (2), 93-107.

21. Fong, S.; Wang, C.; Chang, T.; Chin, T., Crystallization of amorphous Si film by microwave annealing with SiC susceptors. *Applied Physics Letters* **2009,** *94* (10), 102104.

22. Vemuri, R. N.; Gadre, M. J.; Theodore, N.; Chen, W.; Lau, S.; Alford, T. L., Susceptor assisted microwave annealing for recrystallization and dopant activation of arsenic-implanted silicon. *Journal of Applied Physics* **2011,** *110* (3), 034907.

23. Poate, J., *Laser annealing of semiconductors*. Elsevier: 1982.

24. Baeri, P.; Campisano, S.; Foti, G.; Rimini, E., A melting model for pulsing-laser annealing of implanted semiconductors. *Journal of Applied Physics* **1979,** *50* (2), 788-797.

25. Baeri, P.; Campisano, S.; Foti, G.; Rimini, E., Arsenic diffusion in silicon melted by high-power nanosecond laser pulsing. *Applied Physics Letters* **1978,** *33* (2), 137-140.

26. Venkatesan, T.; Golovchenko, J.; Poate, J.; Cowan, P.; Celler, G., Dose dependence in the laser annealing of arsenic-implanted silicon. *Applied Physics Letters* **1978,** *33* (5), 429-431.

27. Cristiano, F.; Qiu, Y.; Bedel-Pereira, E.; Huet, K.; Mazzamuto, F.; Fisicaro, G.; La Magna, A.; Quillec, M.; Cherkashin, N.; Wang, H. In *Extended defects in ion-implanted si during nanosecond laser annealing*, Junction Technology (IWJT), 2014 International Workshop on, IEEE: 2014; pp 1-6.

28. Gat, A.; Gibbons, J.; Magee, T.; Peng, J.; Deline, V.; Williams, P.; Evans Jr, C., Physical and electrical properties of laser-annealed ion-implanted silicon. *Applied Physics Letters* **1978,** *32* (5), 276-278.

29. Krynicki, J.; Suski, J.; Ugniewski, S.; Grötzschel, R.; Klabes, R.; Kreissig, U.; Rüdiger, J., Laser annealing of arsenic implanted silicon. *Physics Letters A* **1977,** *61* (3), 181-182.

30. White, C.; Christie, W.; Appleton, B.; Wilson, S.; Pronko, P.; Magee, C., Redistribution of dopants in ion-implanted silicon by pulsed-laser annealing. *Applied Physics Letters* **1978,** *33* (7), 662-664.

31. Sivaramakrishnan, K.; Alford, T. L., Conduction and transmission analysis in gold nanolayers embedded in zinc oxide for flexible electronics. *Applied Physics Letters* **2010,** *96* (20), 201109.

32. Dhar, A.; Alford, T. L., High quality transparent TiO2/Ag/TiO2 composite electrode films deposited on flexible substrate at room temperature by sputtering. *Apl Materials* **2013,** *1* (1), 012102.

33. Kumar, A.; Srivastava, R.; Kamalasanan, M. N.; Mehta, D. S., Enhancement of light extraction efficiency of organic light emitting diodes using nanostructured indium tin oxide. *Optics Letters* **2012,** *37* (4), 575-577.

34. El Hichou, A.; Kachouane, A.; Bubendorff, J.; Addou, M.; Ebothe, J.; Troyon, M.; Bougrine, A., Effect of substrate temperature on electrical, structural, optical and cathodoluminescent properties of In 2 O 3-Sn thin films prepared by spray pyrolysis. *Thin Solid Films* **2004,** *458* (1), 263-268.

35. Hsu, C.-M.; Lee, J.-W.; Chen, J.-S.; Huang, C.-Y.; Lin, J.-C. In *Temperature effect on the characteristics of DC magnetron sputtered ITO films*, Photonics Asia 2002, International Society for Optics and Photonics: 2002; pp 135-143.

36. Muneshwar, T.; Varma, V.; Meshram, N.; Soni, S.; Dusane, R., Development of low temperature RF magnetron sputtered ITO films on flexible substrate. *Solar Energy Materials and Solar Cells* **2010,** *94* (9), 1448-1450.

37. Lee, J. H.; Woo, K. Y.; Kim, K. H.; Kim, H. D.; Kim, T. G., ITO/Ag/ITO multilayer-based transparent conductive electrodes for ultraviolet light-emitting diodes. *Optics Letters* **2013,** *38* (23), 5055-5058.

38. Guillen, C.; Herrero, J., TCO/metal/TCO structures for energy and flexible electronics. *Thin Solid Films* **2011,** *520* (1), 1-17.

39. Cattin, L.; Morsli, M.; Dahou, F.; Abe, S. Y.; Khelil, A.; Bernede, J. C., Investigation of low resistance transparent MoO3/Ag/MoO3 multilayer and application as anode in organic solar cells. *Thin Solid Films* **2010,** *518* (16), 4560-4563.

40. Sahu, D. R.; Lin, S. Y.; Huang, J. L., ZnO/Ag/ZnO multilayer films for the application of a very low resistance transparent electrode. *Applied Surface Science* **2006,** *252* (20), 7509-7514.

41. Guillen, C.; Herrero, J., Structure, optical and electrical properties of Al:ZnO thin films deposited by DC sputtering at room temperature on glass and plastic substrates. *Physica Status Solidi a-Applications and Materials Science* **2009,** *206* (7), 1531-1536.

42. Dhar, A.; Alford, T. L. In *Optimization of IGZO/Cu/IGZO Multilayers as Transparent Composite Electrode on Flexible Substrate by Room-temperature Sputtering and Post-Deposition Anneals*, MRS Proceedings, Cambridge Univ Press: 2013; pp mrss13-1577-xx03-33.

43. Dhar, A.; Alford, T. L., Optimization of TiO2/Cu/TiO2 Multilayer as Transparent Composite Electrode (TCE) Deposited on Flexible Substrate at Room Temperature. *ECS Solid State Letters* **2014,** *3* (11), N33-N36.

44. Han, H.; Theodore, N. D.; Alford, T. L., Improved conductivity and mechanism of carrier transport in zinc oxide with embedded silver layer. *Journal of Applied Physics* **2008,** *103* (1), 013708.

45. Kim, S.; Lee, J. L., Design of dielectric/metal/dielectric transparent electrodes for flexible electronics. *Journal of Photonics for Energy* **2012,** *2*, 021215.

46. Köstlin, H.; Frank, G., Optimization of transparent heat mirrors based on a thin silver film between antireflection films. *Thin Solid Films* **1982,** *89* (3), 287-293.

47. Haacke, G., NEW FIGURE OF MERIT FOR TRANSPARENT CONDUCTORS. *Journal of Applied Physics* **1976,** *47* (9), 4086-4089.

48. Zhigal'skii, G.; Jones, B. K., *The physical properties of thin metal films*. CRC Press: 2003; Vol. 13.

49. Seal, K.; Nelson, M. A.; Ying, Z. C.; Genov, D. A.; Sarychev, A. K.; Shalaev, V. M., Growth, morphology, and optical and electrical properties of semicontinuous metallic films. *Physical Review B* **2003,** *67* (3).

50. Sennett, R. S.; Scott, G. D., The Structure of Evaporated Metal Films and Their Optical Properties. *Journal of the Optical Society of America* **1950,** *40* (4), 203-211.

51. Hecht, E.; Zajac, A., *Optics Addison-Wesley*. 1974.

52. Lecaruyer, P.; Maillart, E.; Canva, M.; Rolland, J., Generalization of the Rouard method to an absorbing thin-film stack and application to surface plasmon resonance. *Applied Optics* **2006,** *45* (33), 8419-8423.

53. Williams, W. E., Applications of interferometry. **1950**.

54. Wang, Z. B.; Helander, M. G.; Xu, X. F.; Puzzo, D. P.; Qiu, J.; Greiner, M. T.; Lu, Z. H., Optical design of organic light emitting diodes. *Journal of Applied Physics* **2011,** *109* (5), 053107.

55. Katsidis, C. C.; Siapkas, D. I., General transfer-matrix method for optical multilayer systems with coherent, partially coherent, and incoherent interference. *Applied Optics* **2002,** *41* (19), 3978-3987.

56. Centurioni, E., Generalized matrix method for calculation of internal light energy flux in mixed coherent and incoherent multilayers. *Applied Optics* **2005,** *44* (35), 7532-7539.

57. Poruba, A.; Fejfar, A.; Remes, Z.; Springer, J.; Vanecek, M.; Kocka, J.; Meier, J.; Torres, P.; Shah, A., Optical absorption and light scattering in microcrystalline silicon thin films and solar cells. *Journal of Applied Physics* **2000,** *88* (1), 148-160.

58. Beckmann, P.; Spizzichino, A., The scattering of electromagnetic waves from rough surfaces. *Norwood, MA, Artech House, Inc., 1987, 511 p.* **1987,** *1*, 80-91.

59. Potscavage Jr, W. J., Physics and engineering of organic solar cells. **2010**.

60. Research Cell Efficiency Records. http://www.nrel.gov/ncpv/.

61. Günes, S.; Neugebauer, H.; Sariciftci, N. S., Conjugated polymer-based organic solar cells. *Chemical reviews* **2007,** *107* (4), 1324-1338.

62. Hoppea, H.; Sariciftci, N. S., Organic solar cells: An overview. *J. Mater. Res* **2004,** *19* (7), 1925.

63. Coropceanu, V.; Cornil, J.; da Silva Filho, D. A.; Olivier, Y.; Silbey, R.; Brédas, J.-L., Charge transport in organic semiconductors. *Chemical reviews* **2007,** *107* (4), 926-952.

64. Lee, C.-C., *The Current Trends of Optics and Photonics*. Springer: 2014; Vol. 129.

65. Jao, M.-H.; Liao, H.-C.; Su, W.-F., Achieving a high fill factor for organic solar cells. *Journal of Materials Chemistry A* **2016,** *4* (16), 5784-5801.

66. Hoppe, H.; Sariciftci, N. S., Organic solar cells: An overview. *Journal of Materials Research* **2011,** *19* (07), 1924-1945.

67. Andreoli, E.; Liao, K. S.; Haldar, A.; Alley, N. J.; Curran, S. A., PPy:PSS as alternative to PEDOT:PSS in organic photovoltaics. *Synthetic Metals* **2013,** *185*, 71-78.

68. Das, S.; Choi, J. Y.; Alford, T. L., P3HT:PC61BM based solar cells employing solution processed copper iodide as the hole transport layer. *Solar Energy Materials and Solar Cells* **2015,** *133*, 255-259.

69. Yun, J. M.; Yeo, J. S.; Kim, J.; Jeong, H. G.; Kim, D. Y.; Noh, Y. J.; Kim, S. S.; Ku, B. C.; Na, S. I., Solution-Processable Reduced Graphene Oxide as a Novel Alternative to PEDOT:PSS Hole Transport Layers for Highly Efficient and Stable Polymer Solar Cells. *Adv. Mater.* **2011,** *23* (42), 4923-4928.

70. Steim, R.; Kogler, F. R.; Brabec, C. J., Interface materials for organic solar cells. *Journal of Materials Chemistry* **2010,** *20* (13), 2499-2512.

71. Chen, L.-M.; Xu, Z.; Hong, Z.; Yang, Y., Interface investigation and engineering–achieving high performance polymer photovoltaic devices. *Journal of Materials Chemistry* **2010,** *20* (13), 2575-2598.

72. Peumans, P.; Bulović, V.; Forrest, S. R., Efficient, high-bandwidth organic multilayer photodetectors. *Applied Physics Letters* **2000,** *76* (26), 3855.

73. Peumans, P.; Bulović, V.; Forrest, S. R., Efficient photon harvesting at high optical intensities in ultrathin organic double-heterostructure photovoltaic diodes. *Applied Physics Letters* **2000,** *76* (19), 2650.

74. Choy, W. C. H., *Organic Solar Cells: Materials and Device Physics*. Springer London: 2013.

75. Choy, W. C.; Ho, W., *Organic solar cells*. Springer: 2013; Vol. 2.

76. Servaites, J. D.; Ratner, M. A.; Marks, T. J., Organic solar cells: a new look at traditional models. *Energy & Environmental Science* **2011,** *4* (11), 4410-4422.

77. Lefky, C.; Mamidanna, A.; Huang, Y.; Hildreth, O., Impact of solvent selection and temperature on porosity and resistance of printed self-reducing silver inks. *physica status solidi (A)* **2016**, 1-8.

78. Mamidanna, A.; Song, Z.; Lv, C.; Lefky, C. S.; Jiang, H.; Hildreth, O. J., Printing Stretchable Spiral Interconnects Using Reactive Ink Chemistries. *ACS applied materials & interfaces* **2016,** *8*, 12594-12598.

79. Jeffries, A.; Mamidanna, A.; Clenney, J.; Ding, L.; Hildreth, O.; Bertoni, M. In *Innovative Methods for Low-Temperature Contact Formation For Photovoltaics Applications*, Photovoltaic Specialist Conference (PVSC), 2015 IEEE 42nd, IEEE: 2015; pp 1-5.

80. Walker, S. B.; Lewis, J. A., Reactive silver inks for patterning high-conductivity features at mild temperatures. *Journal of the American Chemical Society* **2012,** *134* (3), 1419-1421.

81. Rosen, Y.; Grouchko, M.; Magdassi, S., Printing a Self-Reducing Copper Precursor on 2D and 3D Objects to Yield Copper Patterns with 50% Copper's Bulk Conductivity. *Advanced Materials Interfaces* **2015,** *2* (3), 1400448(1-5).

82. Farraj, Y.; Grouchko, M.; Magdassi, S.; Koch, F.; Wittkötter, M.; Müller, M.; Reinhold, I.; Zapka, W. In *Ink-Jet Printed Copper Complex MOD Ink for Plastic Electronics*, NIP & Digital Fabrication Conference, Society for Imaging Science and Technology: 2014; pp 191-193.

83. Shin, D.-H.; Woo, S.; Yem, H.; Cha, M.; Cho, S.; Kang, M.; Jeong, S.; Kim, Y.; Kang, K.; Piao, Y., A self-reducible and alcohol-soluble copper-based metal–organic decomposition ink for printed electronics. *ACS applied materials & interfaces* **2014,** *6* (5), 3312-3319.

84. Lee, H. M.; Seo, J. Y.; Jung, A.; Choi, S.-Y.; Ko, S. H.; Jo, J.; Park, S. B.; Park, D., Long-term sustainable aluminum precursor solution for highly conductive thin films on rigid and flexible substrates. *ACS applied materials & interfaces* **2014,** *6* (17), 15480-15487.

85. Lee, H. M.; Lee, H. B.; Jung, D. S.; Yun, J.-Y.; Ko, S. H.; Park, S. B., Solution processed aluminum paper for flexible electronics. *Langmuir* **2012,** *28* (36), 13127-13135.

86. Li, D.; Sutton, D.; Burgess, A.; Graham, D.; Calvert, P. D., Conductive copper and nickel lines via reactive inkjet printing. *Journal of Materials Chemistry* **2009,** *19* (22), 3719-3724.

87. Ginley, D. S.; Curtis, C. J.; Miedaner, A.; Van Hest, M. F. A. M.; Kaydanova, T., Metal Inks. Google Patents: 2006.

88. Valeton, J. J.; Hermans, K.; Bastiaansen, C. W.; Broer, D. J.; Perelaer, J.; Schubert, U. S.; Crawford, G. P.; Smith, P. J., Room temperature preparation of conductive silver features using spin-coating and inkjet printing. *Journal of Materials Chemistry* **2010,** *20* (3), 543-546.

89. Lee, H. M.; Choi, S. Y.; Kim, K. T.; Yun, J. Y.; Jung, D. S.; Park, S. B.; Park, J., A Novel Solution-Stamping Process for Preparation of a Highly Conductive Aluminum Thin Film. *Adv. Mater.* **2011,** *23* (46), 5524-5528.

90. Jenkins, G.; Wang, Y.; Xie, Y. L.; Wu, Q.; Huang, W.; Wang, L.; Yang, X., Printed electronics integrated with paper-based microfluidics: new methodologies for next-generation health care. *Microfluidics and Nanofluidics* **2015,** *19* (2), 251-261.

91. Farraj, Y.; Grouchko, M.; Magdassi, S., Self-reduction of a copper complex MOD ink for inkjet printing conductive patterns on plastics. *Chemical Communications* **2015,** *51* (9), 1587-1590.

92. Ross, I. M., The invention of the transistor. *Proceedings of the IEEE* **1998,** *86* (1), 7-28.

93. Alford, T. L.; Thompson, D. C.; Mayer, J.; Theodore, N. D., Dopant activation in ion implanted silicon by microwave annealing. *Journal of Applied Physics* **2009,** *106* (11), 114902.

94. Jain, S.; Schoenmaker, W.; Lindsay, R.; Stolk, P.; Decoutere, S.; Willander, M.; Maes, H., Transient enhanced diffusion of boron in Si. *Journal of applied physics* **2002,** *91* (11), 8919-8941.

95. Michel, A.; Rausch, W.; Ronsheim, P.; Kastl, R., Rapid annealing and the anomalous diffusion of ion implanted boron into silicon. *Applied physics letters* **1987,** *50* (7), 416-418.

96. Claverie, A.; Giles, L.; Omri, M.; De Mauduit, B.; Assayag, G. B.; Mathiot, D., Nucleation, growth and dissolution of extended defects in implanted Si: impact on dopant diffusion. *Nuclear Instruments and Methods in Physics Research Section B: Beam Interactions with Materials and Atoms* **1999,** *147* (1), 1-12.

97. Damm, M.; Kappe, C. O., Parallel microwave chemistry in silicon carbide reactor platforms: an in-depth investigation into heating characteristics. *Molecular diversity* **2009,** *13* (4), 529-543.

98. Poweleit, C.; Gunther, A.; Goodnick, S.; Menéndez, J., Raman imaging of patterned silicon using a solid immersion lens. *Applied physics letters* **1998,** *73* (16), 2275-2277.

99. Suni, I.; Göltz, G.; Nicolet, M.-A.; Lau, S., Effects of electrically active impurities on the epitaxial regrowth rate of amorphized silicon and germanium. *Thin Solid Films* **1982,** *93* (1), 171-178.

100. Calvo, P.; Claverie, A.; Cherkashin, N.; Colombeau, B.; Lamrani, Y.; De Mauduit, B.; Cristiano, F., Thermal evolution of {113} defects in silicon: transformation against dissolution. *Nuclear Instruments and Methods in Physics Research Section B: Beam Interactions with Materials and Atoms* **2004,** *216*, 173-177.

101. Cutroni, M.; Mandanici, A.; Piccolo, A.; Fanggao, C.; Saunders, G.; Mustarelli, P., Ionic conduction in silver phosphate glasses doped with silver sulphide. *Philosophical Magazine B* **1996,** *73* (2), 349-365.

102. Funke, K., Ion dynamics and correlations: Translational and localized ionic hopping motion in solid electrolytes. *Philosophical Magazine A* **1993,** *68* (4), 711-724.

103. León, C.; Lucia, M.; Santamaria, J., Correlated ion hopping in single-crystal yttria-stabilized zirconia. *Physical Review B* **1997,** *55* (2), 882.

104. Cristiano, F.; Hebras, X.; Cherkashin, N.; Claverie, A.; Lerch, W.; Paul, S., Clusters formation in ultralow-energy high-dose boron-implanted silicon. *Applied physics letters* **2003,** *83* (26), 5407-5409.

105. Xu, P.; Fu, C.; Hu, C.; Zhang, D. W.; Wu, D.; Luo, J.; Zhao, C.; Zhang, Z.-B.; Zhang, S.-L., Ultra-shallow junctions formed using microwave annealing. *Applied Physics Letters* **2013,** *102* (12), 122114.

106. Cojocaru-Mirédin, O.; Cristiano, F.; Fazzini, P.-F.; Mangelinck, D.; Blavette, D., Extended defects and precipitation in heavily B-doped silicon. *Thin Solid Films* **2013,** *534*, 62-66.

107. Alford, T. L.; Thompson, D.; Mayer, J.; Theodore, N. D., Dopant activation in ion implanted silicon by microwave annealing. *Journal of Applied Physics* **2009,** *106* (11), 114902.

108. Murakoshi, A.; Harada, T.; Miyano, K.; Harakawa, H.; Aoyama, T.; Yamashita, H.; Kohyama, Y., Boron diffusion layer formation using Ge cryogenic implantation with low-temperature microwave annealing. *Japanese Journal of Applied Physics* **2016,** *55* (4), 046501.

109. Michalak, T. J.; Herman, J.; Basavalingappa, A.; Rodgers, M.; Françca, D.; Borst, C., Study of millisecond laser annealing on recrystallization, activation, and mobility of laser annealed SOI doped via arsenic ion implantation. *Journal of Vacuum Science & Technology B* **2015,** *33* (1), 011201.

110. Paul, S.; Lerch, W.; Chan, J.; McCoy, S.; Gelpey, J.; Cristiano, F.; Severac, F.; Fazzini, P.; Bolze, D., Optimum activation and diffusion with a combination of spike and flash annealing. *JOURNAL OF VACUUM SCIENCE AND TECHNOLOGY B MICROELECTRONICS AND NANOMETER STRUCTURES* **2008,** *26* (1), 293.

111. Green, M. A.; Keevers, M. J., Optical properties of intrinsic silicon at 300 K. *Progress in Photovoltaics: Research and Applications* **1995,** *3* (3), 189-192.

112. Zhao, Z.; Theodore, N. D.; Vemuri, R. N.; Das, S.; Lu, W.; Lau, S.; Alford, T. L., Effective dopant activation via low temperature microwave annealing of ion implanted silicon. *Applied Physics Letters* **2013,** *103* (19), 192103.

113. Feldman, L. C.; Mayer, J. W.; Picraux, S. T., *Materials analysis by ion channeling: submicron crystallography*. Academic Press: 1986.

114. Dhar, A.; Zhao, Z.; Alford, T. L., Effect of Gold Thickness and Annealing on Optical and Electrical Properties of TiO2/Au/TiO2 Multilayers as Transparent Composite Electrode on Flexible Substrate. *JOM* **2015,** *67* (4), 840-844.

115. Williams, W. E., *Applications of interferometry*. Methuen: London, 1950.

116. Han, Y. C.; Lim, M. S.; Park, J. H.; Choi, K. C., Optical Effect of Surface Morphology of Ag on Multilayer Electrode Applications for OLEDs. *Ieee Electron Device Letters* **2014,** *35* (2), 238-240.

117. Lu, Y. C.; Chen, C. Y.; Shen, K. C.; Yeh, D. M.; Tang, T. Y.; Yang, C. C., Enhanced photoluminescence excitation in surface plasmon coupling with an InGaN/GaN quantum well. *Applied Physics Letters* **2007,** *91* (18).

118. Malinsky, M. D.; Kelly, K. L.; Schatz, G. C.; Van Duyne, R. P., Nanosphere lithography: Effect of substrate on the localized surface plasmon resonance spectrum of silver nanoparticles. *Journal of Physical Chemistry B* **2001,** *105* (12), 2343-2350.

119. Duche, D.; Torchio, P.; Escoubas, L.; Monestier, F.; Simon, J. J.; Flory, F.; Mathian, G., Improving light absorption in organic solar cells by plasmonic contribution. *Solar Energy Materials and Solar Cells* **2009,** *93* (8), 1377-1382.

120. Mayer, K. M.; Hafner, J. H., Localized surface plasmon resonance sensors. *Chemical reviews* **2011,** *111* (6), 3828-3857.

121. Jain, P. K.; Huang, X.; El-Sayed, I. H.; El-Sayad, M. A., Review of some interesting surface plasmon resonance-enhanced properties of noble metal nanoparticles and their applications to biosystems. *Plasmonics* **2007,** *2* (3), 107-118.

122. Yu, J. G.; Xiong, J. F.; Cheng, B.; Liu, S. W., Fabrication and characterization of Ag-TiO2 multiphase nanocomposite thin films with enhanced photocatalytic activity. *Applied Catalysis B-Environmental* **2005,** *60* (3-4), 211-221.

123. He, J. H.; Ichinose, I.; Kunitake, T.; Nakao, A., In situ synthesis of noble metal nanoparticles in ultrathin TiO2-gel films by a combination of ion-exchange and reduction processes. *Langmuir* **2002,** *18* (25), 10005-10010.

124. Balci, S.; Kocabas, C.; Ates, S.; Karademir, E.; Salihoglu, O.; Aydinli, A., Tuning surface plasmon-exciton coupling via thickness dependent plasmon damping. *Physical Review B* **2012,** *86* (23), 235402.

125. Zayats, A. V.; Smolyaninov, II; Maradudin, A. A., Nano-optics of surface plasmon polaritons. *Physics Reports-Review Section of Physics Letters* **2005,** *408* (3-4), 131-314.

126. Sivaramakrishnan, K.; Alford, T. L., Conduction and transmission analysis in gold nanolayers embedded in zinc oxide for flexible electronics. *Applied Physics Letters* **2010,** *96* (20).

127. Dhar, A.; Alford, T. L., High quality transparent TiO2/Ag/TiO2 composite electrode films deposited on flexible substrate at room temperature by sputtering. *Apl Materials* **2013,** *1* (1).

128. Dhar, A.; Alford, T. L., Optimization of Nb2O5/Ag/Nb2O5 multilayers as transparent composite electrode on flexible substrate with high figure of merit. *Journal of Applied Physics* **2012,** *112* (10).

129. Dhar, A.; Zhao, Z.; Alford, T. L., Effect of Gold Thickness and Annealing on Optical and Electrical Properties of TiO2/Au/TiO2 Multilayers as Transparent Composite Electrode on Flexible Substrate. *JOM* **2015,** *67* (4), 840-844.

130. Dhar, A.; Alford, T. L, *Optimization of IGZO/Cu/IGZO Multilayers as Transparent Composite Electrode on Flexible Substrate by Room-temperature Sputtering and Post-Deposition Anneals*, MRS Proceedings, Cambridge Univ Press: 2013; pp mrss13-1577-xx03-33.

131. Dhar, A.; Zhao, Z.; Alford, T. L., Effect of Different Substrates on the Wettability and Electrical Properties of Au Thin Films Deposited by Sputtering. *JOM* **2015,** *67* (4), 845-848.

132. Dhar, A.; Alford, T. L., Optimization of TiO2/Cu/TiO2 Multilayer as Transparent Composite Electrode (TCE) Deposited on Flexible Substrate at Room Temperature. *ECS Solid State Letters* **2014,** *3* (11), N33-N36.

133. Han, H.; Theodore, N. D.; Alford, T. L., Improved conductivity and mechanism of carrier transport in zinc oxide with embedded silver layer. *Journal of Applied Physics* **2008,** *103* (1).

134. Kim, S.; Lee, J. L., Design of dielectric/metal/dielectric transparent electrodes for flexible electronics. *Journal of Photonics for Energy* **2012,** *2*.

135. Zhao, Z.; Khorasani, A. E.; Theodore, N.; Dhar, A.; Alford, T. L., Prediction of transmittance spectra for transparent composite electrodes with ultra-thin metal layers. *Journal of Applied Physics* **2015,** *118* (20), 205304.

136. Jang, Y.; Seo, J. W.; Seok, J.; Lee, J. Y.; Kim, K., Roughening Conjugated Polymer Surface for Enhancing the Charge Collection Efficiency of Sequentially Deposited Polymer/Fullerene Photovoltaics. *Polymers* **2015,** *7* (8), 1497-1509.

137. Kim, S.; Lee, J.-L., Design of dielectric/metal/dielectric transparent electrodes for flexible electronics. *Journal of Photonics for Energy* **2012,** *2* (1), 021215-021215.

138. Leftheriotis, G.; Yianoulis, P.; Patrikios, D., Deposition and optical properties of optimised ZnS/Ag/ZnS thin films for energy saving applications. *Thin solid films* **1997,** *306* (1), 92-99.

139. Zhao, Z.; Alford, T. L., The optimal TiO 2/Ag/TiO 2 electrode for organic solar cell application with high device-specific Haacke figure of merit. *Solar Energy Materials and Solar Cells* **2016,** *157*, 599-603.

140. Lai, T.-H.; Tsang, S.-W.; Manders, J. R.; Chen, S.; So, F., Properties of interlayer for organic photovoltaics. *Materials Today* **2013,** *16* (11), 424-432.

141. Lattante, S., Electron and hole transport layers: their use in inverted bulk heterojunction polymer solar cells. *Electronics* **2014,** *3* (1), 132-164.

142. Kim, D. Y.; Subbiah, J.; Sarasqueta, G.; So, F.; Ding, H.; Irfan, G., The effect of molybdenum oxide interlayer on organic photovoltaic cells. *Applied Physics Letters* **2009,** *95* (9), 3304.

143. Meyer, J.; Hamwi, S.; Kröger, M.; Kowalsky, W.; Riedl, T.; Kahn, A., Transition metal oxides for organic electronics: energetics, device physics and applications. *Adv. Mater.* **2012,** *24* (40), 5408-5427.

144. Dasgupta, B.; Goh, W. P.; Ooi, Z. E.; Wong, L. M.; Jiang, C. Y.; Ren, Y.; Tok, E. S.; Pan, J.; Zhang, J.; Chiam, S. Y., Enhanced extraction rates through gap states of molybdenum oxide anode buffer. *The Journal of Physical Chemistry C* **2013,** *117* (18), 9206-9211.

145. Wong, K. H.; Ananthanarayanan, K.; Luther, J.; Balaya, P., Origin of hole selectivity and the role of defects in low-temperature solution-processed molybdenum oxide interfacial layer for organic solar cells. *The Journal of Physical Chemistry C* **2012,** *116* (31), 16346-16351.

146. Tremolet de Villers, B.; Tassone, C. J.; Tolbert, S. H.; Schwartz, B. J., Improving the reproducibility of P3HT: PCBM solar cells by controlling the PCBM/cathode interface. *The Journal of Physical Chemistry C* **2009,** *113* (44), 18978-18982.

147. Zhou, Y.; Shim, J. W.; Fuentes-Hernandez, C.; Sharma, A.; Knauer, K. A.; Giordano, A. J.; Marder, S. R.; Kippelen, B., Direct correlation between work function of indium-tin-oxide electrodes and solar cell performance influenced by ultraviolet irradiation and air exposure. *Physical Chemistry Chemical Physics* **2012,** *14* (34), 12014-12021.

148. Shrotriya, V.; Li, G.; Yao, Y.; Chu, C.-W.; Yang, Y., Transition metal oxides as the buffer layer for polymer photovoltaic cells. *Applied Physics Letters* **2006,** *88* (7), 073508.

149. Kroger, M.; Hamwi, S.; Meyer, J.; Riedl, T.; Kowalsky, W.; Kahn, A., Role of the deep-lying electronic states of MoO3 in the enhancement of hole-injection in organic thin films. *Applied physics letters* **2009,** *95* (12), 123301.

150. Meyer, J.; Kidambi, P. R.; Bayer, B. C.; Weijtens, C.; Kuhn, A.; Centeno, A.; Pesquera, A.; Zurutuza, A.; Robertson, J.; Hofmann, S., Metal oxide induced charge transfer doping and band alignment of graphene electrodes for efficient organic light emitting diodes. *Scientific reports* **2014,** *4*.

151. Cho, S.; Piper, L.; DeMasi, A.; Preston, A.; Smith, K.; Chauhan, K.; Hatton, R. A.; Jones, T. S., Soft X-ray spectroscopy of C60/copper phthalocyanine/MoO3

interfaces: role of Reduced MoO3 on energetic band alignment and improved performance. *The Journal of Physical Chemistry C* **2010,** *114* (42), 18252-18257.

152. Das, S.; Alford, T. L., Improved efficiency of P3HT: PCBM solar cells by incorporation of silver oxide interfacial layer. *Journal of Applied Physics* **2014,** *116* (4), 044905.

153. Kamyshny, A.; Steinke, J.; Magdassi, S., Metal-based inkjet inks for printed electronics. *The Open Applied Physics Journal* **2011,** *4* (1), 19-36.

154. Wu, J.-T.; Hsu, S. L.-C.; Tsai, M.-H.; Hwang, W.-S., Inkjet printing of low-temperature cured silver patterns by using AgNO3/1-dimethylamino-2-propanol inks on polymer substrates. *The Journal of Physical Chemistry C* **2011,** *115* (22), 10940-10945.

155. Magdassi, S.; Grouchko, M.; Kamyshny, A., Copper nanoparticles for printed electronics: routes towards achieving oxidation stability. *Materials* **2010,** *3* (9), 4626-4638.

156. Lee, B.; Kim, Y.; Yang, S.; Jeong, I.; Moon, J., A low-cure-temperature copper nano ink for highly conductive printed electrodes. *Current Applied Physics* **2009,** *9* (2), e157-e160.

157. Magdassi, S.; Grouchko, M.; Berezin, O.; Kamyshny, A., Triggering the sintering of silver nanoparticles at room temperature. *ACS nano* **2010,** *4* (4), 1943-1948.

158. Grouchko, M.; Kamyshny, A.; Mihailescu, C. F.; Anghel, D. F.; Magdassi, S., Conductive inks with a "built-in" mechanism that enables sintering at room temperature. *ACS nano* **2011,** *5* (4), 3354-3359.

159. Huang, Q.; Shen, W.; Xu, Q.; Tan, R.; Song, W., Room-temperature sintering of conductive Ag films on paper. *Materials Letters* **2014,** *123*, 124-127.

160. Alford, T. L.; Misra, E.; Bhagat, S.; Mayer, J., Influence of Joule heating during electromigration evaluation of silver lines. *Thin Solid Films* **2009,** *517* (5), 1833-1836.

161. Black, J. R., Electromigration—A brief survey and some recent results. *Electron Devices, IEEE Transactions on* **1969,** *16* (4), 338-347.

162. Misra, E.; Theodore, N.; Mayer, J.; Alford, T. L., Failure mechanisms of pure silver, pure aluminum and silver–aluminum alloy under high current stress. *Microelectronics Reliability* **2006,** *46* (12), 2096-2103.

163. Indluru, A.; Misra, E.; Alford, T. L., Current-Density Dependence on Ag eFUSEs With TiN Underlayers. *Electron Device Letters, IEEE* **2009,** *30* (11), 1134-1136.

164. Yeh, E. C.; Choi, W.; Tu, K.; Elenius, P.; Balkan, H., Current-crowding-induced electromigration failure in flip chip solder joints. *Applied physics letters* **2002,** *80* (4), 580-582.

165. Gousseau, S.; Moreau, S.; Bouchu, D.; Farcy, A.; Montmitonnet, P.; Inal, K.; Bay, F.; Zelsmann, M.; Picard, E.; Salaun, M., Electromigration-induced failure in operando characterization of 3D interconnects: microstructure influence. *Microelectronics Reliability* **2015,** *55* (8), 1205-1213.

166. Ceric, H.; Rovitto, M. In *Impact of microstructure and current crowding on electromigration: A TCAD study*, Simulation of Semiconductor Processes and Devices (SISPAD), 2015 International Conference on, IEEE: 2015; pp 194-197.

167. Tian, X.; Moser, M. L.; Pekker, A.; Sarkar, S.; Ramirez, J.; Bekyarova, E.; Itkis, M. E.; Haddon, R. C., Effect of atomic interconnects on percolation in single-walled carbon nanotube thin film networks. *Nano letters* **2014,** *14* (7), 3930-3937.

168. Pennetta, C.; Reggiani, L.; Trefán, G., Scaling and universality in electrical failure of thin films. *Physical review letters* **2000,** *84* (21), 5006.

169. Misra, E.; Islam, M. M.; Hasan, M.; Kim, H.; Alford, T. L., Percolative approach for failure time prediction of thin film interconnects under high current stress. *Microelectronics Reliability* **2005,** *45* (2), 391-395.

170. Chang, S.-Y.; Chen, C.-F.; Lin, S.-J.; Kattamis, T. Z., Electrical resistivity of metal matrix composites. *Acta materialia* **2003,** *51* (20), 6291-6302.

171. Scorzoni, A.; De Munari, I.; Stulens, H.; D.; D, T. Z., Ele-linear resistance behavior in the early stages and after electromigration in Al-Si lines. *Journal of applied physics* **1996,** *80* (1), 143-150.

172. Zhang, F.; Xu, X.; Tang, W.; Zhang, J.; Zhuo, Z.; Wang, J.; Wang, J.; Xu, Z.; Wang, Y., Recent development of the inverted configuration organic solar cells. *Solar Energy Materials and Solar Cells* **2011,** *95* (7), 1785-1799.